

AD A104241

12

LEVEL II

DTIC FILE COPY

DTIC
ELECTE
SEP 16 1981
S D
B

DISTRIBUTION STATEMENT A

Approved for public release;
Distribution Unlimited



DEPARTMENT OF PHYSICS

81 9 16 014

(12)

LEVEL II

DEPARTMENT OF PHYSICS
WASHINGTON STATE UNIVERSITY
PULLMAN, WA 99164

TECHNICAL REPORT NO. 1
LIGHT SCATTERING BY BUBBLES
IN LIQUIDS OR IN GLASS

by

Philip L. Marston, Dean S. Langley,
and Dwight L. Kingsbury

September 1, 1981

Prepared for:
OFFICE OF NAVAL RESEARCH
CONTRACT NO. N00014-80-C-0838

DTIC
ELECTE
SEP 16 1981
S D
B

Approved for public release; distribution unlimited
Reproduction in whole or in part is permitted for
any purpose of the United States Government

REPORT DOCUMENTATION PAGE		READ INSTRUCTIONS BEFORE COMPLETING FORM
1. REPORT NUMBER 1	2. GOVT ACCESSION NO. AD-A204 242	3. RECIPIENT'S CATALOG NUMBER
4. TITLE (and Subtitle) LIGHT SCATTERING BY BUBBLES IN LIQUIDS OR IN GLASS.		5. TYPE OF REPORT & PERIOD COVERED Interim Technical Report 1 July 80 - 31 Aug 81
7. AUTHOR(s) Philip L. Marston, Dean S. Langley Dwight L. Kingsbury		8. CONTRACT OR GRANT NUMBER(s) N00014-80-C-0838
9. PERFORMING ORGANIZATION NAME AND ADDRESS Department of Physics Washington State University Pullman, WA 99164		10. PROGRAM ELEMENT PROJECT, TASK AREA & WORK UNIT NUMBERS
11. CONTROLLING OFFICE NAME AND ADDRESS Office of Naval Research Physics Program Office Arlington, VA 22217		12. REPORT DATE 1 September 1981
14. MONITORING AGENCY NAME & ADDRESS (if different from Controlling Office)		13. NUMBER OF PAGES 90
		15. SECURITY CLASS. (of this report) Unclassified
		15a. DECLASSIFICATION/DOWNGRADING SCHEDULE
16. DISTRIBUTION STATEMENT (of this Report) Approved for public release; distribution unlimited.		
17. DISTRIBUTION STATEMENT (of the abstract entered in Block 20, if different from Report)		
18. SUPPLEMENTARY NOTES		
19. KEY WORDS (Continue on reverse side if necessary and identify by block number) light scattering, bubbles, Mie theory, glass, fused silica, optical oceanography, optical properties of water, laser-Doppler velocimetry, cavitation, backscattering, diffraction, depolarization, optical or acoustical inhomogeneities, two-phase flow, Brewster angle, light extinction		
20. ABSTRACT (Continue on reverse side if necessary and identify by block number) This technical report consists of publications and supplemental information related to the scattering of light by bubbles in liquids and in glass. The emphasis of the report is to understand the scattering by air bubbles in water into the angular regions where diffraction makes essential corrections to elementary ray optics. For bubbles these regions are backward, forward, and		

20. (con.)

critical angle scattering. Structure in the scattering in these regions is present in the scattering computed from Mie theory for bubbles in water and in fused silica glass. Most of the previous literature on light scattering is concerned with drop-like objects where the refractive index of the scatterer exceeds that of the surroundings.

Angular structures in the far-field scattering from a bubble in water near the critical scattering angle at 83° are observed and modeled. Mie theory supports a model of diffraction and interference near the critical scattering angle provided the product of the wave number k and the radius a lies in the range $25 \leq ka \leq 1000$. When the scattering angle $\phi < 83^\circ$, there is a coarse structure to the scattering with a quasi-period $\leq (\lambda/a)^{1/2}$ radians where λ is the wavelength. There is also a fine structure to the scattering with an angular spacing proportional to (λ/a) . Photographs of the scattering show some of these predicted features. A reduction in the scattering of parallel polarized light near the Brewster scattering angle, which is near 106° for an air bubble in water, is predicted. Application of these structures to bubble sizing and detection are summarized and the theoretical extinction coefficient in water is plotted.

Mie computations for bubbles in water also reveal backward and forward glory effects. These are partially manifested as cross polarized scattering. Observed from bubbles in a viscous silicone oil to the near backward direction is found to have a strong cross-polarized component.

Accession For	
NTIS	<input checked="" type="checkbox"/>
DTIC	<input type="checkbox"/>
DDIC	<input type="checkbox"/>
Accession For	
P	
Distribution/	
Availability Codes	
Distribution/or	
Distribution	
A	

Unclassified

TABLE OF CONTENTS

	Page
REPORT DOCUMENTATION PAGE	1
PREFACE	4
PAPER NO.	
1. Light scattering by bubbles in liquids: Mie theory, physical-optics approximations, and experiments (P. L. Marston, D. S. Langley, and D. L. Kingsbury).	8
2. Critical angle scattering by a bubble: Physical-optics approximation and observations (P. L. Marston).	29
3. Scattering by a bubble in water near the critical angle: interference effects (P. L. Marston and D. L. Kingsbury).	36
4. Mie scattering near the critical angle of bubbles in water (D. L. Kingsbury and P. L. Marston). [Includes supplement with unpublished graphs of computed Mie scattering by bubbles in water].	42
5. Scattering by bubbles in glass: Mie theory and physical optics approximation (D. L. Kingsbury and P. L. Marston).	54
6. Description of computer codes for Mie and model computations (D. L. Kingsbury and P. L. Marston).	58
7. Glory in the optical backscattering from air bubbles (D. S. Langley and P. L. Marston).	76

PREFACE

This technical report consists of publications, manuscripts, and supplemental information related to the scattering of light by bubbles in liquids and in glass. The emphasis of the report is on the scattering by air bubbles in water into the angular regions where diffraction makes essential corrections to elementary ray optics. For bubbles these regions are backward scattering, forward scattering, and critical angle scattering. Most of the previous literature on light scattering is concerned with drop-like objects where the refractive index of the scatterer exceeds that of the surroundings. The present results should be useful for the optical characterization of microbubbles at sea¹ and in water tunnels², or for the prediction of the optical properties of bubbly media. They should also be useful for laser-Doppler anemometry with microbubbles and the detection of microbubbles in glass.

Certain phenomena described here should be present for other spherical or nearly spherical scatterers where the refractive index is less than that of the surroundings, for example: air bubbles in ice, water inclusions in fused quartz (such as those present in varieties of opal glass), ice spheres in water, and superheated drops in a host liquid. The coarse structure in the critical scattering region can be present even if the scatterer is not spherical.

The first paper summarizes experiments, models, and results of Mie computations for both backward and critical-angle scattering. Theoretical results presented indicate that axial focussing enhances the scattering by an air bubble in water into the near forward and near backward regions. This enhancement for the forward region, (forward optical glory), is more signifi-

cant for depolarized than for polarized scattering since the latter is dominated by ordinary forward diffraction. At present the experimental observations of axial focussing from single bubbles are limited to the backward glory of air bubbles in a viscous polymer liquid. (These are described in detail in the seventh paper). The first paper also discusses the scattering efficiency of bubbles and the relevance of far-field computations to near-field observations of bubbles.

The second paper describes the first observations of, and model for, the scattering in the critical region which is near 83 degrees for an air bubble in water. This paper is included here for completeness though it was not supported by the present ONR contract. It was supported in part by ONR Contract N00014-76-C-0527 (R. E. Apfel principal investigator).

The third paper describes an improved model (which includes both diffraction and interference) for the coarse structure near the critical scattering region.

The fourth paper is the first to be published which correctly gives the results of Mie theory for angular structure in the scattering by bubbles. This paper substantiates the model of the coarse structure developed in the third paper. The paper was excerpted from the Master's Degree Thesis of D. L. Kingsbury. A supplement attached here gives examples which were not published for reasons of brevity.

The fifth paper gives Mie theory and model results for air bubbles in fused silica glass. The paper is the first to discuss the Brewster scattering angle for bubbles and the first to give valid Mie results for bubbles over the entire (0 to 180 degrees) range of scattering angles.

The sixth paper describes computer codes used for some of the Mie and model computations. The codes shown here have been adapted for use on an HP 1000

minicomputer system. This paper is excerpted from the Master's Degree Thesis of D. L. Kingsbury. For a more complete description of the Mie scattering algorithm, consult the paper by Wiscombe³ which is the basis of these codes.

The seventh paper describes the first observations of backscattering from air bubbles in liquids. It also describes a physical-optics approximation for the backward axial focussing of scattered light. This model shows that the intensity of individual axially focussed rays are proportional to a^3 , while the simply reflected scattering is proportional to a^2 where a is the bubble radius. (The total backscattering is not simply proportional to a^3 due to the interference of various paths; see paper 1). Polarization and quasi-periodic properties of the glory are discussed.

The approximations and physical models described here for bubbles should also be useful for certain cases in the scattering of sound from fluid or elastic spheres. This has been verified by Marston and Kingsbury⁴ for scattering in the critical region from fluid spheres. Backward axial focussing or "acoustic glory" has also been proposed for elastic spheres in water.⁵

Care should be taken when applying the results of this report to light scattering by microbubbles in seawater. Our computations assume that the bubbles are spherical and that the refractive index of the scatterer is homogeneous. There is a natural tendency for the gas in microbubbles to dissolve into the surrounding liquid.⁶ There is some recent evidence that microbubbles in seawater can be stabilized by substances sorbed onto their surface.⁷ The presences of a sorbed film or small deviations from sphericity may alter the details of the

scattering patterns described here, but it should not obliterate the existence of axial focusing and the coarse and fine structures.

Philip L. Marston
Principal Investigator

REFERENCES TO PREFACE

1. B. D. Johnson, and R. C. Cooke, "Bubble populations and spectra in coastal waters: a photographic approach," J. Geophys. Res. 84, 3761-3766 (1979).
2. H. W. H. E. Godefroy, R. H. J. Jansen, A. P. Keller, Y. Lecoivre, P. M. Oldenziel and R. L. van Renesse, Comparison of measuring and control methods of the water quality with respect to cavitation behaviour (Waterloopkundig Laboratorium, Delft Hydraulics Laboratory, 1981).
3. W. J. Wiscombe, "Improved Mie scattering algorithms," Applied Optics 19, 1505-1509 (1980).
4. P. L. Marston and D. L. Kingsbury, "Acoustic scattering from fluid spheres: Diffraction and interference near the critical scattering angle," J. Acoust. Soc. Am. (accepted for publication).
5. P. L. Marston and L. Flax, "Glory contribution to the backscatter from large elastic spheres," J. Acoust. Soc. Am. Suppl. 68, S81 (1980).
6. P. S. Epstein and M. S. Plesset, "On the stability of gas bubbles in liquid-gas solutions," J. Chem. Phys. 18, 1505-1509 (1950).
7. B. D. Johnson and R. C. Cooke, "Generation of stabilized microbubbles in seawater," Science 213, 209-211 (1981).

Paper No. 1

Light scattering by bubbles in liquids: Mie theory, physical-optics approximations, and experiments (P. L. Marston, D. S. Langley, and D. L. Kingsbury) to be published in the journal Applied Scientific Research in the proceedings of the IUTAM Symposium on the Mechanics and Physics of Bubbles in Liquids. This paper was presented at the Symposium (June, 1981).

Abstract

Angular structures in the far-field scattering from bubbles are observed and modeled. Mie theory supports a model of diffraction and interference near the critical scattering angle. A new expression for the angular spacing of fine structure is derived. Photographs of scattering show some of the predicted features. Application of these structures to bubble sizing and detection are summarized and the theoretical extinction coefficient in water is plotted.

Mie computations for bubbles in water also reveal backward and forward glory effects. These are partially manifested as cross-polarized scattering. Observed scattering from bubbles in the near backward direction is found to have a strong cross-polarized component.

1. Introduction

Equations for the scattering of plane electromagnetic waves by a dielectric sphere were given by Mie [1] in 1908 and the resulting features of the angular scattering pattern of drops are well known [2-4]. The Mie solution, though exact, does not give insight into either the scattering process, or changes in the pattern resulting from changes in shape, refractive index, or profile of the incident wave fronts. Reviews of the literature on light scattering [2-4] reveal a paucity of information about the scattering pattern of bubbles in liquids where the refractive index of the scatterer n_i is less than that of the surroundings n_o . Consequently we have begun [5-10] a systematic study of the scattering of light by gas bubbles in liquids. Aspects of the study are: (1) the computation of Mie scattering; (2) the development of simple physical models which give insight; and (3) observations of features in the scattering which differ significantly from both the scattering by drops and the scattering predicted by geometrical optics [11]. In this paper we summarize the main features of the scattering with an emphasis on the critical [5-7] and backscatter [10] regions. New experiments and applications will be described. These are the first detailed observations of scattering by bubbles.

Mie's solution [1-3] to the problem of the scattering efficiency and pattern of a dielectric sphere is a function of the ratio $m = n_i/n_o$. It is usually expressed as a function of $x = ka = 2\pi a/\lambda_o$ where a is the sphere radius, k and λ_o are the wavenumber and wavelength in the outer dielectric. Optical sources are typically characterized by the wavelength in a vacuum λ_v ; we note that $k = 2\pi n_o/\lambda_v$. For an air filled bubble, $n_i = 1.00029$

and it is usually a good approximation to take $m = 1/n_0$. Most of this paper will deal with scattering by spherical bubbles with plane incident waves. We will gain some insight however, into which features of the scattering pattern should be sensitive to deviations from sphericity.

2. Scattering Efficiency

The efficiency factor Q_{sca} is the ratio of the total scattering cross section to the geometric cross section πa^2 . When n_i is real valued, Q_{sca} also gives the extinction efficiency [2-4,12]. Figure 1 compares Q_{sca} for drops of water in air with $m = 4/3$ with that for a bubble in water with $m = 3/4$. The computations were performed using a slightly modified version [9] of Wiscombe's MIEVO Mie scattering algorithm [13]. A table of Q_{sca} for bubbles exists [14] which is consistent with Fig. 1. For a fixed λ_v , and a given value of x , the drop's radius is larger than the bubble's radius by a factor of 4/3. For the case of light from a He-Ne laser, $\lambda_v = 0.6328 \mu m$; for bubbles in water, x of 10, 100, 1000, and 10 000 give a of 0.75, 7.55, 75.5, and 755 μm , respectively.

The salient feature of Fig. 1 is that for drops Q_{sca} exhibits a fine "ripple" structure [3,12] but that our calculations of Q_{sca} for bubbles do not reveal a ripple structure. For both drops and bubbles, Q_{sca} has a broad undulation with a quasi-period $\Delta x \approx \pi/|m - 1|$. This approximation, which has been derived from the theory of "anomalous diffraction" [2,3], appears to be useful for both bubbles and drops. The ripple structure present for drops is due to optical resonances [12] which are attributed, in part, to internal surface waves. The absence of such structure for bubbles is probably because $m < 1$ does not favor the entrapment of internal surface waves.

3. Critical and Brewster Angle Scattering

For scattering by drops, diffraction is important for the description of the forward, backward, and rainbow regions [2,3]. For bubbles, there is no longer a rainbow; however, a new region appears known as the critical scattering region [5]. Diffraction is important in this region because of an abrupt change in the amplitude of the reflected wave as the local angle of incidence θ changes from $\theta < \theta_c$ for small impact parameters to $\theta > \theta_c$ for large ones. Here $\theta_c = \arcsin(m^{-1})$ which is the critical angle for a plane surface. Figure 2 illustrates several ray paths which lead to a scattering angle ϕ (the deviation from the forward direction) of 50° . The number on the left specifies the number of internal chords p ; θ_p and ρ_p denote the angle of incidence and refraction of the p th ray. The reflected ray (which has $p = 0$) has a scattering angle $\phi = \pi - 2\theta_0$. For an air bubble in water with $m = 3/4$, the critical scattering angle is $\phi_c = \pi - 2\theta_c = 82.82^\circ$. Geometric optics [5, 6, 11] predicts that $|dI_j/d\phi| \rightarrow \infty$ as ϕ approaches ϕ_c from above ϕ_c . Here I_j is the normalized scattered intensity defined as follows: the actual j -polarized intensity at a distance $R \gg a$ from the bubble's center is the incident j -polarized intensity multiplied by $I_j (a/R)^2/4$. For the electric vector perpendicular to the scattering plane, $j = 1$; for the parallel case, $j = 2$. This normalization is appropriate for bubbles since geometric optics predicts that if the intensity of the $p = 0$ reflection could be considered by itself $I_j(\phi \leq \phi_c) = 1$ due to total reflection.

Our observations [5], model [5, 6], and Mie computations [7-9] demonstrate that instead of a divergence of $|dI_j/d\phi|$, the rise in I_j is spread out over the region $|\phi - \phi_c| \approx \Omega$ where $\Omega = \arcsin [0.8 (1-m^2)^{-1/2} (\lambda_0/a)^{1/2}] \approx 144x^{-1/2} \text{deg}$ for water. The model makes use of a physical optics approximation which is to (a) use ray optics

along with the reflection coefficients of a plane surface to compute the complex amplitudes of virtual waves which simulate the scattering, and (b) use Fraunhofer's approximation to compute the diffraction of the virtual wave to the far field where $R \gg xa$. Step (b) yields the improvements over the geometrical predictions [11]. This procedure is analogous to Airy's model of diffraction near the rainbow [2]. Additional approximations used in the model are: only the two most intense virtual waves for $\phi \approx \phi_c$ are included ($p = 0$ and 1); and the divergence of the derivative of the reflectivity is simulated by truncating the $p = 0$ reflection when $\theta_0 < \theta_c$.

To compare the model results with Mie theory,* we consider examples of bubbles in water which complement those previously published [7]. Figure 3 shows both theories for $x = 100$ and $j = 1$. It shows that there is a coarse structure in the Mie scattering for $\phi < \phi_c$ which has a quasi-period $\approx \Omega \approx 14.4^\circ$. This structure is described by the model except in the near forward direction ($\phi \lesssim 20^\circ$).

The Mie result also has a superposed fine structure where the magnitude of the quasi-period $< \lambda_0/a \text{ rad.} = 360^\circ x^{-1}$. Near ϕ_c , this fine structure arises primarily from the interference of the $p = 0$ wave with the wave due to the $p = 2$ ray in Fig. 2. Its quasi-period Ω_f may be estimated from the lateral separation $b_0 + b_2$ of virtual point sources which would simulate the scattering at a given ϕ . As shown in Fig. 2, this separation is the sum of the impact parameters b_p for these rays. Standard relations for the far-field interference applied to these sources gives:

$$\Omega_f(\phi) \approx \arcsin[\lambda_0/(b_0 + b_2)] \quad (1)$$

*The conversion from the Mie amplitudes S_j [2,3,13] to the I_j is $I_j = (2|S_j|/x)^2$.

where $b_p/\alpha = \sin\theta_p$, $\theta_0 = (\pi - \phi)/2$, $\phi = \pi + 2(\theta_2 - 2\theta_1)$ and from Snell's law, $m\sin\theta_p = \sin\theta_0$. Eq. (1) is only an approximation because it fails to include other (such as $p = 1$) virtual waves and it does not completely account for the longitudinal spacing of virtual sources and for how those sources vary with ϕ . With $\phi = \phi_c$ and $m = 3/4$, $b_0 + b_2 \approx \alpha/0.825$ and $\Omega_f \approx \arcsin(5.18 \times 10^{-1})$. This gives 2.97° at $x = 100$ which is in reasonable agreement with Fig. 3.

Figure 4 shows the Mie and physical-optics results for $x = 10\,000$ and $j = 1$. The fine structure quasi-period is greatly reduced; Eq. (1) gives $\Omega_f(\phi_c) \sim 0.0297^\circ$ which agrees with the Mie result of 0.03° . The amplitudes of the coarse undulations ($\Omega \approx 1.4^\circ$) decrease slightly with decreasing ϕ until $\phi \approx 75^\circ$. A graph of I_1 for $\phi < 75^\circ$ shows coarse undulations increasing in amplitude with decreasing ϕ . The explanation is that for $x = 10\,000$, with $\phi \gtrsim 75^\circ$ the coarse structure is primarily due to diffraction of the $p = 0$ wave [5] but for $\phi \lesssim 75^\circ$ it is primarily from the interference of the $p = 0$ wave with $p > 0$ waves [6]. Plots [7] of I_2 for this x also show this transition and that fine structure is significantly weaker when $j = 2$. Figure 3 does not show the transition because the diffraction region ($\phi_c - \phi \lesssim \Omega$) overlaps the region where interference with the $p = 1$ wave is significant.

As θ_0 approaches the Brewster angle, $\theta_B = \arctan(m)$, the reflectivity of the $p = 0$, $j = 2$ polarized ray vanishes [2]. Consequently, according to geometric optics, there is no contribution to I_2 from this ray at the Brewster scattering angle $\phi_B = \pi - 2\theta_B = 2 \arctan(m^{-1})$. Because the reflectivity varies slowly near ϕ_B , diffraction is less important than near ϕ_c . A coarse minimum is evident in the Mie I_2 near ϕ_B for bubbles in glass [8] and for bubbles in water where $\phi_B \approx 106.3^\circ$. When x drops below 5, its location shifts toward 90° ; the scattering pattern approaches that of a dipole radiator predicted by Rayleigh scattering theory [2, 3, 8].

4. Observations of Critical Angle Scattering

Previous observations [5] were limited to the ϕ region where the coarse undulations decreased with decreasing ϕ . We have a new apparatus similar to that in [5] except that it permits observations with ϕ down to 70° . As in [5], bubbles were attached to a vertical needle in distilled water. They were illuminated with a plane wave from a He-Ne laser with $\lambda_v = 632.8$ nm. They were photographed via a window with a camera focused on infinity to place the film in the far field. Because of a technical problem, we have not obtained precise direct measurements of α in the (horizontal) scattering plane along with the photographs, however, we have demonstrated that $\Omega_f(\phi_c)$ from Eq. (1) gives an α which is consistent with the observed and modeled coarse structure. Thus the α values quoted in Fig. 5 were determined from the coarse and fine structures and not from direct observations. Figure 5 serves more to illustrate phenomena described in Sec. 3 than to rigorously test the models with real bubbles. The angle scale is for a ϕ change in water. The horizontal displacement is not exactly linear in ϕ due to refractive corrections at the water-window-air interfaces. In Fig. 5(a), the broad bright region on the left is the first coarse maximum with $\phi < \phi_c$. On the right, the coarse undulations increase in amplitude as ϕ decreases, which is the modeled behavior. Figure 5(b) is for a smaller bubble (verified with direct observations). The coarse undulations are spread out and the fine structure is clearly visible with $\Omega_f = 0.07^\circ$.

5. Backward and Forward Glory

Backscattering from drops is known to be enhanced by the axial focusing of certain rays [2, 3]. A complete description of this "glory" for water drops

is complicated due to the necessity of including surface waves [15]. We have observed and modeled backscattering from air bubbles [10] and find that some aspects can be explained with a physical-optics approximation that does not include surface waves. For the following discussion, it is convenient to define $\gamma = \pi - \phi$; $\gamma = 0$ corresponds to exact backscattering.

Computed Mie intensities show that backscattering from bubbles may be significantly larger than that expected from reflection of the $p = 0$ ray. For $\gamma = 0$, the plane of scattering is no longer defined and $I_1 = I_2 = I$. Figure 6 shows several broad peaks in I which are significantly larger than the normalized intensity of the $p = 0$ reflection which, by itself, is $(m-1)^2/(m+1)^2 \approx 0.02$. Other axial (e.g. $p = 2$) rays are too weak to explain the magnitude of I .

For polarized incident light, scattering near $\gamma = 0$ may be described in part with (non-cross) polarized $I^{(1)}$ and cross-polarized $I^{(2)}$ normalized intensities. For $I^{(2)}$, the plane of polarization is rotated by 90° from incident polarization; symmetry gives $I^{(2)}(\gamma = 0) = 0$ while $I^{(1)}(\gamma = 0) = I_j(\gamma = 0)$. For $\gamma \neq 0$, the $I^{(\ell)}$ depend on both γ and the angle ξ which the scattering plane makes with the incident electric vector.* Figure 7(a) illustrates the computed scattering. Geometric models of $I^{(1)}(\gamma = 0)$ predict that the contributions of off-axis ($p = 3$ and 4) rays diverge as $\gamma \rightarrow 0$ because of a factor which accounts for focusing. This divergence is present in previous ray models [11], but was not discussed; it is also present for drops [2] for certain m . Because of this divergence, diffraction provides an essential correction to ray optics.

*The conversions from the complex Mie amplitudes S_j to the $I^{(\ell)}(\gamma \ll 10^\circ, \xi)$ are $I^{(1)} = |S^- - S^+ \cos 2\xi|^2/x^2$ and $I^{(2)} = |S^+ \sin 2\xi|^2/x^2$ where $S^\pm = S_1 \pm S_2$. Evidently the ξ dependence of Eq. (2) is of the correct type.

The scattering due to the $p = 3$ ray in Fig. 7(a) (insert) is a back-facing toroidal wave front which appears to originate at a virtual ring-like source known as the focal circle in the analogous [2] $p = 2$ scattering from drops. This source at point F is ringlike because the figure may be rotated around the optic axis through the center C. For large x , the stationary-phase approximation of far-field diffraction integrals gives the following proportionalities for off-axis ($p > 2$) contributions to the $I^{(\ell)}$ taken separately:

$$I_{(p)}^{(1)} \propto x[(c_1 + c_2) J_0(u) + (c_1 - c_2) J_2(u) \cos 2\epsilon]^2 \quad (2a)$$

$$I_{(p)}^{(2)} \propto x[(c_1 - c_2) J_2(u) \sin 2\epsilon]^2 \quad (2b)$$

where the c_j are combined Fresnel reflectivities and transmissivities of the j -polarized fields, $u = kb_p' \sin \gamma$, and b_p' is the impact parameter of the exactly backscattered p th ray. Because $I_{(p)}^{(\ell)} \propto x$, the unnormalized intensity is proportional to k_d^3 while that for the $p = 0$ ray is proportional to k_d^2 . Consequently, off-axis waves are dominant when x is sufficiently large. It is evident from Fig. 6 and 7(a) that the modeling of $I^{(\ell)}$ may require summation of electric fields from several virtual sources. (In physical optics, intensities do not add but fields do.) Interference of various ring-like and axial virtual sources depends on x and could lead to the broad structures in Fig. 6. Detailed computation of $I_{(p)}^{(1)}$ ($\gamma = 0$) give magnitudes sufficient to explain the Mie scattering. Due to the Bessel functions in Eq. (2), the actual scattering should be peaked at or near $\gamma = 0$.

We have observed backscattering from single air bubbles in a dimethylsiloxane-polymer liquid which were nearly immobilized by viscosity. In these

experiments, $m^{-1} = 1.403$, $\lambda_v = 632.8$ nm, $a = 0.3 - 0.8$ mm and $x \approx 4000 - 11\ 000$. The far-field cross-polarized intensity had a dependence on γ and ξ similar to that predicted by Eq. (2b) with $p = 3$. Equation (2b) predicts that when both $\sin \gamma \approx \gamma$ and $u \gg 1$, the minima in $I_{(3)}^{(2)}$ should be spaced by $\Delta \gamma \approx \pi (kb_3')^{-1}$ radians where $b_3' = 0.447a$. The prediction correctly described the observed $\ell = 2$ scattering which is apparently dominated here by the $p = 3$ virtual source. The focal circle was viewed by focusing the camera on the bubble. The $\ell = 1$ scattering was not dominated by a single class of rays. Cross-polarized scattering from a polydispersion of bubbles in water has also been seen.

Figure 7(b) shows an enhancement of near-forward cross-polarized scattering due to axial focusing. Focal circles due to the $p = 2$ and 3 rays largely contribute to the $\ell = 2$ scattering. The forward $\ell = 1$ scattering is dominated by ordinary diffraction [2] when x is large. Mie theory gives $i^{(1)} \sim 10^7$ when $\phi = 0$ for the x and m of Fig. 7. Forward optical glory has also been displayed in Mie scattering by water drops [16]. Its description is complicated by surface waves.

5. Discussion

Figures 3 - 7 demonstrate that for several angular regions, the intensity exceeds that of geometric scattering from a perfectly reflecting sphere of the same a (for which $I_j = 1$). This information should be useful in optical devices which size or detect bubbles [7, 17, 18]. Due to diffraction near ϕ_c , it is preferable to detect scattering with $\phi \approx \phi_c - \Omega$ than to observe it with $\phi \approx 90^\circ$ which is the usual practice [17] for bubbles in water. For an unpolarized source, the normalized total scattering is $(I_1 + I_2)/2$.

Though this paper has emphasized the far-field ϕ dependence, the results are also applicable to the imaging of bubbles. For example, if it is desired to resolve the virtual sources of the $p = 0$ and 1 rays in Fig. 2, the aperture of the imaging system should have an angular width $\gtrsim \Omega$. It is easier to resolve the $p = 0$ and $2'$ virtual sources since the angular width requirements are reduced to Ω_f . Resolution of identifiable virtual sources reveals the size of a bubble.

Fine structure in the far-field scattering, such as that shown in Fig. 5(b), arises from the interference of widely spaced rays. Consequently the positions of the maxima will be quite sensitive to changes in the bubble's shape. That part of the coarse structure due to the interference of $p = 0$ and 1 rays will also depend on the shape but more weakly. As is the case for drops [19], these shape dependences may be useful for detecting mechanical resonances.

Scattered intensities for bubbles in water purported to be from Mie theory have been used in a study of cavitation nuclei [17]. Comparison of our Mie results and model of the coarse structure (which are consistent for the α in question) with those in [17], show that the latter err significantly. Plots in [17] predict coarse maxima at $\phi = 100^\circ$ for $\alpha = 5 \mu\text{m}$ and $\phi = 120^\circ$ for $\alpha = 7.5 \mu\text{m}$ which are not present in our Mie computations. We cannot find any physical justification for coarse maxima at these ϕ for x near 100.

We are grateful to W. J. Wiscombe for providing the initial computer program from which the program used here was derived. This research was supported in part by the Washington State University Research and Arts Committee and by the Office of Naval Research. P. L. Marston is an Alfred P. Sloan Research Fellow.

References

1. Mie G (1908) Beiträge zur optik trüber medien, speziell kolloidaler metallösungen. Ann Phys (Leipzig) 25: 377-445.
2. Van de Hulst HC (1957) Light scattering by small particles. New York: Wiley.
3. Kerker M (1969) The scattering of light. New York: Academic.
4. Shipley ST and Weinman JA (1978) A numerical study of scattering by large dielectric spheres. J Opt Soc Am 68: 130-134.
5. Marston PL (1979) Critical angle scattering by a bubble: physical-optics approximation and observations. J Opt Soc Am 69: 1205-1211; (1980) Erratum. 70: 353.
6. Marston PL and Kingsbury DL (1981) Scattering by an air bubble in water near the critical angle: interference effects. J Opt Soc Am 71: 192-196; (1981) Erratum. 71: 917.
7. Kingsbury DL and Marston PL (1981) Mie scattering near the critical angle of bubbles in water. J Opt Soc Am 71: 358-361.
8. Kingsbury DL and Marston PL (1981) Scattering by bubbles in glass: Mie theory and physical optics approximation. Appl Opt 20: 2348-2350.
9. Kingsbury DL (1981) MS thesis, Washington State University, Pullman.
10. Marston PL and Langley DS (1980) Glory and depolarization in backscattering from air bubbles. J Opt Soc Am 70: 1607.
11. Davis GE (1955) Scattering by an air bubble in water. J Opt Soc Am 45: 572-581.
12. Chýlek P, Kiehl JT, Ko MK, and Ashkin A (1980) Surface waves in light scattering by spherical and non-spherical particles. In Scheuerman D, ed. Light scattering by irregularly shaped particles, p 153 New York: Plenum.

13. Wiscombe WJ (1980) Improved Mie scattering algorithms. Appl Opt 19: 1505-1509.
14. Zelmanovich IL and Shifrin KS (1968) Tables of light scattering part III. Leningrad: Hydrometeorological Publishing House.
15. Khare V and Nussenzveig HM (1977) Theory of the glory. Phys Rev Lett 38: 1279-1282.
16. Nussenzveig HM and Wiscombe WJ (1980) Forward optical glory. Opt Lett 5: 455-457.
17. Keller A (1972) The influence of the cavitation nucleus spectrum on cavitation inception. J Basic Eng 94: 917-925.
18. Ben-Yosef N, Ginio O, Mahlab D, and Weitz A (1975) Bubble size distribution measurement by Doppler velocimeter J Appl Phys 46: 738-740.
19. Marston PL (1980) Rainbow phenomena and the detection of nonsphericity in drops. Appl Opt 19: 680-684.

Figure Captions

Fig. 1 Scattering efficiency from Mie theory as a function of the size parameter x . The solid curve is for drops and the dashed curve is for bubbles.

Fig. 2 Ray paths for a bubble with $m = 3/4$. The number of internal chords p is given a prime if the ray enters the bubble below the center-line.

Fig. 3 Logarithm (base 10) of the normalized scattered intensity predicted by Mie theory (solid curve) for $x = 100$. The dashed curve is the physical-optics approximation [6] of the coarse structure.

Fig. 4 Like Figure 3 but with a linear scale and $x = 10\,000$.

Fig. 5 Photographs of far-field scattering for (a) the bubble radius $a = 480\text{ }\mu\text{m}$ ($x = 6360$, $\theta = 1.8^\circ$) and $j = 2$; (b) $a = 330\text{ }\mu\text{m}$ ($x = 4370$, $\theta = 2.2^\circ$) and $j = 1$. The critical scattering angle ϕ_c is near the left edge of the photograph; ϕ decreases from left to right. Coarse structure is manifest as broad vertical bands. The rings are artifacts.

Fig. 6 Normalized Mie backscattering from a spherical air bubble in water ($m = 3/4$) plotted as a function of the size parameter x ; for green light, $a = 200\text{ }\mu\text{m}$.

Fig. 7 Normalized Mie near-backscattering (a) and near-forward scattering (b) for $m = 3/4$ and $x = 3040$. For clarity, the computed $I^{(2)}$ was multiplied by two in (a) before plotting. The inserts illustrate some of the significant rays.

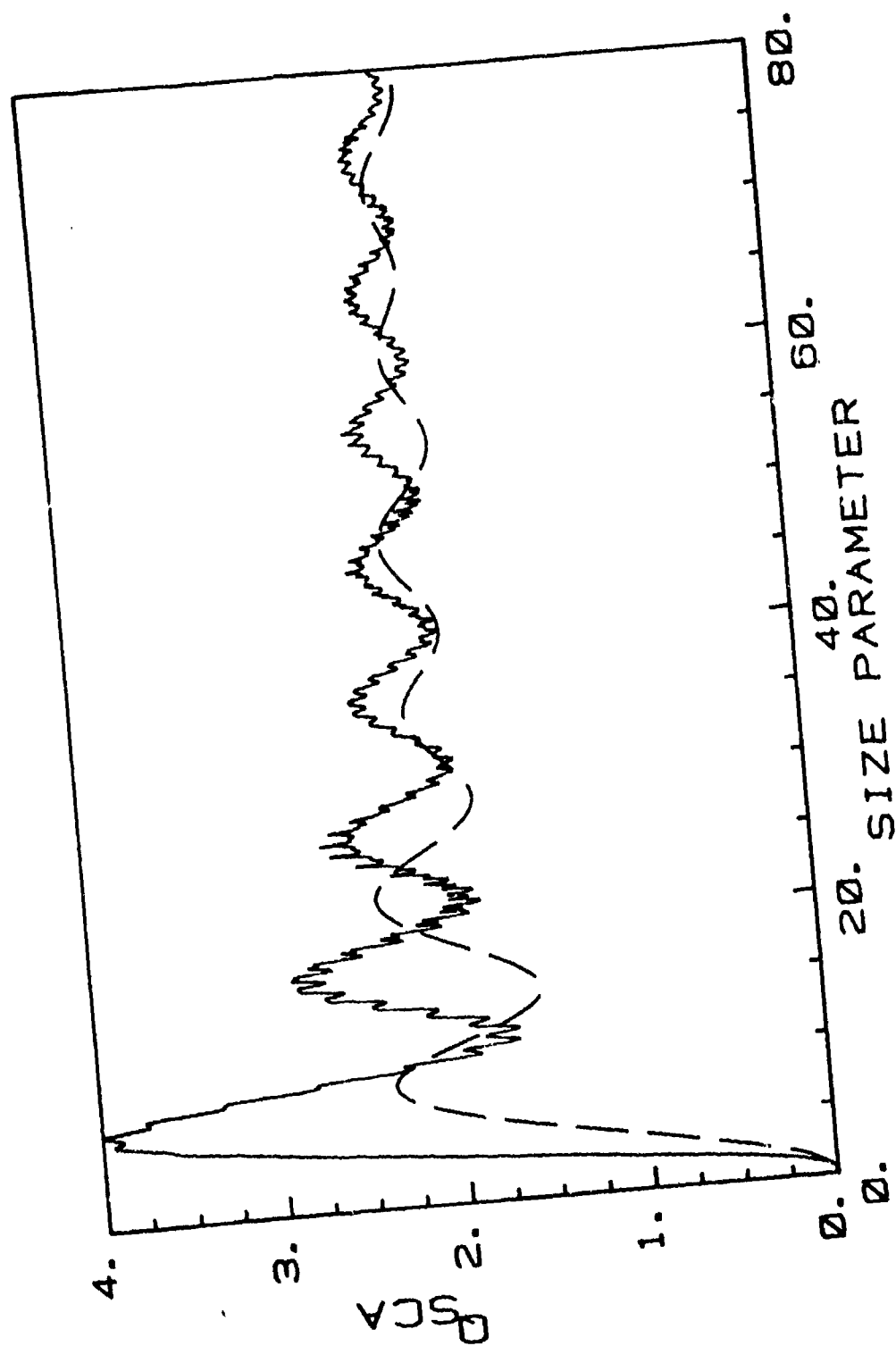


Fig. 1

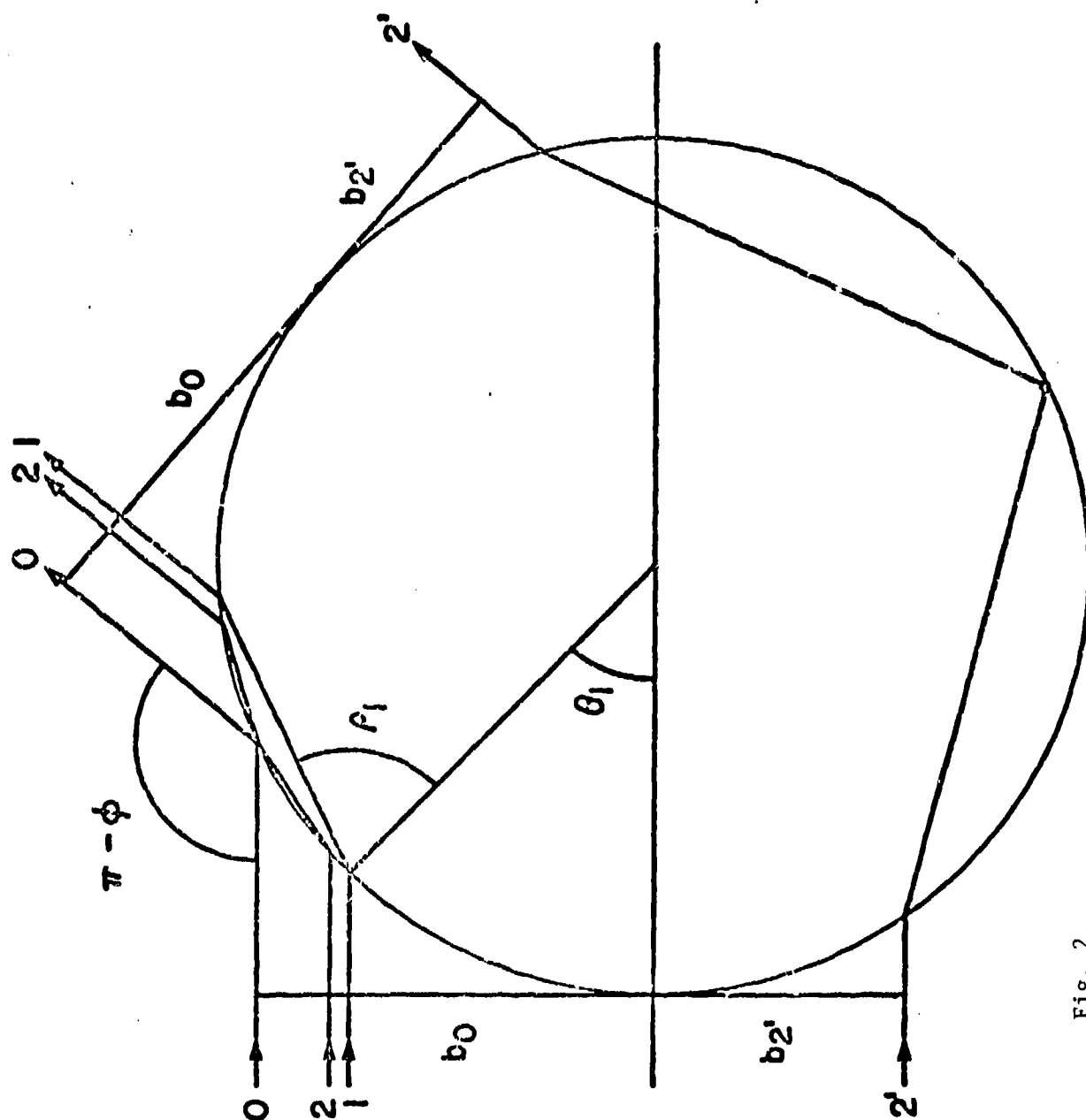


Fig. 2

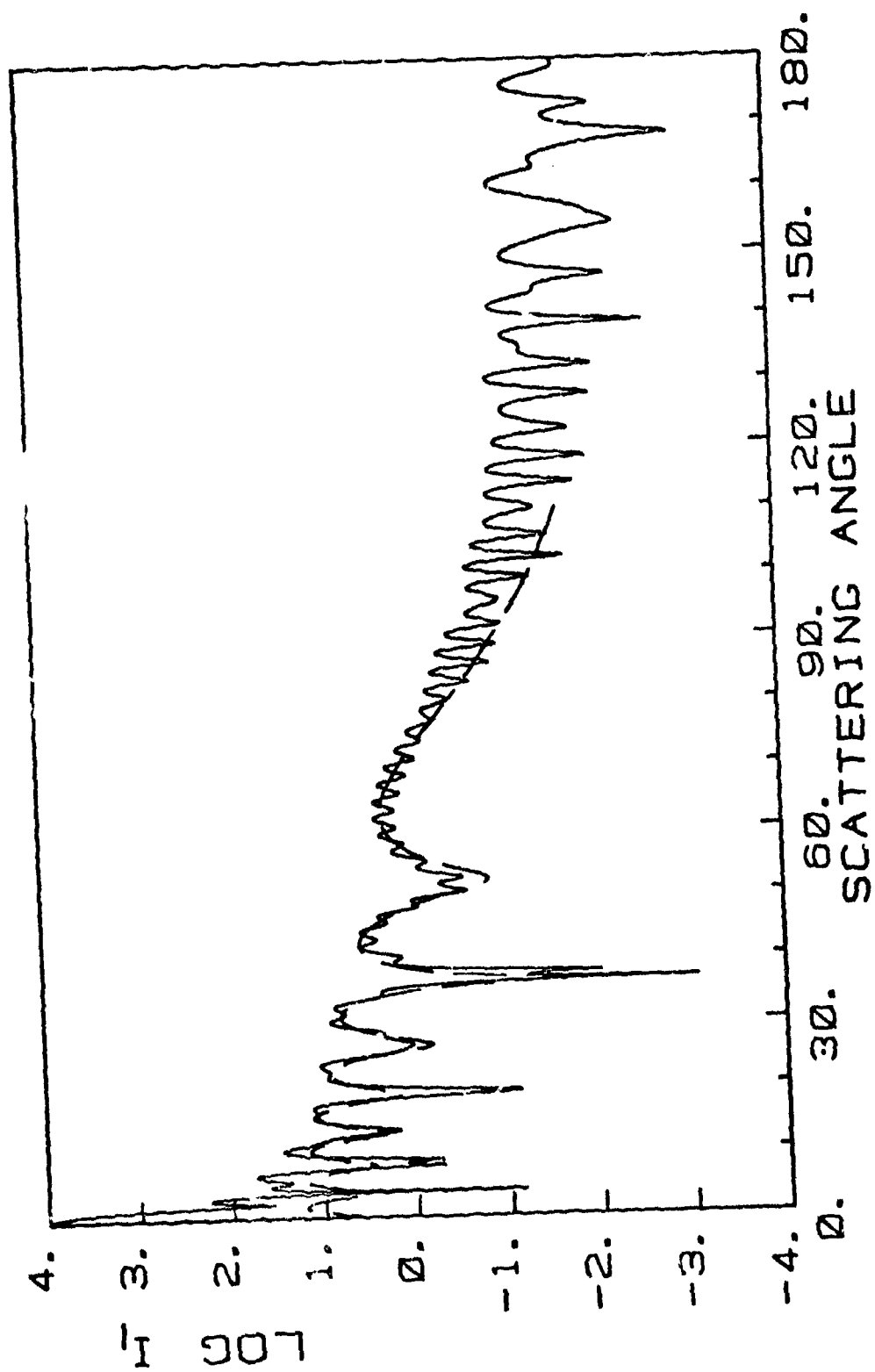


Fig. 3

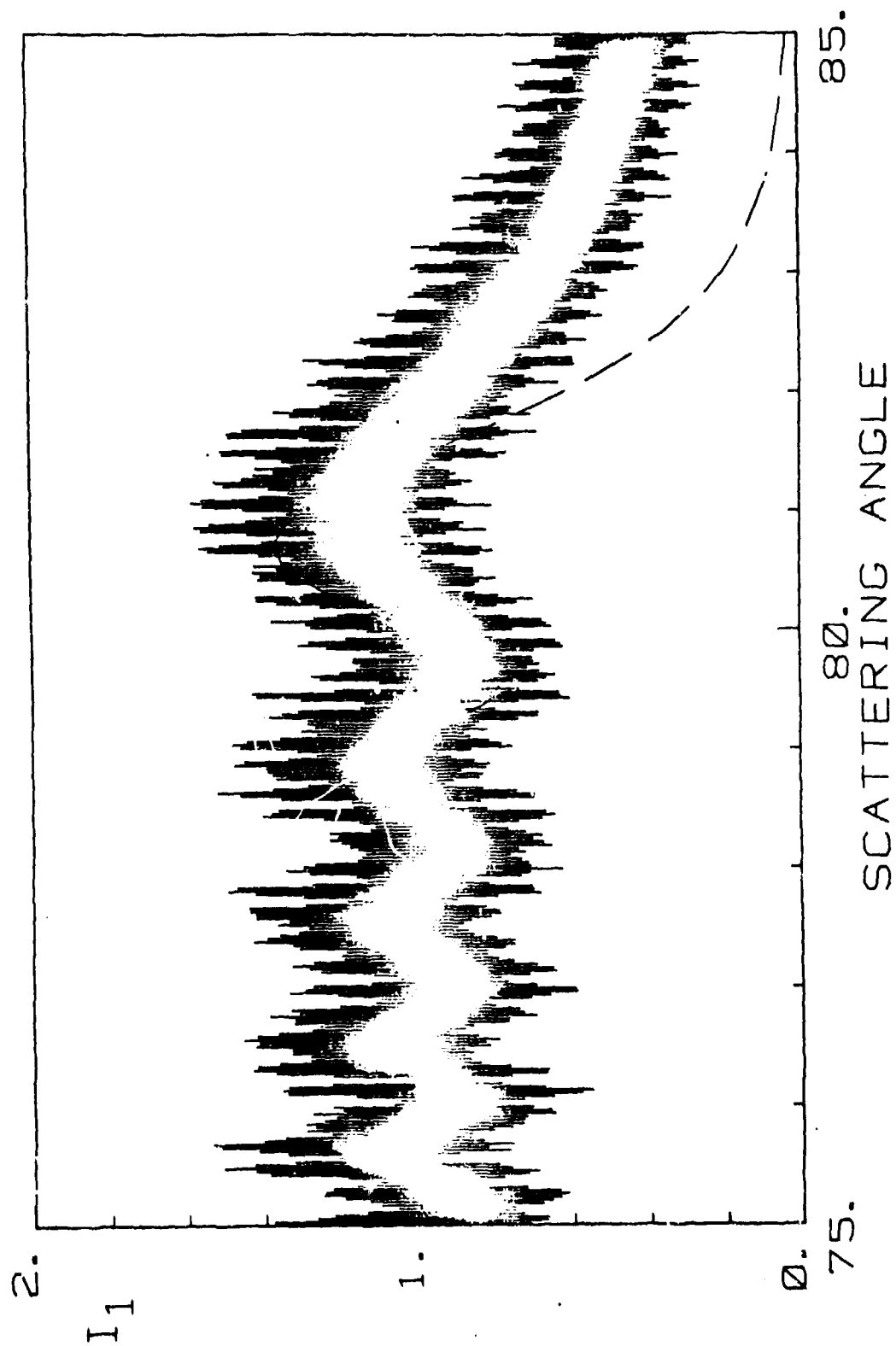


Fig. 4

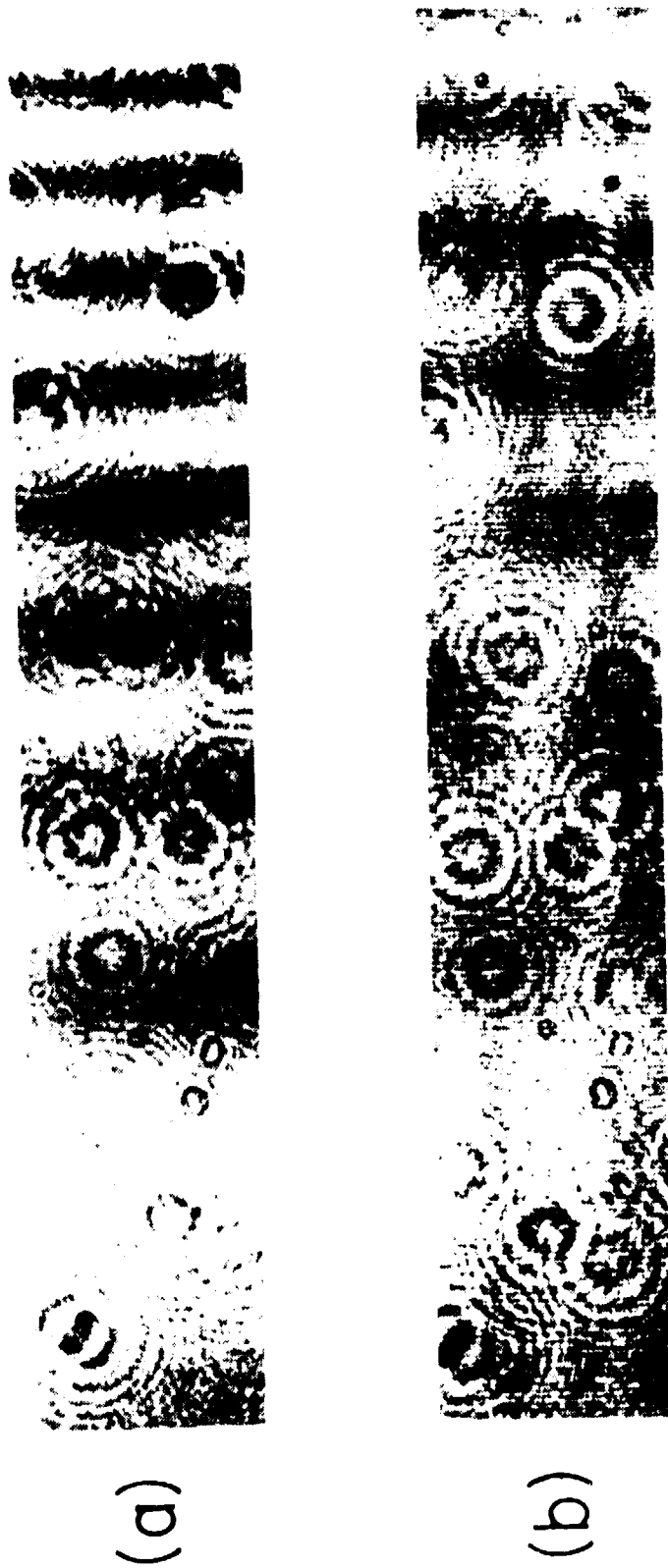


Fig. 5

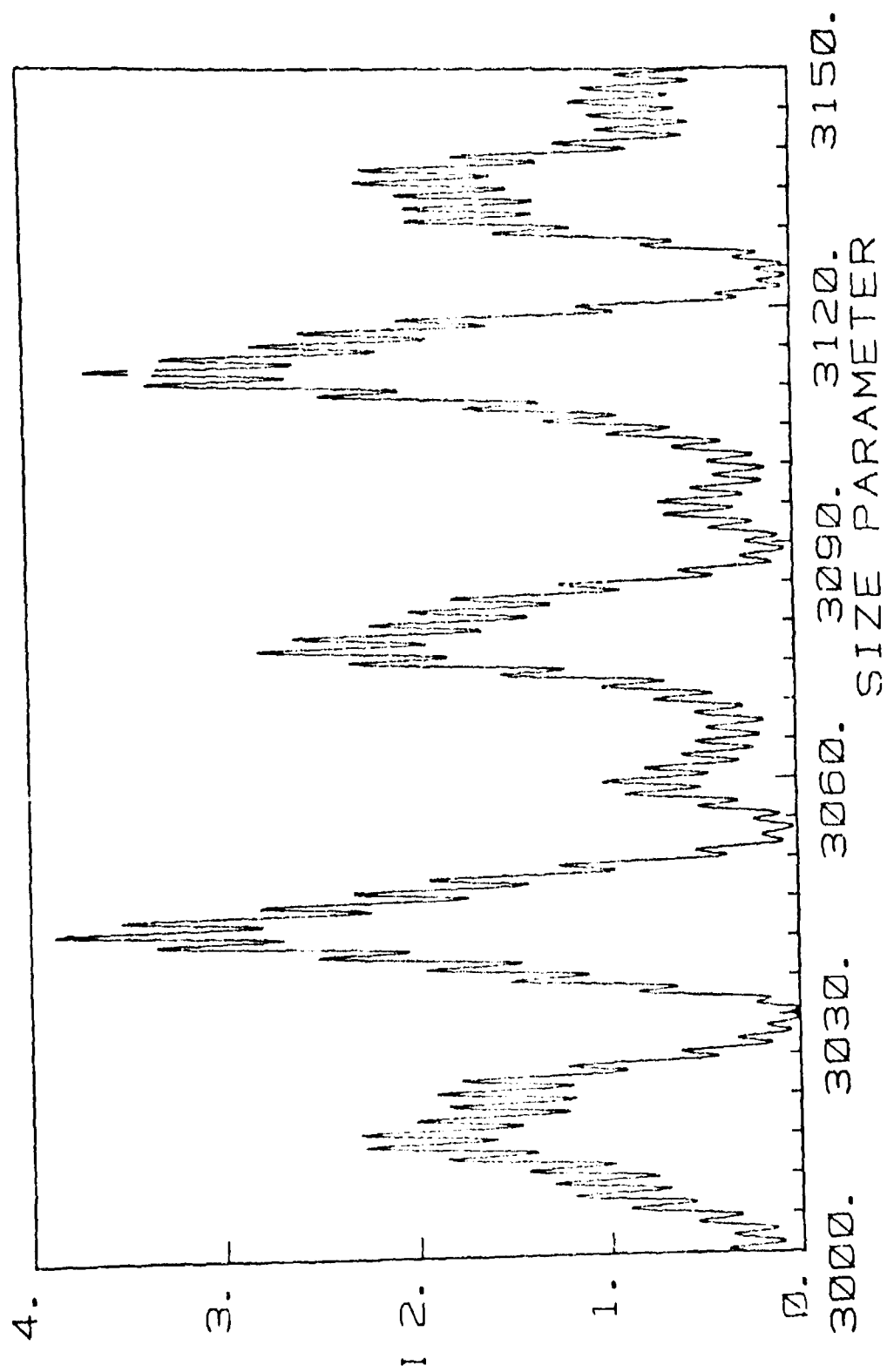


Fig. 6

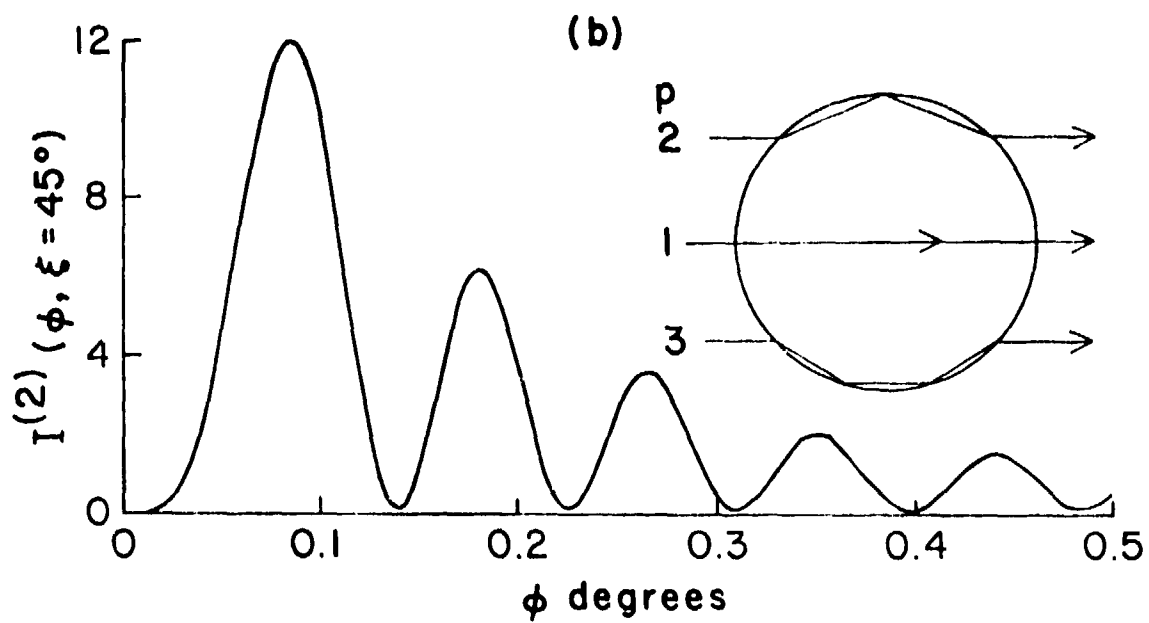
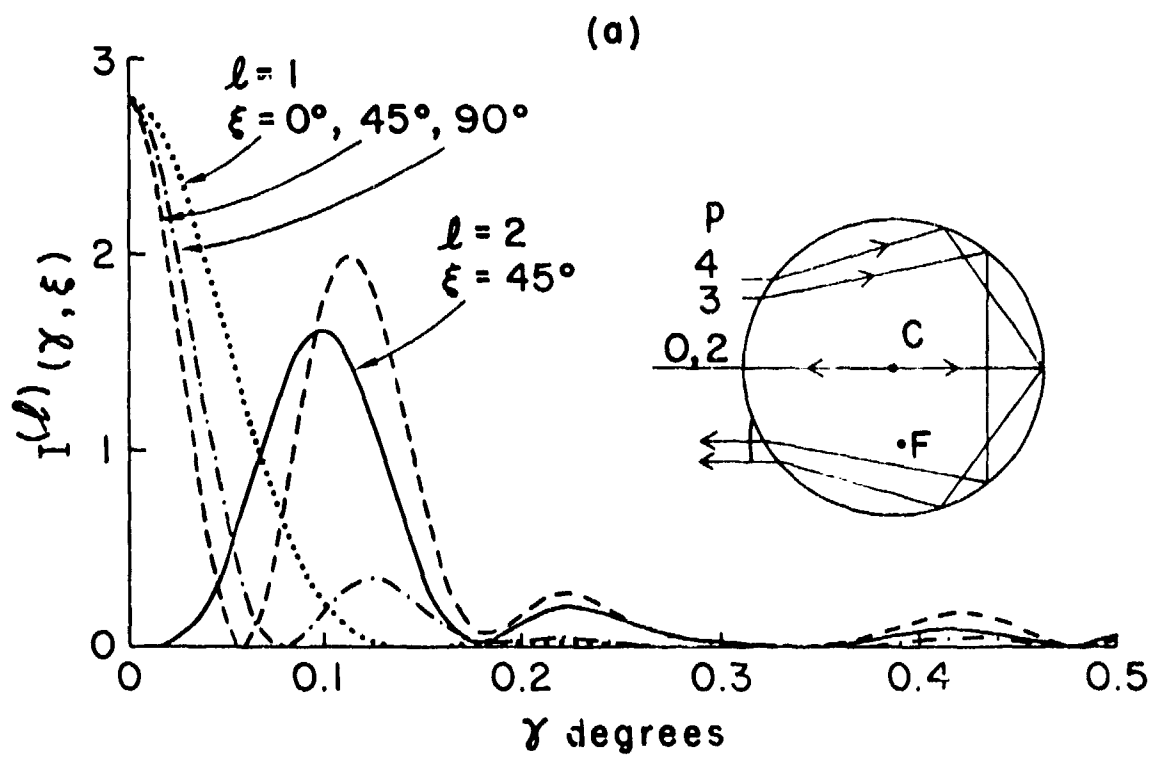


Fig. 7

Critical angle scattering by a bubble: physical optics approximation and observation (P. L. Marston) *J. Opt. Soc. Am.* 69, 1205-1211 (1979) [An error in transcription, noted in an Erratum published in *J. Opt. Soc. Am.* 70, 353(1980), has been corrected in this reproduction.]

Critical angle scattering by a bubble: physical-optics approximation and observations

Philip L. Marston

*Department of Physics, Washington State University, Pullman, Washington 99164**

Department of Engineering and Applied Science, Yale University, New Haven, Connecticut 06520

(Received 3 February 1979)

The intensity of light scattered by an air bubble in water is predicted by the geometric-optics calculation of Davis (1955) to have a divergent angular derivative as the critical scattering angle ϕ_c is approached. Effects of diffraction in the angular region near ϕ_c are described here. The Fraunhofer diffraction for scattering angles $\phi \ll \phi_c$ is estimated using a simplified physical-optics approximation. A ringing and decay of the far-field intensity is predicted that is formally similar to the near-field diffraction of a straight edge. Observation of millimeter-radius bubbles in water with collimated monochromatic illumination confirms the existence of this ringing which has a quarter period ~ 25 mrad. The diffraction calculation gives an approximate description of the relative ϕ of the observed maxima and minima. Fringes with a lower contrast and spacing ~ 0.3 mrad were also observed; they appear to be caused by the interference of rays with distinct paths. Implications for the critical angle scattering of white light are discussed.

INTRODUCTION

The purpose of this paper is to present measurements and an approximate theoretical description of diffraction phenomena observed when light is scattered near the critical angle from a bubble with an interior refractive index less than that of the outer media. The optical wavelength is assumed to be very much less than the radius of the nearly spherical bubble. Approximations given here concerning the behavior

of the reflection coefficient and the extent of emerging wave front yield an expression for the scattering in the far field that is similar in form to the Fresnel (near field) diffraction by a straight edge. Observations reported here of the scattering by a bubble in water support some aspects of this simplified theory. The treatment may be readily extended to include scattering from other curved surfaces such as that of a cylinder, provided that the principle radii of curvature are much greater than the wavelength of light.

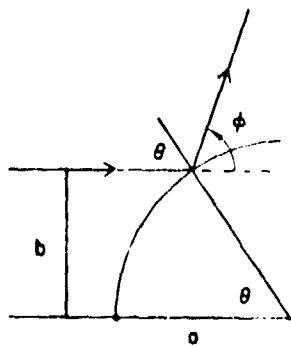


FIG. 1. Total reflection in the plane of scattering of a ray with an impact parameter b larger than the critical impact parameter b_c . Only one quadrant of the cross section of the bubble is shown.

Davis¹ calculated the angular distribution of the intensity of light scattered by an air bubble in water from a collimated incident beam. The calculation was based on geometric optics and the Fresnel reflection coefficients of light at plane interfaces; calculations of this type contribute an approximation that is useful only when the radius of the bubble a is very much greater than the wavelength in the outer media.² Let the scattering angle ϕ of a ray denote the deviation angle of the scattered ray from the direction of the incident parallel beam of rays (see Fig. 1). A significant feature of Davis' calculation is that there should be an abrupt decrease in the scattered intensity when the scattering angle ϕ exceeds ϕ_c , where

$$\phi_c = \pi - 2\theta_c, \quad (1)$$

$$\sin\theta_c = n^{-1}, \quad (2)$$

and $n = (n_o/n_i) > 1$, n_o and n_i being, respectively, the refractive indices of the outer and the inner media.

Figure 1 illustrates the physical origin of this predicted decrease. Consider how the angle of incidence at the bubble's surface θ varies as the impact parameter of the ray b increases. Rays with an impact parameter in excess of a critical value b_c have $\theta > \theta_c$, where θ_c , given by Eq. (2), is the critical angle for a plane interface. According to the geometric optics approximation, rays with $b > b_c = a \cos \theta_c$ ($\theta_c > 2$) will be totally reflected. Rays with $b < b_c$ will be partially reflected according to the magnitude of the Fresnel reflection coefficients and this partial reflection leads to the abrupt decrease in the scattered intensity for $\phi > \phi_c$. Davis' calculated scattering intensity also includes the multiple reflection and transmission of the rays with impact parameters $b > b_c$. The rays that penetrate the sphere and are partially reflected contribute to scattering for the entire range of ϕ ; however, they do not obscure the distinct decrease in the scattered intensity for $\phi > \phi_c$. This is evident from resulting prediction (Eq. 18 of Ref. 1) for the intensity of an air bubble in water that has $\phi_c \approx 82.8^\circ$; it is also evident in the corresponding predictions for bubbles in other liquids (Fig. 5 of Ref. 2). The intensity contribution of the multiply reflected and refracted rays will be omitted in the treatment presented here since we are considering only the effects of diffraction on the scattered intensity for small $|\phi - \phi_c|$.

The calculations of Davis predict that $dI/d\phi$ is discontinuous at ϕ_c , where $I_s(\phi)$ is the total scattered intensity. Diffraction of light will not permit $dI_s/d\phi$ to be discontinuous. The method presented here is a simple method for estimating the effects of diffraction in the region where $|\phi - \phi_c|$ is small. First, the approximate shape of the virtual wave front is cal-

culated geometrically for those rays with $b > b_c$. Rays with $b < b_c$ will be omitted (see Sec. II). The virtual wave front is then modified by a phase correction due to the phase shift of the unimodular Fresnel amplitude reflection coefficients for $b > b_c$. The modified wave front describes the apparent source viewed by an observer far from the bubble; the Fraunhofer diffraction of this wave gives the desired approximations for the scattering amplitude and intensity.

The wave front is assumed to extend over a half plane and is not limited by the finite size of the bubble. This treatment resembles Airy's³ diffraction correction to Descartes' geometric optics treatment of the rainbow caustic.^{4,5} Even though Airy's approximation considers the virtual wave front to be of infinite extent (and a drop must be finite), it is useful for the dominant polarization when the radius of the sphere exceeds the wavelength by a factor of approximately 200.^{4,5} It is anticipated that a more stringent criterion may delineate the range of applicability of the approximations presented here for diffraction by a bubble in the region of critical angle.

Measurements of the scattering of white light by an air bubble in water are reported by Gilson (Fig. 4 of Ref. 7). They substantiate the prediction of geometric optics of a rapid decrease in I_s for $\phi > \phi_c$; the use of white light and the limited angular resolution of the measurements make them unsuitable for comparison with the diffraction theory. The observation with laser illumination reported here in Sec. IV indicates that the simple diffraction theory gives a fair description of the relative positions of the maxima and minima of the intensity in the region of critical angle scattering.

I. CURVATURE OF THE VIRTUAL WAVE FRONT

Figure 2 illustrates a Cartesian coordinate system used in the description of the virtual wave front. The origin is chosen to be the point where the ray with $b = b_c$ contacts the sphere and the x axis is parallel to the incident ray. Points (x, y) on the virtual wave front are obtained by extending the geometrically determined scattered ray backward a distance h from the point of initial contact. In this coordinate system, the surface of the bubble in the plane of scattering is described by the point (x', y') where $h = (a^2 - b^2)^{1/2} = (a^2 - b_c^2)^{1/2} \{1 - (b - b_c)^2/a^2\}^{1/2}$, and a is the radius of the bubble. Calculation of the slope m of the scattered ray gives the following parametric equations for the virtual wave front:

$$x = h[1 - (1 + m^2)^{-1/2}], \quad (3)$$

$$y = h[1 - m(1 + m^2)^{-1/2}], \quad (4)$$

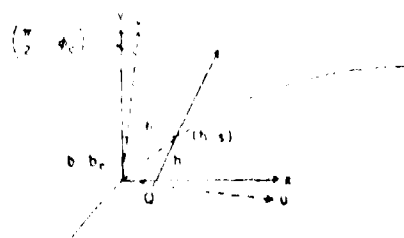


FIG. 2. Illustration of the geometric procedure for locating the coordinates (x, y) of a point Q on the curved virtual wave front. The upper line of length h is parallel to the x axis; h is also the distance between its point of contact with the bubble surface (point $(b, 0)$) and the point Q . The rotated coordinate axes are introduced to facilitate a Taylor expansion of the wave front.

$$m = \tan \phi = \tan[2 \cos^{-1}(b/a)]. \quad (5)$$

The calculation of the diffraction is facilitated by describing virtual wave fronts using coordinates (u, v) which have the same origin but are rotated clockwise by an angle $(\pi/2) - \phi$, so that the positive v axis is the path of the scattered critical ray predicted by geometric optics. Equation (4) and the rotation transformation give the following expression for the new coordinates of the virtual wave front:

$$u = x \sin 2\theta_c + y \cos 2\theta_c, \quad (6)$$

$$v = -x \cos 2\theta_c + y \sin 2\theta_c. \quad (7)$$

To obtain a Taylor expansion of $v(u)$ about $u = 0$, the following derivatives were computed for $\theta = \theta_c$: $dv/du = p/q$ and $d^2v/du^2 = q^{-1}dp/d\theta + pq^{-3}dq^{-1}/d\theta$ where $p(\theta) = dv/d\theta$ and $q(\theta) = du/d\theta$. The calculation of p and q used the relation $b = a \sin \theta$ which is evident from Fig. 1. The term of the Taylor series which is linear in u vanishes because of the coordinate rotation; this is evident since $p(\theta_c) = 0$ and $q(\theta_c) = a \cos \theta_c$. Omission of cubic and higher order terms in the Taylor series gives

$$v = \alpha u^2, \quad (8)$$

$$\alpha = -1/a \cos \theta_c. \quad (9)$$

For the case of an air bubble in water, numerical calculations show that Eq. (8) is within 10% of the value of $v(u)$ predicted by Eqs. (1)–(7) provided that $0 < u < 0.07a$. In the calculation of the diffraction that follows, Eq. (8) will be used for the region $u \geq 0$. (Airy's treatment of the rainbow also retains only the leading term in approximating the virtual wave front but in that case it is a cubic term.) The sign of α indicates that the reflected wave is divergent.

II. AMPLITUDE OF THE VIRTUAL WAVE FRONT

The physical optics approximation¹ involves: (i) the specification of the polarization of the incident wave; and, (ii) the use of the reflection coefficients for a plane surface to approximate the reflected fields at each point on a curved surface. In the application of the technique that follows, the incident wave has an electric field polarization either entirely perpendicular to the plane of scattering or entirely parallel to it; a subscript j will be assigned the value 1 in the first case and 2 in the second. (A linear combination of reflected fields may be used for other incident polarizations.) To a distant observer, the reflected wave appears to come from a virtual wave described by the following complex amplitude at points on the u axis:

$$U(u, t) = r_j e^{i(k\omega u^2 - \omega t)}, \quad (10)$$

where: $t = \sqrt{\epsilon - 1}$, ω is the angular frequency, t is the time, $k = 2\pi/\lambda$, λ is the wavelength in the outer medium, and r_j is the amplitude reflection coefficient of a plane surface for the angle of incidence θ :

$$r_1 = \frac{\cos \theta - (n^{-2} - \sin^2 \theta)^{1/2}}{\cos \theta + (n^{-2} - \sin^2 \theta)^{1/2}}, \quad (11)$$

$$r_2 = \frac{-n^{-2} \cos \theta + (n^{-2} - \sin^2 \theta)^{1/2}}{n^{-2} \cos \theta + (n^{-2} - \sin^2 \theta)^{1/2}}. \quad (12)$$

Reflection for $b \geq b_c$ where $b_c = b < a$ can be described by the following approximations that give the leading dependence

of r_1 and r_2 on $\epsilon - \theta_c - \theta \geq 0$:

$$r_1 \approx 1 - (8\epsilon/n \cos \theta_c)^{1/2}, \quad (13)$$

$$r_2 \approx -1 + n^2(8\epsilon/n \cos \theta_c)^{1/2}, \quad (14)$$

and in each case $|dr/d\theta| = \epsilon^{-1/2}$. When $\theta > \theta_c$, the reflection coefficients are unimodular and complex; they are $r_1 = \exp(-i\delta_1)$ and $r_2 = -\exp(-i\delta_2)$ where²:

$$\tan(\delta_1/2) = (\sin^2 \theta - n^{-2})^{1/2} / \cos \theta, \quad (15)$$

$$\tan(\delta_2/2) = n^2 \tan(\delta_1/2). \quad (16)$$

Reflection for $b \geq b_c$ where $b = b_c \ll a$ can be described by the following approximations that describe the leading dependences of δ_1 and δ_2 on $\epsilon' = \theta - \theta_c \geq 0$:

$$\delta_1 \approx (8\epsilon'/n \cos \theta_c)^{1/2}, \quad (17)$$

$$\delta_2 \approx n^2(8\epsilon'/n \cos \theta_c)^{1/2}. \quad (18)$$

Approximations for r in terms of u may be obtained using $\theta - \theta_c \approx u/q(\theta_c)$. For $u \geq 0$, Eqs. (17) and (18) give $\delta_j \approx \beta_j u^{1/2}$ where

$$\beta_1 = (8/n a)^{1/2} / \cos \theta_c, \quad (19)$$

$$\beta_2 = n^2 \beta_1. \quad (20)$$

The specification of $U(u, t)$ is further simplified by taking $r_1 = r_2 = 0$ for $\theta < \theta_c$, and equivalently for $u < 0$; the use of this approximation is motivated by the divergences $|dr/d\theta|$ and $d\delta_j/d\theta$ as $\epsilon' \rightarrow \pm 0$ and $\phi = \phi_c \pm 0$, respectively.

III. FRAUNHOFER DIFFRACTION PATTERN

The scattering amplitude at large distances from the bubble is proportional to the Fourier transform of $r_j \exp(-ik\omega u^2)$:

$$f_j(\eta) = \int_{-\infty}^{\infty} r_j(u) e^{i(k\omega u^2 - \eta u)} du, \quad (21)$$

where $\eta = \phi_c - \phi$ (an angle of the observation point relative to ϕ_c) is assumed to be small so that $\sin \eta \approx \eta$; and constant magnitude multiplicative factors that precede the integral have been omitted. The approximation described in the preceding sections yield the following expression for f_j :

$$f_j = \pm \int_0^{\infty} e^{-i(k\omega u^2 + \eta u + \beta_j u^{1/2})} du, \quad (22)$$

where, here and in the equations that follow, the upper sign is for polarization $j = 1$ and the lower one is for $j = 2$.

Evaluation of Eq. (22) is facilitated by a change of variables that completes the partial square formed by $(\omega u^2 + \eta u)$. Define $z = (4\omega/\lambda)^{1/2} u = u$ where

$$u = \eta[(a/\lambda) \cos \theta_c]^{1/2} z. \quad (23)$$

We will approximate the integral only for $0 < \phi < \phi_c$ which corresponds to the region predicted by geometric optics to be strongly illuminated; this restriction gives $u \geq 0$. Equation (22) may then be written as follows: $f_j = \pm (\lambda a \cos \theta_c)^{1/2} g/2$, where

$$g = e^{i\psi} \int_0^{\infty} e^{-i(\psi_j(z, u) + k\eta^2/4\omega)} e^{-i(\omega/2)z^2} dz, \quad (24)$$

$$\psi_j(z, u) = \beta_j z^{1/2} [(u + z)^{1/2} - u^{1/2}] (\lambda a \cos \theta_c)^{1/4}. \quad (25)$$

In the exponential that precedes the integral, $\psi_j(u,0)$ is evaluated by the appropriate variable substitution in Eq. (25), (0 replaces w and w replaces z); physically, $-\psi_j(u,0)$ is the approximate phase shift associated with r_j of the geometric ray scattered to the observation angle ϕ . The second term in this exponential arises from the completion of the square.

We now examine the condition for omitting the $\exp[i\psi_j(z,u)]$ factor within the integral; when this simplification is permissible, the integral may be estimated using Fresnel integrals. If $\psi_j(z,u)$ is a sufficiently slowly varying function of z , the principle contribution of the integrand occurs when $|z| \leq 2$ because the phase of $\exp[i(\pi/2)z^2]$ is stationary at $z = 0$. (For a lucid discussion of stationary phase approximations, see Segel.¹⁹) For $u > 0$, $z \geq u$, and $z^2 \geq |z|$, it is evident that $|\psi_j(z,u)| \leq \psi_j(z,0)$, consequently the factor in question may be omitted if the radius of the bubble is sufficiently large that $\psi_j(2,0) \ll 1$. For example, water has $n \sim 1.333$ and visible light from a He-Ne laser has a wavelength in water of $n^{-1}0.6328 \mu\text{m}$. For polarization 1 this condition on $\psi_j(2,0)$ gives $(a/590 \mu\text{m})^{1/3} \gg 1$ and for polarization 2 it gives $(a/590 \mu\text{m})^{1/3} \gg 1$ where Eqs. (2), (19), (20), and (25) have also been used.

After some rearranging, the result of this approximation may be written as follows:

$$g = e^{i[\psi_j(u,0) + k_0 u^2/4]} [F(u) - F(-\infty)], \quad (26)$$

where $F(u)$ is Fresnel's integral¹⁰:

$$F(u) = \int_0^u e^{i(\pi/2)z^2} dz = C(u) + iS(u), \quad (27)$$

$$C(u) = \int_0^u \cos\left(\frac{\pi}{2}z^2\right) dz, \quad (28)$$

$$S(u) = \int_0^u \sin\left(\frac{\pi}{2}z^2\right) dz, \quad (29)$$

and $C(-\infty) = S(-\infty) = -1/2$. For any state of incident polarization, the following factor gives the dependence of the intensity on η where g^* is the complex conjugate of g :

$$gg^* = [C(u) + 1/2]^2 + [S(u) + 1/2]^2. \quad (30)$$

The normalization used in Eqs. (21) and (30) is such that $gg^* \rightarrow 2$ as $(\phi_r - \phi)$ becomes large and positive. As expected, $gg^* \rightarrow 0$ as $\phi_r - \phi$ becomes large and positive, however, the region $w < 0$ is out of the range of the validity test for the approximation used in deriving Eq. (30).

Davis' analysis¹ of the geometric scattering may be used to obtain the normalization required to express the absolute intensity I associated with the reflected ray at a distance $R \gg a$ from the center of the bubble:

$$I \approx I_0(a/R)^2 gg^*/8, \quad (31)$$

where I_0 is the incident intensity and $gg^*/8 \rightarrow 1/4$ for large u so that Eq. (31) coincides with Eq. (3) of Ref. 1 in the appropriate limit. Furthermore, if the interference between the totally reflected rays and the multiply reflected rays are omitted, the total intensity I_t becomes

$$I_t = I_0(a/R)^2 [gg^*/8 + G'(u)], \quad (32)$$

where $G'(u)$ is the total contribution by the multiply reflected rays. For an air bubble in water, illuminated by unpolarized

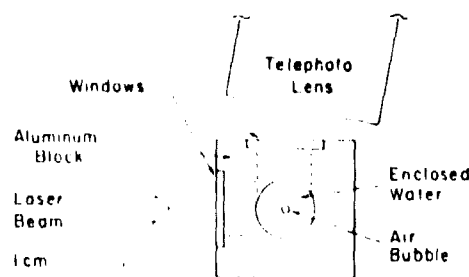


FIG. 3. View of the apparatus in the plane of scattering which was horizontal in the laboratory. The bottom of the bubble was in contact with a needle that prevented the bubble from floating out of the scattering plane. The top of the bubble (which is the side displayed here) was viewed by a microscope. The wavelength in air of the illumination was 632.8 nm.

light, Table III of Ref. 1 shows that G' is a smooth function of ϕ for ϕ near π , and that $G'(u = 82.3^\circ) \approx 0.0027$ and $G'(75^\circ) \approx 0.0010$. Consequently G' for an air bubble in water is approximately 1% to 2% of the asymptotic value of $gg^*/8$.

Equation (30) is similar in form to the well-known¹⁰ Fresnel (near field) diffraction by a straight edge where the parameter u is, in that case, proportional to the lateral displacement of the observation point from the edge of the geometric shadow. For both cases, in the region $u > 0$ the intensity is predicted to oscillate with an oscillation amplitude that decreases rapidly with increasing u . This behavior is predicted for the far-field intensity of a bubble because of the abrupt variation in the amplitude of the virtual wave front near the critical angle and because of the curvature of this wave front induced by the reflection from the curved surface.

From the aforementioned bound on $|z|$ for the principle contributions of the integral in Eq. (24), we can estimate for the w region of interest, the errors introduced in the calculation of the δ_j from Eqs. (19) and (20). In the interval $0 < u < 3$, Eq. (30) predicts two intensity maxima. In this region the principle contributions occur with $0 < u \leq u_{\text{max}} \approx (1 + u)(-\lambda^2/a)^{1/3}$ with $u_{\text{max}} \approx 3$. With the aforementioned λ and with $a = 1$ mm, this estimate gives $u_{\text{max}} \approx 53 \mu\text{m}$. A comparison of Eq. (17) with δ_1 calculated using Eq. (19) and this u shows that the error introduced in δ_1 is less than 3%. A similar comparison of Eqs. (18) and (20) give a bound for the error in δ_2 of 8%. Consequently the use of $\delta_j \approx \delta_j u^{1/3}$ is justified. Furthermore, since $u_{\text{max}} \ll a$, the upper limit of integration in Eq. (27) should have a useful approximation. The main justification for the approximations described in Secs. II-III is the comparison with experiments described in the section that follows.

IV. OBSERVED SCATTERING

This section describes photographic observations of the critical angle variations in the scattered intensity predicted in the previous section. Figure 3 shows a diagram of the apparatus. Distilled water was placed in an aluminum container. The inner walls of the container had been blackened so that they absorbed much of the stray light. A steel needle passed vertically through a rubber septum in the bottom of the container. The other end of the needle was connected to a syringe that contained air. Horizontal holes 1.9 cm in diameter passed through the walls of the container at right an-



30 milliradians

FIG. 4. Photograph of the critical angle for total diffraction from a 2.15-mm-diam bubble. The scattering angle θ decreases from left to right. The vertical bands have a characteristic separation of approximately 25 mrad; the variation in the intensity of the bands is caused by diffraction. The incident beam was polarized with its electric field parallel to the scattering plane.

gles. These holes were sealed with O-rings to prevent water leaks and were covered by antireflection coated windows. A bubble could be created at the flat tip of the needle by decreasing the volume of the syringe; this bubble was stable provided its volume was kept sufficiently small. The bubble was approximately spherical in its central region. (For a discussion of the stability of bubbles suspended from needles, see Ref. 11.) The base of the bubble was in contact with the needle during the observation.

The polarized beam from a 6 mW He-Ne laser was expanded to produce an 8-mm diam parallel beam. The expanded beam passed normally and horizontally through one of the windows in such a way that the central rays of the beam passed close to the center of the bubble. A camera viewed the bubble through the second window. The needle and the inner wall of the aluminum container were blackened to reduce the intensity of stray light that would have otherwise obscured the scattering of the bubble. Light scattered by the bubble near the critical scattering angle had an angle of incidence at the water-in-window interface of approximately 90° ($\theta = \pi/2$). This light is refracted at the window-air interface. The camera telephoto lens (Nikkor Q, manufactured by Nikon, Inc.) had an effective focal length F of 200 mm. The lens was placed with its axis horizontal and approximately parallel to the refracted critical rays. The polarization of the incident monochromatic light was usually chosen with the electric field parallel to the scattering plane that corresponds to $\epsilon = 0$ in the preceding analysis. This choice for the polarization gives the greatest magnitude for the coefficient of ϵ^2 in Eq. (11). Consequently it gives the most rapid decrease for $|r_\epsilon|$ with increasing ϵ and it should be the polarization for which the omission of the wave front with $u < 0$ in Eq. (22) will produce the smallest error in the predicted scattering. The diameter of the bubble in the scattering plane was measured with a microscope located in the air directly above the bubble.

Photographs were taken with the camera lens focused to

infinity so that the film plane was at the optical transform plane of the lens. Let $\eta = \phi_0' - \phi$, where ϕ' and ϕ_0' denote the angles of the rays outside the cell that correspond to ϕ and ϕ_0 in the water. Consequently increments in the distance l on the photographic negative are related to the increments $\Delta\eta$ by $\Delta\eta = \Delta l/F$ for $M \gg F$. Numerical calculation of the refraction at water-glass and the water-air interfaces show that increments in η may be related to the corresponding $\Delta\eta'$ by $\Delta\eta = \theta\Delta\eta'$ with a negligible error. The success of this method relies on the choice of the plane of the viewed window such that it is nearly perpendicular to the critical ray. These results may be combined to give $\Delta\eta = \Delta l/nF$. [Of course, if the entire region external to the sphere had been uniform so that no window was needed, it would not be necessary to invoke these approximations. Then $\Delta l/nF$ could be used as the transform parameter in Eq. (21) because of the Fourier transform properties of a lens.¹²]

Figure 4 is a positive reproduction of a photograph of the critical angle scattering with a bubble diameter of 2.15 ± 0.05 mm. The scale indicates a $\Delta\eta$ relative to an arbitrary reference η . The film used was Tri-X with an exposure time of 1/60 sec. The broad vertical dark bands with a characteristic spacing of approximately 25 mrad ($\approx 1.4^\circ$) are examples of the intensity maxima predicted by Eq. (32). The concentric circular fringes that are centered close to the most central dark band are apparently an artifact associated with spurious reflection, either from the exit window or from the telephoto lens. The dark region on the left of the figure is indicative of the reduction in intensity that occurs when $u < 0$.

Microdensitometer scans were obtained from two negatives to facilitate a quantitative comparison with the theory. Figure 5 compares the relative intensity inferred from a scan of a negative for a bubble diameter of 1.65 ± 0.05 mm. Two free parameters were used for each negative to make the comparison with the theory possible: (i) The location of the geometric critical ray could not be determined experimentally

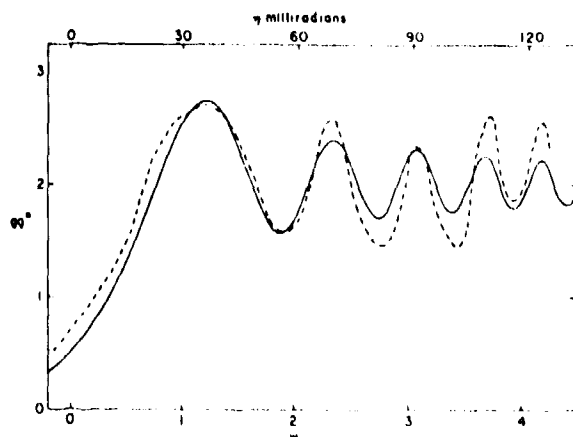


FIG. 5 The dashed curve is the smoothed relative intensity inferred from a microdensitometer scan of the photographic negative. The bubble diameter was 1.65 mm. The solid curve is given by Eq. (30) when n is the result of the physical optics approximation. Two parameters were adjusted to facilitate this comparison.

so that an arbitrary constant angle was added to the abscissa of the measured intensity profile to optimize the agreement with the theory. (ii) The absolute intensity could not be determined experimentally so that the experimental intensity I_r was obtained by multiplying measurements by a constant factor K that was selected to optimize agreement with Eq. (30). The magnitude of G' was sufficiently small that it was neglected in the computation of the theoretical prediction so that gg^* could be used as the prediction. The relationship between the measured transmittance of the negative τ and I_r is¹³:

$$I_r = K(\tau^{-1/2} - \tau_0^{-1/2}) \quad (33)$$

where τ_0 was measured at an unexposed region of the negative and the contrast index γ was estimated from manufacturer's literature to be 0.70 for the conditions of film development. The $\tau(\eta)$ measurements were smoothed by hand to reduce the magnitude of the circular fringe artifact in the inferred I_r . The scale of the smoothing only slightly exceeded the spacing of those fringes. The validity of the procedure was substantiated by comparing parallel but distinct scans from the same negative.

Figure 5 illustrates a close agreement of the relative positions of the maxima and minima of the intensity bands, with those predicted by Eq. (30). The u values were calculated using Eqs. (2) and (23) with $n = 1.3333$ and $2a = 1.65$ mm; $C(u)$ and $S(u)$ were obtained from tables. The gg^* values and locations for the maxima and minima were obtained from Fresnel's original tabulation for the description of edge diffraction (as quoted by Mascart¹⁴). There is an apparent discrepancy of this theory with the following features of the measurement: (i) there appears to be a difference of intensities in the region $u < 1$ that cannot be explained by the omission of G' from the calculation; (ii) the amplitude of the intensity oscillations exceeds the predictions for $u > 2.2$; and, (iii) there is an unexplained drop in the intensity near $u = 3$. Another negative shows qualitatively similar disagreements but also a similar agreement for the location of the maxima and minima with the theory. The quantity and quality of measurements that can be obtained with the available apparatus are not adequate for determining the deficiencies of this calculation.

A comparison of photographs taken with bubbles of differing radii shows that the angular spacing of the intensity oscillation decreases with increasing a , which is expected from the form of Eq. (23). This decrease is also evident to the eye if the radius is increased as the bubble is viewed through a telescope focused on infinity. Intensity variations similar to those displayed in Figs. 4 and 5 were also observed with the incident polarization of $j = 1$.

V. FINE STRUCTURE IN THE SCATTERING

Careful examination of the photographic negatives revealed, in some cases, an oscillation in the intensity periodic in η which was superimposed on the diffraction structure described in Sec. IV. For example, oscillations in intensity with a period of approximately 0.4 mrad are visible in the original photographic print reproduced in Fig. 4. (It is unlikely that this structure exists in the printed version appearing in this journal and it was not resolved in Fig. 5.) Examination of the negative shows that the fringe spacing η decreases with increasing a . A 100 \times long microscope was used to measure η from the negative for bubbles with $1.7 \text{ mm} \leq 2a \leq 2.2 \text{ mm}$. The resulting data could be fitted by the equation: $\eta = \Lambda/\Delta(u)$, with $\Lambda = 0.004 \pm 0.01$; however, it was difficult to obtain comparable measurements from each negative because of noise and the low contrast of the oscillations. Energy associated with certain rays incident with $b < b_c$ will eventually leave the bubble directed with $\phi \sim \phi_c$. From the linearity of the equation for η and the magnitude of Λ , it is likely that the oscillations are caused by the interference of that light with the critically reflected light; however, the number of reflections and L value for the path of this interfering light has not been determined. The separation of the major virtual sources for $\phi = \phi_c$ is $\sim \Lambda^{-1}$.

Similar closely spaced oscillations can be observed in the rainbow scattering from liquid drops with $n_i > n_o$ and monochromatic illumination. The author has found¹⁵ that their spacing η is inversely proportional to a and for drops of xylene ($n = 1.29$) in water: $\Lambda \sim 0.6$. These fringes were found to be useful for detecting micron-amplitude shape oscillations of millimeter diameter drops since changes in the drop's shape cause an angular shift in the position of these fringes. When the frequency of a few Hz, the fringes appeared to blur together and oscillations of the shape of the bubble should have caused the fine structure to blur. Indeed, bubble shape oscillations excited by room vibrations may have blurred the fringes on the negatives where none were observed to appear. These were typically 1/30 s. The similarities and differences of critical angle scattering with rainbow scattering can be seen by comparing Fig. 4 with photographs of the latter in Figs. 6 and 7.

VI. DISCUSSION

The critical angle scattering of eight bubbles was photographed, the bubble diameters were in the range 1.6–2.3 mm. Each photograph is similar in appearance to Fig. 4 in that the ringing in intensity due to the critical angle is quite visible for either state of incident polarization. Consequently there is a significant deviation to the prediction of geometric optics near the critical angle for air bubbles of this size in water.

Furthermore, the measurements of the positions of the intensity maxima and minima, measured relative to an undetermined angle, are in reasonable agreement with Eq. (30). An experimental test of several aspects of this calculation may require the use of photoelectric detectors because of limitations in the present apparatus. These include the following features: (i) the amplitude of the ringing of the intensity, (ii) the absolute positions in the maxima and minima, (iii) the rate of decay of the intensity for $w \lesssim 1$, (iv) the range of radii for which Eq. (30) may be used, and (v) quantitative measurements of the interference phenomena described in Sec. V. Unfortunately, the largeness of the bubble radii makes it impractical to calculate the Mie scattering.

A brief discussion of this use of the physical optics approximation is in order. Surface wave phenomena⁴ do not appear to be included in this calculation; Fig. 5 is evidence that they are not needed for an approximate description of these observations. Surface waves can be included in the Watson transformation method which has been used to formulate the scattering from a cavity.^{18,19} A comparison with the results in Fig. 5 has not been performed because of the complicated nature of predicted scattering amplitude [e.g., Ref. 18, Eqs. (4.92) and (4.101)]; indeed, the present author has been unable to determine if the ringing is consistent with those amplitudes. A second shortcoming of the approximations presented in Secs. I-III is that the curvature of the bubble orthogonal to the plane of scattering is omitted until Eq. (31) where its geometric effect is included in the a^2 factor.

Diffraction may have a major effect on the far field appearance of the critical angle scattering for bubbles in water illuminated by collimated white light. Let ϕ_v and ϕ_r denote respectively ϕ_c for violet and for red light. The dispersion of water and Eqs. (1) and (2) give: $\phi_v - \phi_r \sim 17$ mrad; consequently the geometrical scattering (Fig. 18 of Ref. 1), as seen through a telescope, should appear bluish in the region $\phi_r < \phi < \phi_v$. It is evident, however, from Fig. 5 that diffraction smearing of the otherwise abrupt change in intensity for monochromatic illumination will tend to reduce significantly the coloration predicted by geometric optics.

This work was motivated by an investigation of optical methods for measuring the refractive index of superheated liquid drops suspended in immiscible host liquids. At sufficiently high temperatures, such drops frequently have $n_d < n_h$ and they should exhibit critical angle scattering phenomena similar to that described for bubbles. Even though the distinctive critical angle scattering predicted by geometric optics is altered by diffraction, n may be inferred from the absolute

angles of the intensity maxima and minima, provided the present theory is found to give the *absolute* angles when n is known.

ACKNOWLEDGMENTS

The photographs described here were taken in the laboratory of R. E. Apfel at Yale University. The author wishes to thank the Department of Astronomy of the University of Washington, especially E. Manery, for the use and operation of the scanning microdensitometer. Acknowledgement is made to the Donors of the Petroleum Research Fund, administered by the American Chemical Society, and to the Office of Naval Research for partial support of this research.

*Present address.

¹G. E. Davis, "Scattering of light by an air bubble in water," *J. Opt. Soc. Am.* **45**, 572-581 (1955).

²R. J. Withington, "Light scattering by bubbles in a bubble chamber," *Appl. Opt.* **7**, 175-181 (1968).

³G. B. Airy, "On the intensity of light in the neighborhood of a caustic," *Trans. Cambridge Phil. Soc.* **6**, 379-402 (1838).

⁴H. C. Van de Hulst, *Light Scattering by Small Particles* (Wiley, New York, 1957).

⁵H. M. Nussenzveig, "The theory of the rainbow," *Sci. Am.* **236**, No. 4, 116-127 (1977).

⁶V. Khare and H. M. Nussenzveig, "Theory of the rainbow," *Phys. Rev. Lett.* **33**, 976-980 (1974).

⁷D. A. Glaser, in *Handbuch der Physik* edited by S. Flugge, Vol. 45, (Springer Verlag, Berlin, 1958).

⁸G. R. Fowles, *Introduction to Modern Optics* 2nd ed. (Holt, New York, 1975, Sec. 2.7.2-10).

⁹L. A. Segel, *Mathematics Applied to Continuum Mechanics* (Macmillan, New York, 1977) Appendix 9.1.

¹⁰See for example, ref. 8, Fig. 5.25.

¹¹D. C. Blanchard and L. D. Syzdek, "Production of air bubbles of a specified size," *Chem. Engng Sci.* **32**, 1109-1112 (1977).

¹²J. W. Goodman, *Introduction to Fourier Optics* (McGraw-Hill, San Francisco, 1968) Chap. 5.

¹³Ref. 12, Sec. 7.2.

¹⁴M. E. Mascart, *Traité D'Optique* Vol. I (Gauthier Villars et Fils, Paris, 1889), Sec. 195.

¹⁵The polarization dependence of this phenomenon was not determined in these observations.

¹⁶P. L. Marston and R. E. Apfel, "Acoustically forced shape oscillations of hydrocarbon drops levitated in water," *J. Colloid Interface Sci.* **68**, 280-286 (1979).

¹⁷P. L. Marston and R. E. Apfel, "Quadrupole resonance of drops driven by modulated acoustic radiation pressure: experimental properties," (unpublished).

¹⁸H. M. Nussenzveig, "High frequency scattering by a transparent sphere," *J. Math. Phys.* **10**, 82-124 (1969).

¹⁹D. Ludwig, "Diffraction by a circular cavity," *J. Math. Phys.* **11**, 1617-1630 (1970).

Paper No. 3

Scattering by bubble in water near the critical angle: interference effects (P. L. Marston and D. L. Kingsbury) J. Opt. Soc. Am. 71, 192-196 (1981) [An Erratum, reproduced below, was published in J. Opt. Soc. Am. 71, 917 (1981). This notes errors of transcription which are not corrected in the reprint given here.]

errata

In the caption to Fig. 3 of our paper,¹ $\eta = \phi - \phi_c$ should be written $\eta = \phi_c - \phi$, which is the definition of η given in the text of our paper. In the line below Eq. (15), $\beta_1 = (8/na)^{1/2} \cos \theta_c$ should be written as $\beta_1 = (8/na)^{1/2} / \cos \theta_c$. Also, the top line of the right-hand column on page 194 should be written as "... error from using Eq. (22) ..."

REFERENCE

1. P. L. Marston and D. W. Kingsbury, "Scattering by a bubble in water near the critical angle: interference effects," J. Opt. Soc. Am. 71, 192-196 (1981).

Scattering by a bubble in water near the critical angle: interference effects

Philip L. Marston

Department of Physics, Washington State University, Pullman, Washington 99164

Dwight L. Kingsbury

Department of Electrical Engineering, Washington State University, Pullman, Washington 99164

Received August 28, 1980

A physical-optics approximation is derived for light scattering by dielectric spheres with refractive indices less than their surroundings, and it is applied to air bubbles in water. The approximation gives the coarse structure in the scattering when the scattering angle ϕ is near the critical scattering angle ϕ_c , where $\phi_c \sim 83^\circ$ for bubbles in water. Diffraction has been observed to be important in the critical region because of an abrupt change in the amplitude of the reflected wave [P. L. Marston, J. Opt. Soc. Am. 69, 1205-1211 (1980)]. Interference that is due to a refracted wave produces oscillations in the intensity with an angular quasi-period of magnitude $(\lambda/a)^{1/2}$ rad near ϕ_c , where λ is the wavelength and a is the radius. Unlike diffraction related oscillations, the interference oscillations increase in magnitude as forward scattering is approached. Optical tunneling through bubbles is also discussed.

INTRODUCTION

An approximate description of the scattering of light by large dielectric spheres may be obtained from ray optics, provided that the observation angle is not in a region in which wave-front diffraction is dominant.¹ In the ordinary case, in which the refractive index of the sphere exceeds that of the surroundings, forward scattering, the rainbow, and the glory are the regions in which diffraction is important.¹⁻³ In the less-explored case of a sphere whose refractive index is less than the surroundings, a new region appears in which diffraction is important.⁴ This region may be called the *critical scattering region* because it is associated with light reflected from the sphere's surface when its angle of incidence is close to the critical angle normally associated with total reflection from plane surfaces. Diffraction effects in this region have been observed and described with a physical-optics approximation.⁴ The purpose of this paper is to discuss the effect of the interference of the reflected wave with certain rays that penetrate the sphere and are refracted to angles in the vicinity of the critical scattering region. This interference leads to a modification of the previous model⁴ that becomes significant in the critical region when an air bubble in water has a radius ≤ 0.4 mm.

Let the scattering angle ϕ denote the angle of the distant observation point measured with respect to the direction of propagation of the incident plane wave and the sphere's center. The critical scattering angle is $\phi_c = \pi - 2\theta_c$, where $\theta_c = \arcsin(n_i/n_o)$ is the critical angle of incidence and $n = (n_o/n_i) > 1$, n_o and n_i being, respectively, the refractive indices of the outer and the inner media. Air bubbles in water have $n \sim 4/3$ and $\phi_c \approx 82.82^\circ$. Figure 1 illustrates several rays that have a deviation angle ϕ of 50° . Each ray is characterized by a parameter p , where $p - 1$ is the number of reflections from the internal surface and $p = 0$ has only an external reflection. Rays that enter the bubble below the center line are

indicated with a prime. The angle of incidence measured from the surface normal is θ_p , and the corresponding refracted angle is ρ_p . Rays with $p \neq 0$ have $\theta_p < \theta_c$.

The previous physical-optics approximation⁴ described the diffraction of the virtual wave front associated with the $p = 0$ ray only. It was shown that diffraction is important in the region $|\phi - \phi_c| \sim (\lambda/a)^{1/2}$ rads, where a is the sphere radius and λ is the wavelength in the outer media; consequently, diffraction is important near ϕ_c even if λ/a is quite small. The present paper shows that the interference that is due to the $p = 1$ ray leads to a modulation of the scattered intensity as

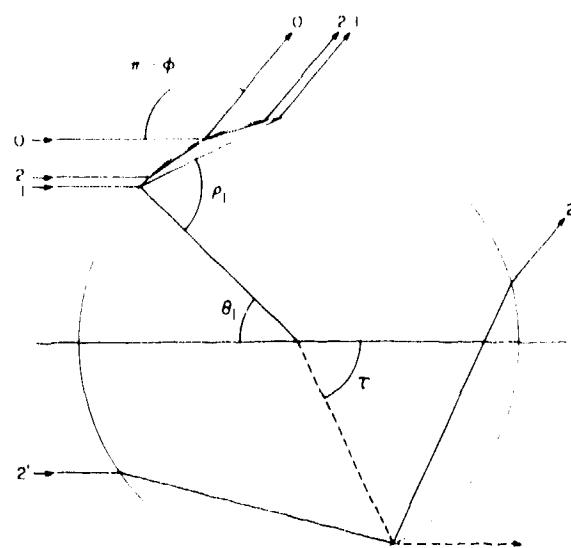


Fig. 1. Ray paths in the scattering plane with a scattering angle $\phi = 50^\circ$. The number gives the ray parameter p . The dashed ray is forward scattering that is due to tunneling from the reflected ray and is discussed in Sec. 4.

Reprinted from *Journal of the Optical Society of America*,

Vol. 71, page 192, February, 1981

Copyright © 1981 by the Optical Society of America and reprinted by permission of the copyright owner

a function of ϕ . The $p \geq 2$ rays will be omitted since they lead to virtual wave fronts much smaller in amplitude than the $p = 0$ and $p = 1$ wave fronts. The $p = 2'$ ray leads to a superposed low-amplitude modulation of the scattered intensity with an angular period $\approx \Lambda(\lambda/a)$, where a/Λ is the lateral separation of rays 0 and $2'$ after emergence from the sphere. For an air bubble in water, ray tracing gives $\Lambda \approx 0.82$ with $\phi = \phi_c$, whereas observations close to ϕ_c (Sec. V of Ref. 4) gave $\Lambda = 0.76 \pm 0.04$. The angular period of this modulation is $\ll (\lambda/a)^{1/2}$ when $a \gg \lambda$. The emphasis of the present paper is on the coarse structure in the scattering; consequently, primed rays are omitted. Mie-theory results⁵ (to be published separately) substantiate these approximations in the region $(\phi_c - 40^\circ) < \phi < \phi_c$ for $n = 4/3$.

1. DESCRIPTION OF THE VIRTUAL WAVE FRONTS

Diffraction and interference effects in the scattering are modeled by first using ray optics to describe virtual wave fronts positioned within the scatterer. These wave fronts are then allowed to diffract to the far field. Fortunately, it is not necessary to express the exact amplitude and phase of the wave fronts in terms of Cartesian coordinates. This is because approximate dependences, derived below, justify the use of the stationary-phase approximation in the diffraction integrals.

Figure 2 illustrates Cartesian coordinates used in the description of virtual wave fronts in the scattering plane. The origin is chosen to be the point where the reflected ray with $\theta_0 = \theta_c$ contacts the sphere. The positive v axis is the path of the scattered critical ray predicted by ray optics. The positions of the virtual wave fronts associated with rays 0 and 1 are denoted by the functions $v_0(u)$ and $v_1(u)$, where the u axis is perpendicular to the v axis and lies in the scattering plane. Phase shifts of ray 0 that are due to reflection beyond the critical angle are not included in v_0 but are accounted for with a separate phase factor in the description of the amplitude. The reference phase is selected such that $v_0(0) = 0$. Ray tracing gives $v_0 = v_1$ at $u = 0$, and the leading term in a Taylor series for v_0 is¹

$$v_0 = \alpha u^2, \quad (1)$$

where $\alpha = -(a \cos \theta_c)^{-1}$. The Taylor series for v_1 may be obtained by including effects of refraction and the change in velocity within the sphere; the leading term is

$$v_1 = \frac{1}{2} \alpha u^2, \quad (2)$$

The resulting wave fronts are shown in Fig. 2. The calculation of the interference of waves 0 and 1 uses the exact path-length difference that is not easily expressed as a function of u . Effects of wave-front curvature orthogonal to the scattering plane will be approximated with normalization factors to be introduced subsequently.

In the description of the scattering, it is only necessary to consider two cases with orthogonal incident polarizations, since the general case may be obtained by a linear combination.¹ The subscript j is assigned the value 1 when the incident electric vector is entirely perpendicular to the scattering plane and the value 2 when entirely parallel. Waves scattered to the far field associated with $p = 0$ and $p = 1$ rays may be simulated by a wave on the u axis with the following amplitude:

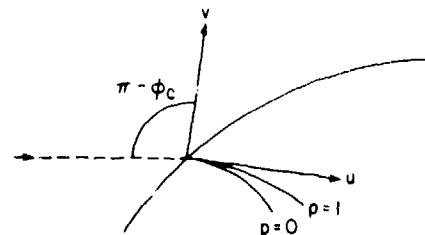


Fig. 2. Positions of the virtual wave fronts for $p = 0$ and $p = 1$ scattering. The dashed ray is the incident critical ray that is reflected to become the v axis. A portion of the bubble's surface is also shown.

$$U_{p,j}(u,t) = h_{p,j} \exp[i(-kv_p - \omega t)], \quad (3)$$

where $i = \sqrt{-1}$, ω is the frequency, t is the time, and $k = 2\pi/\lambda$. The $\exp(-i\omega t)$ factor will be omitted subsequently. Ray tracing and the physical-optics approximation give the following amplitude factors^{1,4}:

$$h_{0,j} = r_j(\theta_0), \quad u < 0, \quad (4)$$

$$h_{0,j} = e^{-i\delta_j}, \quad u > 0, \quad (5)$$

$$h_{1,j} = 0, \quad u < 0, \quad (6)$$

$$h_{1,j} = [1 - r_j(\theta_1)^2] \sqrt{\kappa D}, \quad u > 0, \quad (7)$$

where the r_j are Fresnel's amplitude reflection coefficients for a plane surface,⁶

$$r_1(\theta_p) = \frac{\sin(\rho_p - \theta_p)}{\sin(\rho_p + \theta_p)}, \quad (8)$$

$$r_2(\theta_p) = \frac{\tan(\theta_p - \rho_p)}{\tan(\rho_p + \theta_p)}, \quad (9)$$

and ρ_p is the refraction angle predicted by Snell's law,

$$\rho_p = \arcsin(n \sin \theta_p). \quad (10)$$

The Stokes symmetry relations have been used in the derivation of Eq. (7), where D is Van de Hulst's divergence factor,¹ which may be written⁷

$$D = \frac{\sin \theta_1 \cos \theta_1}{2[1 - (n \cos \theta_1 / \cos \rho_1)] \sin \phi}, \quad (11)$$

ϕ is the scattering angle of the $p = 1$ ray predicted by ray optics,

$$\phi = 2(\rho_1 - \theta_1), \quad (12)$$

and κ is a positive constant normalization factor determined subsequently.

The phase shifts⁸ δ_j are associated with the (nearly) total reflection of ray 0 as θ_0 exceeds θ_c (tunneling through large bubbles can be neglected; see Sec. 4):

$$\tan(\delta_1/2) = (\sin^2 \theta_0 - n^{-2})^{1/2} / \cos \theta_0, \quad (13)$$

$$\tan(\delta_2/2) = n^2 \tan(\delta_1/2). \quad (14)$$

The δ_j vanish when $\theta_0 = \theta_c$, but they become positive as θ_0 exceeds θ_c , which represents an *advancement* of the $p = 0$ virtual wave front. (The reader is cautioned that some authors write δ_1 and δ_2 with an incorrect sign for their choice of the sign of ω in the time-dependence factor.⁹)

Approximate dependence of $h_{p,j}$ on small values of u is obtained by first relating θ_p to u for $u \sim 0$ and $\theta_p \sim \theta_c$. This

leads to the following proportionalities: $1 - h_{0,j} \propto (-u/a)^{1/2}$ for $u < 0$, $h_{1,j} \propto (u/a)^{3/2}$ for $u > 0$, and⁴

$$\delta_j \approx \beta_j u^{1/2}, \quad (15)$$

where $\beta_1 = (8/na)^{1/2} \cos \theta_c$ and $\beta_2 = n^2 \beta_1$.

2. FAR-FIELD DIFFRACTION AND INTERFERENCE OF THE SCATTERED WAVES

Let R denote the distance to the observation point from the center of the bubble. When $R \gg k\alpha^2$, the scattering amplitude is proportional to the Fourier transform of $U_{0,j} + U_{1,j}$, which may be written as $f_j = f_{0,j} + f_{1,j}$, where

$$f_{p,j}(\sin \eta) = \int_{-\infty}^{\infty} U_{p,j}(u) \exp(-iku \sin \eta) du \quad (16)$$

and $\eta \equiv \phi_c - \phi$. An approximation for $f_{0,j}$ with $\eta > 0$, which was introduced in Ref. 4, is to let $U_{0,j} = 0$ for $u < 0$ because $U_{0,j}$ decreases abruptly as u becomes negative. It is not clear if ray optics can be used to model the virtual wave in the region in which $|\partial h_{0,j}/\partial u|$ is large; however, its use leads to the diffraction of reflected energy away from the critical region and supports the approximation $U_{0,j}(u < 0) = 0$. Most of the diffracted $p = 0$ wave in the critical region comes from the virtual wave, where u is small and positive, and an approximate result is obtained by using Eqs. (1) and (15) in the entire positive u domain. The integral may be approximated by using the principle of stationary phase¹⁰ with the result that $f_{0,j} = (\lambda a \cos \theta_c)^{1/2} g_{0,j}/2$, where^{4,11}

$$g_{0,j} \approx \exp(i\gamma_{0,j}) [F(w) - F(-\infty)], \quad (17)$$

$$w = [(a/\lambda) \cos \theta_c]^{1/2} \sin \eta, \quad (18)$$

$$\gamma_{0,j} = -\beta_j (w/2)^{1/2} (\lambda a \cos \theta_c)^{1/4} + \frac{k(\sin \eta)^2}{4\alpha}, \quad (19)$$

where the first term of Eq. (19) is the phase shift of the geometric ray reflected to ϕ and $F(w)$ is Fresnel's integral,

$$F(w) = \int_0^w \exp[i(\pi/2)z^2] dz. \quad (20)$$

When the observation point is in the critical region, Eq. (2) may be used in the evaluation of $f_{1,j}$:

$$f_{1,j} = \int_0^{\infty} h_{1,j} \exp[-i\{ku \sin \eta + (k\alpha u^2/2)\}] du. \quad (21)$$

The phase of the complex exponential is stationary when $u = \bar{u}$, where $\bar{u} = a \cos \theta_c \sin \eta$. Since $h_{1,j}$ is a slowly varying function of u , the stationary-phase approximation may be used to evaluate Eq. (21) provided that \bar{u} is well within the domain of integration.¹⁰ The result is $f_{1,j} = (\lambda a \cos \theta_c)^{1/2} g_{1,j}/2$, where

$$g_{1,j} = 2h_{1,j}(\theta_1) \exp\left[i\left(\frac{\pi}{4} + \gamma_{1,j}\right)\right] + O(\lambda/a)^{1/2}, \quad (22)$$

$$\gamma_{1,j} = \frac{k(\sin \eta)^2}{2\alpha}. \quad (23)$$

In Eq. (22) the stationary-phase point that is used in the evaluation of $h_{1,j}$ corresponds to the θ_1 given by Eqs. (10) and (12). The use of the stationary-phase approximation breaks down as $\eta \rightarrow 0$, since $\bar{u} \rightarrow 0$; however, this is just where $h_{1,j} \rightarrow 0$, and the scattering is dominated by the diffracted $p = 0$

wave. Consequently, the error from using Eq. (23) in the total scattering should be acceptable even if η is small.

The scattered intensity normalized to that of the geometric result for a perfectly reflecting sphere of the same size is

$$I_j = 1/2 |g_{0,j} + g_{1,j}|^2, \quad (24)$$

where the normalization was obtained by noting that $|g_{0,j}| \rightarrow \sqrt{2}$ as $w \rightarrow \infty$. The actual intensity is the incident intensity multiplied by $I_j(a/R)^2/4$. The value of κ in Eq. (7) is determined to be 2 by noting that only then does $g_{1,j}$ become the value predicted by ray optics.⁷ Because of the interference of the $g_{p,j}$, the intensity is sensitive to the computation of $(\gamma_{0,j} - \gamma_{1,j})$. Comparisons with Mie theory have shown that the phase difference given by Eqs. (19) and (23) is limited in its usefulness because of errors introduced by Eqs. (1), (2), and (15). The agreement with Mie theory is significantly improved when $(\gamma_{0,j} - \gamma_{1,j})$ is taken to be the exact value predicted by ray optics^{1,7}:

$$\gamma_{0,j} - \gamma_{1,j} = 2ka(\cos \theta_1 - \cos \theta_0 - n^{-1} \cos \rho_1) - \delta_j(\theta_0), \quad (25)$$

where θ_0 is predicted by ray optics to be

$$\theta_0 = (\pi - \phi)/2 \approx \theta_c + (\eta/2). \quad (26)$$

To evaluate Eqs. (22) and (25) for a given value of ϕ , it is necessary to solve the transcendental Eqs. (10) and (12) for θ_1 and ρ_1 . The evaluation of Eq. (24) requires the evaluation of Eqs. (7)–(14), (17), (18), (22), (25), and (26).

3. DISCUSSION

Figures 3–6 illustrate the result of three approximations for the scattered intensity for an air bubble in water normalized to the ray-optics value for a perfectly reflecting sphere. In each figure, $n = 4/3$. The ray-optics result for a bubble is equal to $1 + 2h_{1,j}^2$ when $\eta \geq 0$ and $r_j(\theta_0)^2$ when $\eta < 0$. It exhibits a cusp at the critical angle, which is also evident in the ray-optics predictions plotted by Davis⁷ and by Welford.¹² The predictions for the diffraction-only model developed in Ref. 4 are given by $|g_{0,j}|^2/2$. The present model must eventually break down in the region where $\eta < 0$ because of the

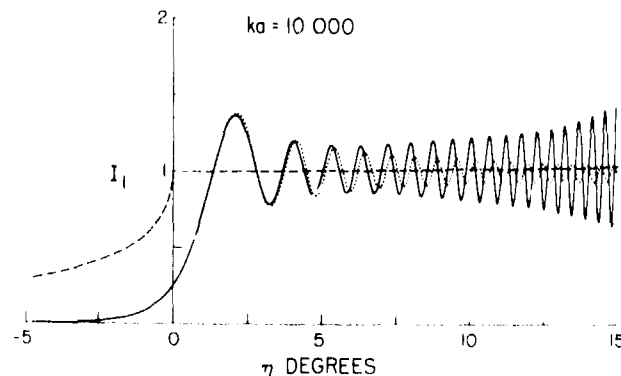


Fig. 3. Three approximations for scattered intensity as a function of $\eta = \phi - \phi_c$ with $n = 4/3$, the electric field perpendicular to the scattering plane, and $ka = 10,000$. The dashed curve is the result of ray optics, which adds the intensities of $p = 0$ and $p = 1$ scattering. The dotted curve is the diffracted $p = 0$ wave only and is from Eq. (17). The solid curve is given by Eq. (24), which includes the diffraction of the $p = 0$ wave and the interference of the $p = 1$ wave.

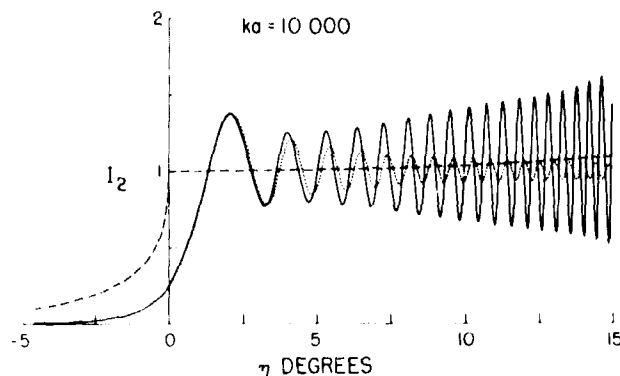


Fig. 4. Same as Fig. 3 but with parallel polarization.

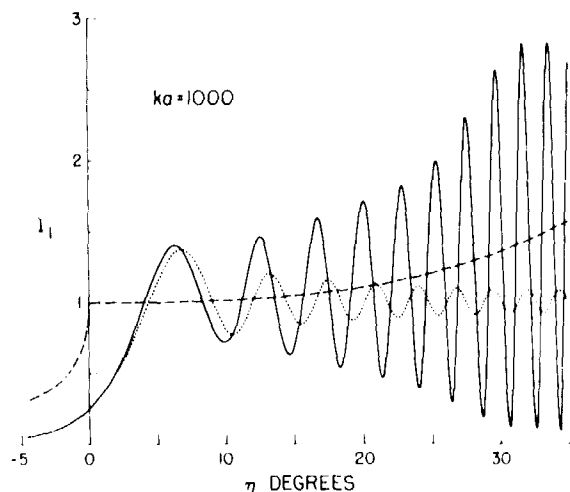
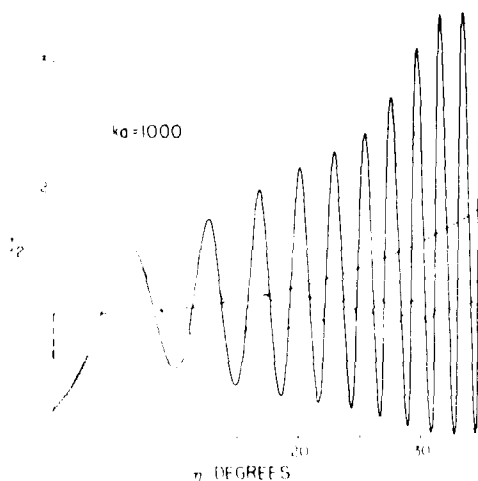
Fig. 5. Same as Fig. 3 but with $ka = 1000$.

Fig. 6. Same as Fig. 5 but with parallel polarization.

assumption that $U_{0,j}(u < 0) = 0$. In the figures, the model has been extended into that region by evaluating Eq. (24) with $g_{1,j}(\eta < 0) = 0$. Fresnel's integral $F(u)$ was evaluated with a numerical approximation.¹³

The bubble sizes in these figures are manifest by considering illumination by a He-Ne laser with a wavelength in air

of 632.8 nm and a wavelength in water $\lambda \sim 474.6$ nm. Then $ka = 10,000$ gives $a = 0.755$ mm. When measuring the scattering, refraction corrections may be required to relate the scattering angle in the water to that seen by an external instrument.⁴

The diffraction-only theory⁴ predicted oscillations in the intensity that are homologous with respect to bubble size, polarization, and refractive index. They decrease monotonically in magnitude as η increases and have an angular quasi-period $\leq (\lambda/a)^{1/2}$ rad. Figure 3 shows that, for $j = 1$ and $ka = 10,000$, interference alters the scattering significantly for $\eta \geq 10^\circ$. After the fourth maximum, the oscillations increase in magnitude. It is noteworthy that the quasi-period of the newly predicted oscillation is also roughly $(\lambda/a)^{1/2}$ rad [as may be shown by Eqs. (1) and (2)]. Figures 4-6 show that the effect of interference is even larger for $j = 2$ and for $ka = 1000$. The intensity averaged over a quasi-period is roughly the ray-optics result. Consequently, for large spherical bubbles in white light, the ray-optics results are useful *except* when $w \leq 2.5$, where diffraction corrections become essential ($w = 2.5$ corresponds to $\eta = 4.4^\circ$ at $ka = 10,000$ and $\eta = 14.0^\circ$ at $ka = 1000$.)

The experimental data plotted in Ref. 4 were for $ka \approx 10,930$ and $j = 2$. A comparison of Fig. 4 with those data indicates that it is not surprising that the diffraction-only model correctly described the relative positions of the first four maxima but that it underestimated the magnitude of the intensity oscillations for $\eta > 3^\circ$. A new apparatus has been built that permits observations in the region $\eta > 7^\circ$, which was obscured in the original⁴ apparatus. Visual observations for air bubbles with $a \approx 1$ mm in monochromatic light suggest that the magnitude of the intensity oscillations tends to increase with increasing η but, as of the time of this writing, photographs of a quality to permit quantitative measurements have not been obtained. These observations preceded and motivated the present theoretical effort.

The intensities given by Eq. (24) have been compared with Mie theory^{1,14} with $n = 4/3$ and $ka = 25, 100, 1000, 5000$, and $10,000$. The computations were performed using Wiscombe's Mie-scattering algorithms¹⁵ with minor modifications. The comparison shows⁵ that, for $0 < \eta < 30^\circ$, the coarse structure is approximately described by Eq. (24). Errors in the predicted locations of intensity oscillations are typically less than one tenth of a quasi-period. Furthermore, the phase difference of the scattering amplitudes for the two polarizations given by Eq. (28) (below) reproduces the coarse structure in the Mie results. Equation (24) differs most from the coarse structure in the Mie results when $j = 2$. This may be due in part to its omission of the $p = 2$ wave, which has a smaller amplitude for $j = 1$ than for $j = 2$. For example, at $\eta = 30^\circ$, the intensities of $p = 2$ scattering in the units of Figs. 3-6, are given by ray optics⁷ to be 0.012 and 0.015, respectively.

Equation (24) does not describe *fine structure* in the Mie intensities which is most prominent when $j = 1$. This structure has a quasi-period $\sim \lambda(\lambda/a)$ rad (0.3° for $ka = 1000$), which indicates that it could be included in the model with the addition of $p = 2'$ scattering. Ray optics verifies that the amplitude of $2'$ scattering in the critical region is largest when $j = 1$. Except for the fine structure, the Mie intensities decrease gradually as η decreases through zero. The error in Eq. (24), with η negative, generally decreases with ka as diffraction becomes more important.⁵

Equation (24) may be converted to the units commonly used in Mie algorithms through the following transformation:

$$|S_j|^2 = (ka)^2 I_j/4, \quad (27)$$

where S_j are the scattering amplitudes in the usual units.^{1,15,16} The phase difference of S_1 and S_2 is needed if the scattering for arbitrary states of the incident polarization is to be calculated.^{1,16} The phase difference is predicted to be¹⁷

$$\arg(S_2) - \arg(S_1) = \arg(g_{0,2} + g_{1,2}) - \arg(g_{0,1} + g_{1,1}), \quad (28)$$

where \arg denotes the complex argument of the quantity indicated. The present calculation uses an $\exp(-i\omega t)$ time factor, whereas the S_j are often,^{1,15} but not always,¹⁶ specified by using $\exp(+i\omega t)$, so the right-hand side of Eq. (28) should be multiplied by -1 for some applications.

The coarse structure in the scattering, which arises because of the interference of the reflected and refracted light, may be a useful experimental tool. The angular position of the maxima should shift if there are changes in the size of a bubble or, for the case of a drop with $n_i < n_o$, if the refractive-index ratio changes. Shifts in the structure of rainbow scattering have been useful for detecting shape oscillations in drops,¹⁸ and a similar technique could be used for detecting small changes in the scattering from bubbles.

Diffraction associated with the critical angle and structured scattering that is due to interference should also be present in the scattering by cylindrical bubbles or dielectric cylinders with $n_i < n_o$. For a circular cylinder with a symmetry axis perpendicular to the incident beam, the critical scattering angle and ray tracing in the scattering plane are the same as those described here for spheres. The divergence factors used in the description of the virtual wave fronts differ from those of a sphere. The geometric optics of a large, perfectly reflecting cylinder¹⁹ show that (neglecting tunneling) $|h_{0,j}(u > 0)|$ is no longer constant but is $\propto [\sin(\phi/2)]^{1/2}$. The normalized magnitude and positions of the intensity oscillations should differ from those of a sphere. Critical-angle diffraction and interference structure should also be present in acoustic scattering from fluid spheres and cylinders.²⁰

4. ELECTROMAGNETIC TUNNELING THROUGH SPHERICAL BUBBLES

The present model has assumed that the reflection is total when $\theta_0 > \theta_c$. The existence of evanescent waves within the bubble will, however, frustrate the total reflection, as in the case of plane dielectric slabs separated by an air gap.²¹ The effect of tunneling on nearly total reflection at curved dielectric interfaces has been studied to determine losses from curved optical waveguides²²; however, the sense of the curvature differs from that in the present case. The effect of tunneling through bubbles can be estimated by using the plane slab results,²¹ in which the gap d is equal to the bubble diameter and θ_0 becomes the angle of incidence at the plane surface. The result of this approximation is that the wave that has tunneled through the bubble will always be transmitted in the forward direction. The dashed ray in Fig. 1 shows the ray transmitted because of the frustrated reflection of the $p = 0$ ray. For each $p = 0$ ray with $\theta_0 > \theta_c$, there is a forward-transmitted ray with $\tau = \theta_0$. The intensity transmittance through a plane gap is found to be of order $(kd)^{-1}$

when $\theta_0 = \theta_c$, and it decreases rapidly as θ_0 exceeds θ_c . Tunneling should have a negligible effect on the reflection from a bubble unless ka is small. This conclusion is also supported by the success of the present model in reproducing Mie results⁵ when $ka = 25$.

We are grateful to R. G. Olsen for his comments on tunneling. Acknowledgement is made to the following organizations for partial support of this research: the donors of the Petroleum Research Fund, administered by the American Chemical Society; the Washington State University Research and Arts Committee; and the U.S. Office of Naval Research.

REFERENCES

1. H. C. van de Hulst, *Light Scattering by Small Particles* (Wiley, New York, 1957).
2. H. M. Nussenzveig, "Complex angular momentum theory of the rainbow and the glory," *J. Opt. Soc. Am.* **69**, 1068-1079 (1979).
3. G. P. Konnen and J. H. de Boer, "Polarized rainbow," *Appl. Opt.* **18**, 1961-1965 (1979).
4. P. L. Marston, "Critical angle scattering by a bubble: physical-optics approximation and observations," *J. Opt. Soc. Am.* **69**, 1205-1211 (1979); **70**, 353(E) (1980).
5. D. L. Kingsbury and P. L. Marston, "Mie scattering near the critical angle of bubbles in water," *J. Opt. Soc. Am.*, to be published (March 1980).
6. Unlike in Ref. 4, $h_{0,2}$ and r_2 are written here without minus signs in front of their right-hand sides because this convention gives a description of the interference that is convenient for comparison with Mie theory.
7. G. E. Davis, "Scattering of light by an air bubble in water," *J. Opt. Soc. Am.* **45**, 572-581 (1955).
8. H. K. V. Lotsch, "Reflection and refraction of a beam of light at a plane interface," *J. Opt. Soc. Am.* **58**, 551-561 (1968).
9. Ref. 8, footnote 62.
10. L. A. Segel, *Mathematics Applied to Continuum Mechanics* (Macmillan, New York, 1977), Appendix 9.1.
11. Equations (18) and (19) differ from Ref. 4 because it is not assumed in these equations that $\sin \eta \sim \eta$.
12. W. T. Welford, "Illumination and photography of bubble chambers," in *Bubble and Spark Chambers*, R. P. Shutt, ed. (Academic, New York, 1967), Vol. 1, pp. 233-313.
13. M. Abramowitz and I. A. Stegun, *Handbook of Mathematical Functions* (Dover, New York, 1965), pp. 301-302, Eqs. 7.3.32, 7.3.33, 7.3.9, 7.3.10.
14. G. Mie, "Beiträge zur Optik trüber Medien, speziell kolloidaler Metallösungen," *Ann. Phys. (Leipzig)* **25**, 377-445 (1908).
15. W. J. Wiscombe, "Improved Mie scattering algorithms," *Appl. Opt.* **19**, 1505-1509 (1980).
16. A. Ishimaru, *Wave Propagation and Scattering in Random Media* (Academic, New York, 1978), Vol. 1, pp. 27-35.
17. The absolute phases of S_1 and S_2 are not calculated here because the coordinate system used in Sec. 1 was not centered on the bubble and because wave front curvature orthogonal to the scattering plane introduces an undetermined phase factor independent of the polarization. Equation (25) is to be used in the evaluation of Eq. (28).
18. P. L. Marston, "Rainbow phenomena and the detection of non-sphericity in drops," *Appl. Opt.* **19**, 680-685 (1980).
19. J. B. Keller, R. M. Lewis, and B. D. Seckler, "Asymptotic solution of some diffraction problems," *Commun. Pure Appl. Math.* **9**, 207-265 (1956), example 19.
20. P. L. Marston, "Critical angle diffraction in high frequency scattering by fluid spheres and cylinders," *J. Acoust. Soc. Am.* **66**, S80(A) (1979); **67**, 718(E) (1980).
21. L. N. Court and E. K. von Willisen, "Frustrated total internal reflection and applications of its principle to laser cavity design," *Appl. Opt.* **3**, 719-726 (1964).
22. A. W. Snyder and J. D. Love, "Reflection at a curved dielectric interface—electromagnetic tunneling," *IEEE Trans. Microwave Theory Tech.* **MTT-23**, 134-141 (1975).

Paper No. 4

Mie scattering near the critical angle of bubbles in water (D. L. Kingsbury and P. L. Marston) J. Opt. Soc. Am. 71, 358-361 (1981) [A supplemental with unpublished Mie computations is included here.]

Mie scattering near the critical angle of bubbles in water

Dwight L. Kingsbury

Department of Electrical Engineering, Washington State University, Pullman, Washington 99164

Philip L. Marston*

Department of Physics, Washington State University, Pullman, Washington 99164

Received September 11, 1980

Mie-scattering algorithms were used to compute scattered intensities and phase differences for air bubbles in water. Results are plotted as a function of the scattering angle ϕ in the general range of 30° – 90° for size parameters ka of 25, 100, 1,000, and 10,000 (corresponding to radii $a \sim 1.3 \mu\text{m}$ to 0.8 mm). As ϕ decreases below the critical scattering angle at 82.8° , the intensity increases and undergoes broadly spaced oscillations that are described by a physical-optics approximation developed by the authors in a separate publication. Mie scattering also exhibits finely spaced oscillations.

INTRODUCTION

Observations of light scattered by air bubbles in water in the vicinity of the critical scattering angle¹ indicate that diffraction is significant, even if the bubble radius a is as large as 1 mm. The coarse structure in the critical scattering region has been described with a physical-optics approximation that accounts for the diffraction of light reflected from the bubble's surface and the interference of certain refracted light.² In this Letter we use Mie theory^{3–5} to calculate far-field scattered intensities and phase differences in the critical region of spherical bubbles in water and compare these exact results with those of the physical-optics approximation.² Previous applications of Mie theory to bubbles emphasized the calculation of the scattering efficiency factor^{6–8} and the radiation pressure.⁸ In contrast with the scattering by spherical drops,^{4,9,10} the exact angular structure in the scattering by bubbles is not well explored.

Consideration of the approximate scattering⁷ introduces the features to be expected in the exact Mie results and facilitates the choice of the range and frequency of the angles needed for a description of the angular structure. Figure 1 illustrates several rays with a scattering angle ϕ of 50° . In this figure and the Mie computations that follow, the relative refractive index n_i/n_o is taken to be $3/4$, where n_o is the refractive index of the water and n_i is the refractive index of the bubble contents. Rays are characterized by a parameter p , where $p = 1$ is the number of reflections within the bubble and $p = 0$ has only an external reflection; θ_p is the angle of incidence at the p th ray when it first touches the surface of the bubble. When $\sin \theta > n_i/n_o$, the $p = 0$ ray is totally reflected (the effects of tunneling¹¹ and surface curvature are neglected). The corresponding condition on the scattering angle of the reflected ray is $\phi < \phi_c \sim 82.82^\circ$, where ϕ_c , the critical scattering angle, is related to n_i/n_o through Eqs. (1) and (2) of Ref. 1. (For air bubbles in seawater, ϕ_c may be as large as 84° .) The physical-optics approximations^{1,2} lead to the predictions of structure in the angular scattering with an angular spread

of the order of $(\lambda/a)^{1/2} \text{ rad}$ [$\sim 144(ka)^{-1/2} \text{ deg}$], where λ is the wavelength in the outer medium and $k = 2\pi/\lambda$. Structure with a quasi-period of that magnitude will be referred to as *coarse structure*, in contrast to *fine structure* in the scattering that has a quasi-period in the critical region of *less than* $\lambda/a \text{ rad}$ (or $360^\circ/ka$). The fine structure originates in part from the interference of the $p = 2$ ray with the rest of the scattering. To describe the general effects of the critical angle on the scattering, Mie computations are needed with a spread of $|\phi_c - \phi|$ somewhat larger than $(\lambda/a)^{1/2}$ with angular steps somewhat smaller than $\lambda/2a$ to prevent sampling errors.

COMPUTER-PROGRAM CONSIDERATIONS

The Mie solutions were computed by using the FORTRAN MIEVO subroutine developed by Wiscombe,^{12,13} chosen in

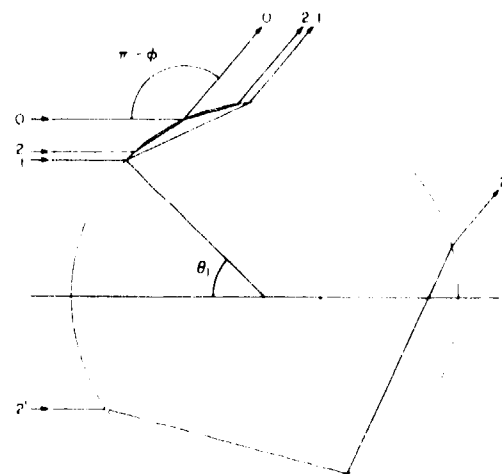


Fig. 1. Ray paths in the scattering plane with a scattering angle $\phi = 50^\circ$. The number adjacent to each ray gives the ray parameter p . The approximation given in Ref. 2 includes the interference and diffraction of waves associated with rays 0 and 1.

preference to his faster MIEV routine because of the memory limitations of the HP 1000 computer system used in the work. We found it necessary to convert all Wiscombe's internal variables to HP double precision (14 significant digits), and we were then able to duplicate his tables¹¹ for scattering by a drop with $n_i/n_o = 1.5$. (Wiscombe's subroutines assume 14-digit single precision.) Most complex arithmetic was rewritten as real arithmetic because of the absence of complex double precision. The logarithmic derivative of the Riccati-Bessel function, commonly denoted by A_n , was calculated by downward recursion, which is known to be stable. The program was tested against Wiscombe's tables for $n_i/n_o = 1.5$ of the complex scattering amplitudes and efficiency factors and against the scattering efficiency factors for small size parameters when $n_i/n_o = 0.75$ as given in Refs. 7 and 8.

Let N denote the number of terms included in the computation of the Mie series and N_{ang} denote the number of angles for which the Mie scattering is computed. Since MIEV0 uses^{6,11} $N = ka + 4.05(ka)^{1/3} + 2$ and N_{ang} must also be increased in proportion to ka to resolve the fine structure, execution time is roughly proportional to $(ka)^2$ for a fixed spread of angles. Whereas the results for $ka = 25$ required a fraction of a minute, those for $ka = 10,000$, where the angle step size was 0.005° , required 2.5 h for 8000 angles. (These times were realized after vectorization of two N_{ang} loops, which speeded up execution by a factor of approximately 4.)

Higher values of N than that given in Wiscombe's equation above were tested for the bubble case with $ka = 100$ and 1000 and found to yield identical results to six decimal places.

In contrast, the physical-optics approximation program was executed in seconds, regardless of size parameter. Equations used in that program are listed at the end of Section II of Ref. 2.

RESULTS

Calculated intensities I_j as a function of the scattering angle ϕ are shown in Figs. 2-4. The normalization was chosen so that $I_j(\phi) = 1$ represents perfect reflection according to geometric optics.^{2,12} At a distance $R \gg ka^2$ from the center of the sphere, the actual j -polarized intensity is the incident j -polarized intensity multiplied by $I_j(a/R)^2/4$, where $j = 1$ denotes polarization of the electric vector perpendicular to the scattering plane and $j = 2$ the parallel case. The van de Hulst normalization⁴ used in Wiscombe's routines required that the squared modulus of the scattering amplitude computed with MIEV0 be multiplied by $(2/ka)^2$ to be expressed in the units of Figs. 2-4.⁷

As is shown in the figures, the exact solution suggests that a fine ripple structure is superposed upon the coarse structure that is described by the physical-optics approximation. The ripples have a quasi-period of about $0.82 (\lambda/a)$ rad near ϕ_c , decreasing slightly with ϕ . To avoid severe distortion resulting from sampling errors, it was necessary to use an angle step size less than $\lambda/7a$ rad. This fine structure is due to the interference of rays not included in the approximation, primarily the $p = 2'$ ray. Consequently, the ripples should be damped out for bubbles containing a gas that absorbs light. Fine structure from air bubbles has been observed.¹

The plots in Fig. 5 show the phase difference of the scattered waves

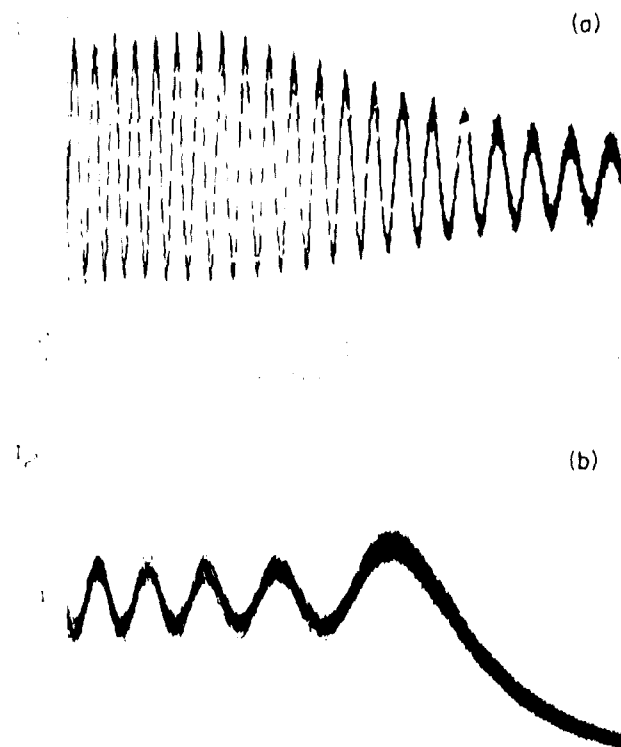


Fig. 2. Calculated normalized scattering intensities for $ka = 10,000$. The electric vector is parallel to the scattering plane. The solid curve is from Mie theory. The dashed curve is the physical optics approximation given in Ref. 2.

$$\delta = \arg(S_2) - \arg(S_1), \quad (1)$$

where the S_j are Mie scattering amplitudes for a time dependence of $\exp(-i\omega t)$, where ω is the frequency and t the time. This phase difference can be used along with I_1 and I_2 to compute the scattered intensity and polarization for arbitrary states of incident polarization.⁴ The physical-optics approximation for δ is given by Eq. (28) of Ref. 2. As is described in Ref. 2, it was necessary to reverse the sign of δ from the output of the MIEV0 program because Wiscombe assumes a time dependence of $\exp(+i\omega t)$.

DISCUSSION

For $\phi > \phi_c$, the agreement with the approximation is best at low size parameters where diffraction accounts for the scattering in this region in the approximation.

The coarse-structure oscillations at angles $\phi < \phi_c$ are similar to the predictions of diffraction theory, which gives a reflected intensity proportional to the squared modulus of Fresnel integrals [Eq. (30) of Ref. 1]. The first maximum of the reflected intensity occurs at¹

$$\phi_c - \phi \sim 1.2(\lambda/a \cos \theta_c)^{1/2} \text{ (rad)}. \quad (2)$$

The Cornu spiral behavior of the Fresnel integrals predicts a decrease in the amplitude of these intensity oscillations with decreasing ϕ and also a decrease in their quasi-period. The amplitude decrease is most evident at large size parameters

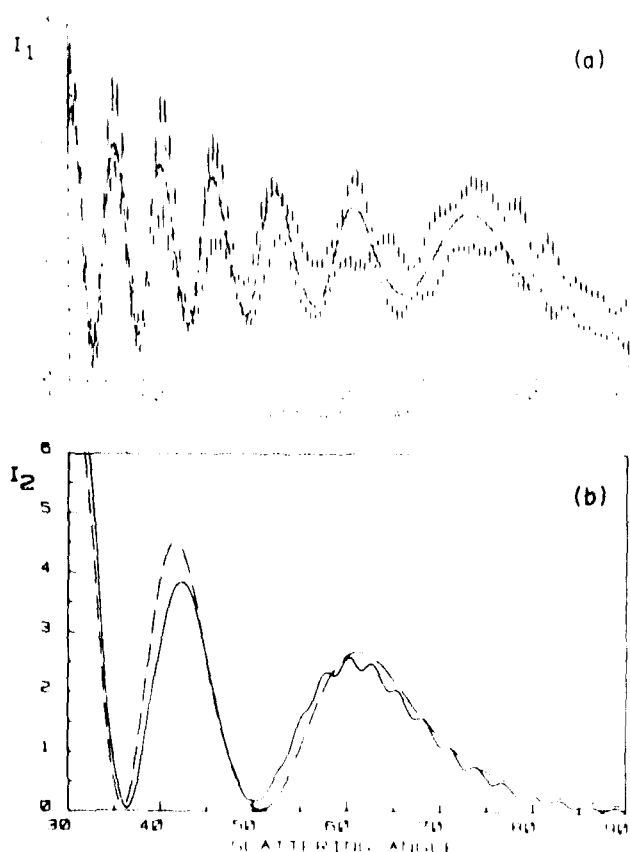


Fig. 3. Like Fig. 2 but with (a) $ka = 1000$ and the electric vector perpendicular to scattering plane and (b) $ka = 100$ and the electric vector parallel to the scattering plane.

(Fig. 2) where the diffraction pattern is less spread out; at small size parameters the diffraction decrease is lost because of the increasing amplitude of the intensity oscillations associated with the interference of the $p = 1$ ray. These oscillations are also of quasi-period $\lesssim (\lambda/a)^{1/2}$ rad,² diminishing with ϕ . In addition to the j polarizations of Figs. 2-4, the physical-optics approximation has been verified for the j not shown and for both j at $ka = 5000$. Both the approximation and the Mie theory predict that the positions of the coarse maxima depend only weakly on j ; the coarse maxima lie slightly closer to ϕ_c when $j = 1$. The approximation predicts that the intensity variations of the coarse-structure oscillations are greatest when $j = 2$, which agrees with Mie theory.

Mie theory shows that the *fine-structure* intensity variations are larger for $j = 1$ than for $j = 2$; this is probably because $p = 2'$ scattering is greatest when $j = 1$.² For $30^\circ \leq \phi \leq 90^\circ$, the positions of the fine-structure intensity oscillations for $j = 2$ are typically shifted from those for $j = 1$ by one half of a fine-structure quasi-period, except when ϕ is slightly less than ϕ_c .

It is evident from Fig. 5 that the coarse structure of the phase difference for Mie scattering roughly follows that of the physical-optics approximation. This has also been verified at $ka = 25$. The gently sloping curve of the approximate result near ϕ_c may be understood in terms of the phase advances δ_j of the (totally reflected) $p = 0$ ray; δ_2 is approximately $(n_0/n_1)^2 \delta_1$ near ϕ_c .^{1,2} Comparison of Figs. 5 and 3 shows that

the maxima in the coarse structure of $[\delta]$ are associated with minima in the coarse structure of the I_j . An anomaly is present in Fig. 5(b) for $\phi \sim 37^\circ$. Mie computations of I_1 indicate that I_1 is quite small at this anomaly; for $ka = 100$, I_1 has a minimum value of 8×10^{-4} in the units of Fig. 3(b) at $\phi = 36.705^\circ$. The plot of δ for $ka = 25$ reveals a similar anomaly at $\phi \sim 23^\circ$.

The range of bubble sizes associated with Figs. 2-5 will be illustrated by considering green illumination with a wavelength in air of 550 nm and a wavelength in water λ of 413 nm; then $ka = 10,000$ gives $a = 652 \mu\text{m}$ and $ka = 25$ gives $a = 1.6 \mu\text{m}$.

It is remarkable that the physical-optics approximation describes the general features of the broad intensity maxima at $\phi \sim 35^\circ$ for $ka = 25$. A stationary-phase approximation was used in Refs. 1 and 2 to eliminate a phase term $[\psi_j(\tau, w)]$ in Eq. (24) of Ref. 1 from the diffraction integral. The arguments given in Ref. 1 that justify that approximation would appear to break down for $ka = 25$. The rough success of the model indicates that the maximum can be attributed in part to the first diffraction maximum and in part to the interference of the refracted wave associated with the $p = 1$ ray; however, 25 may be close to the lowest value of ka for which this model is useful.

The principal purpose for developing and testing the physical-optics approximation² was to see if the coarse structure in the scattering could be related to the diffraction and interference of reflected and refracted waves. The model

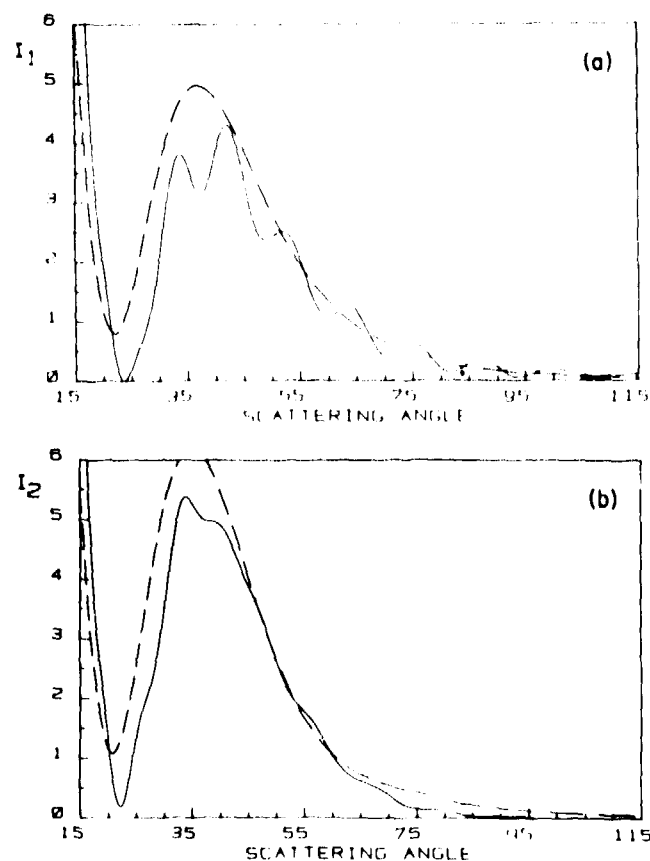


Fig. 4. Like Fig. 2 but with $ka = 25$ and the electric vector (a) perpendicular and (b) parallel.

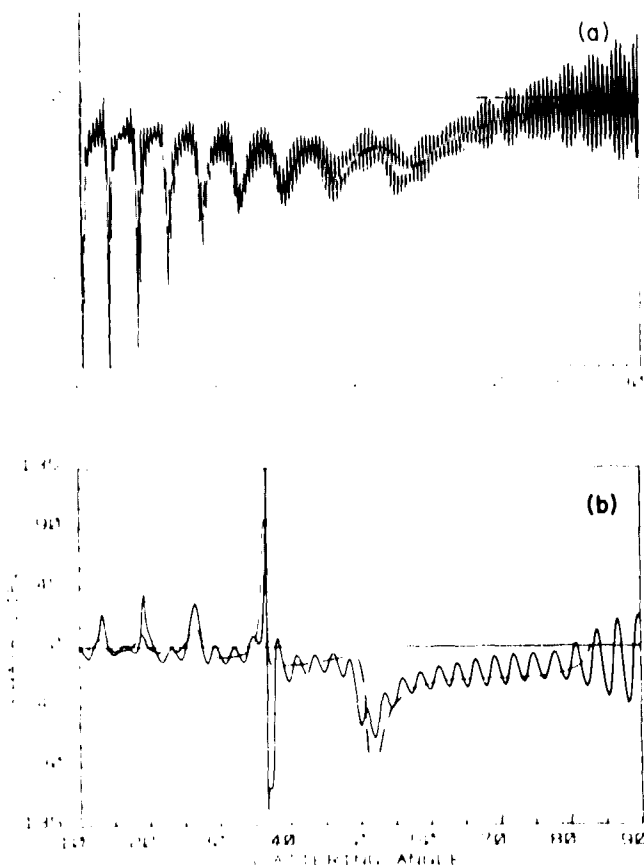


Fig. 5. Phase difference for the scattering amplitudes in the two polarization states for (a) $ka = 1000$ and (b) $ka = 100$. The solid curve is from Mie theory and Eq. (1). The dashed curve is the physical optics approximation by Eq. (28) of Ref. 2.

may have practical applications, however, even though it omits the fine structure in the scattering. For example, in the scattering by a spherical polydispersion of bubbles, the fine structure would be lost and the coarse structure retained if the spread of bubble sizes or wavelengths was not too large. Furthermore, the model may be useful in the design of instruments that depend on the scattering of light by bubbles. Examples include (a) devices for *in situ* optical measurement of microbubble populations at sea; (b) laser Doppler anemometry of bubbles in liquids; and (c) the detection of bubble imperfections in glass. Johnson and Cooke¹³ have used (a) to obtain evidence of a lack of bubbles at sea with radii of less than approximately $30\text{ }\mu\text{m}$, in apparent disagreement with similar acoustic measurements. Their instrument made use of scattering with $\phi \sim 90^\circ$, which is shown by Figs. 3 and 4 to be much smaller for microbubbles than for a geometric reflection from a perfect reflector. Both the physical optics approximation and the Mie theory suggest that bubble detection instruments relying on bistatic scattering should accept light with ϕ less than that of the first diffraction maximum as predicted by Eq. (2). Geometric optics¹² gives $I_r >$

1 for all $\phi \leq \phi_c$; consequently, it significantly overestimates the scattered intensity close to ϕ_c when $ka < 1000$.

Keller^{14,15} has attempted to use light scattering with $\phi \sim 90^\circ$ to measure the size spectrum of microbubbles in water for the purpose of testing models of cavitation. References 14 and 15 give angular scattering patterns (reported to be obtained from Mie theory) with $\lambda \sim 0.6328\text{ }\mu\text{m}/1.333$ and $a = 1, 5, 7.5$, and $10\text{ }\mu\text{m}$ (which correspond to $ka \sim 13, 66, 100$, and 132). Comparison of the results of our Mie program and model show that Keller's patterns err significantly; they do not include fine structure and they incorrectly describe the coarse structure.

We are grateful to W. J. Wiscombe for providing the initial computer program from which the program used here was derived and to H. Medwin for bringing the work of Johnson and Cooke to our attention. This research was supported in part by the Washington State University Research and Arts Committee and by the Office of Naval Research. P. L. Marston is an Alfred P. Sloan Research Fellow.

* Author to whom correspondence should be addressed.

REFERENCES

1. P. L. Marston, "Critical angle scattering by a bubble: physical optics approximation and observations," *J. Opt. Soc. Am.*, **69**, 1205-1211 (1979); **70**, 3530E (1980).
2. P. L. Marston and D. L. Kingsbury, "Scattering by a bubble in water near the critical angle: interference effects," *J. Opt. Soc. Am.*, **71**, 192-196 (1981).
3. G. Mie, "Beiträge zur Optik trüber Medien, speziell kolloidaler Metallösungen," *Ann. Phys. (Leipzig)*, **25**, 377-445 (1908).
4. H. C. van de Hulst, *Light Scattering by Small Particles* (Wiley, New York, 1957).
5. W. J. Wiscombe, "Improved Mie scattering algorithms," *Appl. Opt.*, **19**, 1505-1509 (1980).
6. R. H. Boll, R. O. Gumprecht, and C. M. Sliepcevich, "Theoretical light scattering coefficients for relative refractive indexes less than unity and for totally reflecting spheres," *J. Opt. Soc. Am.*, **44**, 18-21 (1954).
7. R. H. Boll *et al.*, *Tables of Light-Scattering Functions* (U. Michigan Press, Ann Arbor, Mich., 1958).
8. I. I. Zel'manovich and K. S. Shifrin, *Tables of Light Scattering. Part III - Coefficients of Extinction, Scattering, and Light Pressure* (Hydrometeorological Publishing House, Leningrad, 1968).
9. M. Kerker, *The Scattering of Light and Other Electromagnetic Radiation* (Academic, New York, 1969).
10. J. V. Dave, "Scattering of visible light by large water spheres," *Appl. Opt.*, **8**, 155-161 (1968).
11. W. J. Wiscombe, "Mie Scattering Calculations: Advances in Technique and Fast, Vector-Speed Computer Codes," NCAR Technical Note NCAR/TN-110+STR (National Center for Atmospheric Research, Boulder, Colo., 1979).
12. G. E. Davis, "Scattering of light by an air bubble in water," *J. Opt. Soc. Am.*, **45**, 572-581 (1955).
13. B. D. Johnson and R. C. Cooke, "Bubble populations and spectra in coastal waters: a photographic approach," *J. Geophys. Res.*, **84**, 3761-3766 (1979).
14. A. Keller, "Ein Streulicht Zahlverfahren, angewandt zur Bestimmung des Kavitationskeimspektrums," *Optik*, **32**, 165-176 (1970).
15. A. Keller, "The influence of the cavitation nucleus spectrum on cavitation inception, investigated with a scattered light counting method," *J. Basic Eng.*, **94**, 917-925 (1972).

SUPPLEMENT TO PAPER NO. 4

This supplement compares unpublished Mie computations (solid curve) with the physical-optics model from Paper 3 (dashed curve). The refractive index ratio is $n_i/n_o = 0.75$. The notation is as in Papers 3 and 4 except in Figures S1 and S2 we give the total normalized scattering $I_u = (I_1 + I_2) / 2$ for the case of unpolarized incident light. For Figures S3 - S5, scattering for the same ka but for the orthogonal polarization is given in Paper No. 4; the associated figure from that paper is noted in parenthesis.

FIGURE CAPTIONS FOR SUPPLEMENT

- | | |
|---------|---------------------------------------------------------------------------------------------------------------------------------------------------------------|
| Fig. S1 | Log (base 10) of I_u for $ka = 25$. |
| Fig. S2 | Log (base 10) of I_u for $ka = 100$. |
| Fig. S3 | I_1 for $ka = 100$ (see Fig. 3b). |
| Fig. S4 | I_2 for $ka = 1000$ (see Fig. 3a). |
| Fig. S5 | I_1 for $ka = 10000$ (see Fig. 2a). See also Fig. 4 of Paper 1 for ϕ from 75° to 85° . |
| Fig. S6 | Phase difference for scattering amplitudes (as in Fig. 5a,5b) for $ka = 25$. Note that the model does not give the fine structure present in the Mie result. |

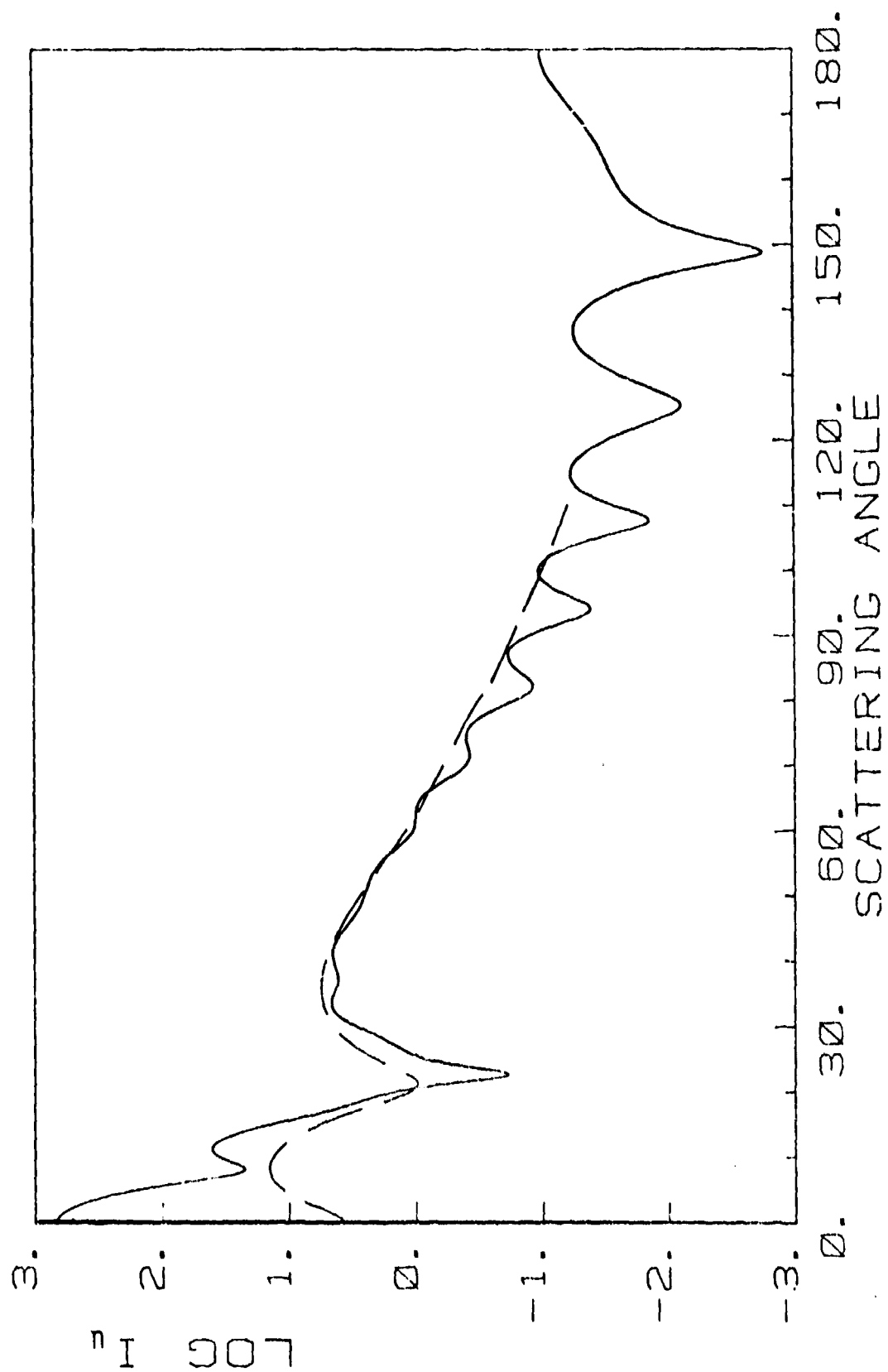


Fig. S1

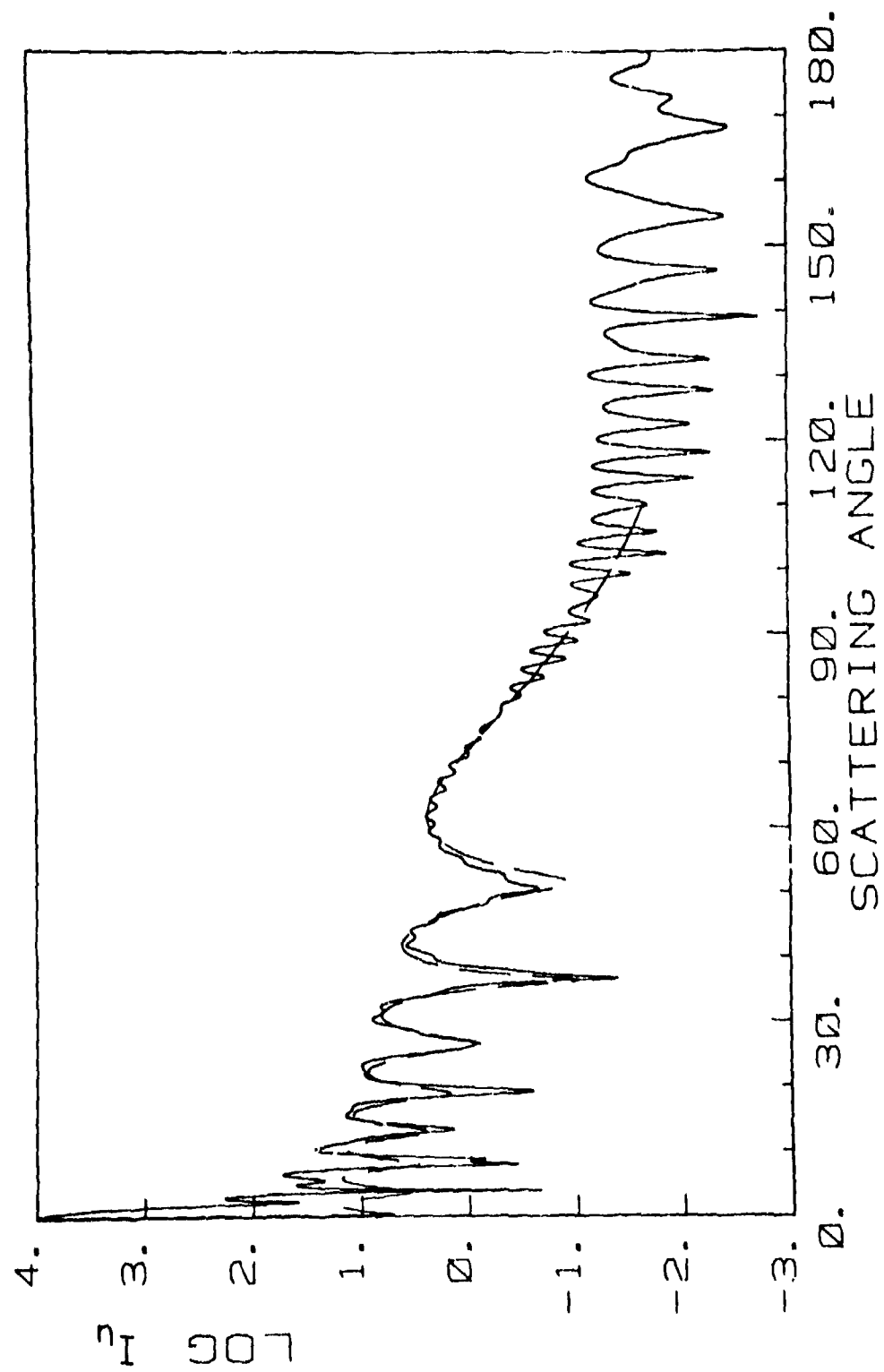


Fig. S2

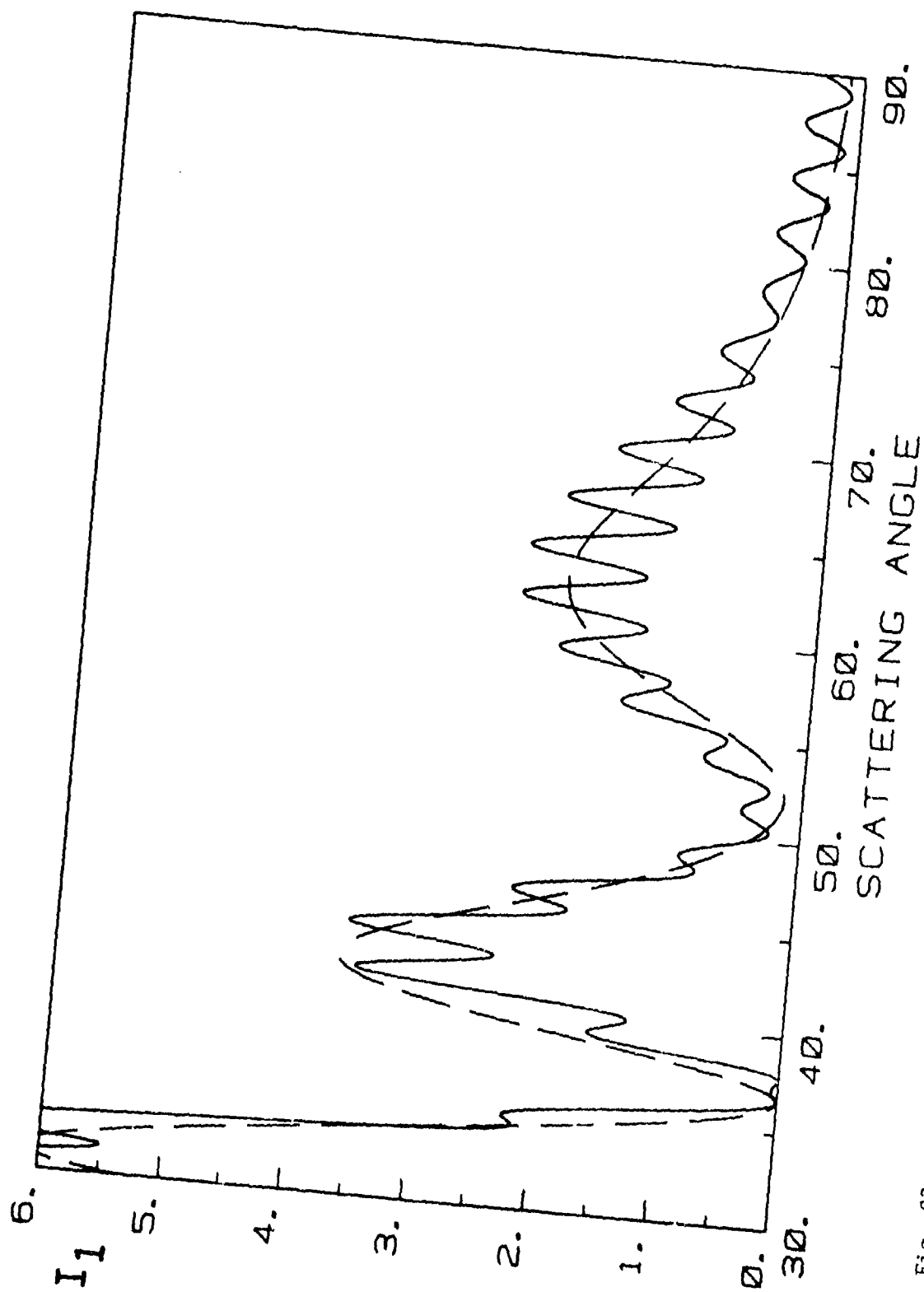


Fig. S3

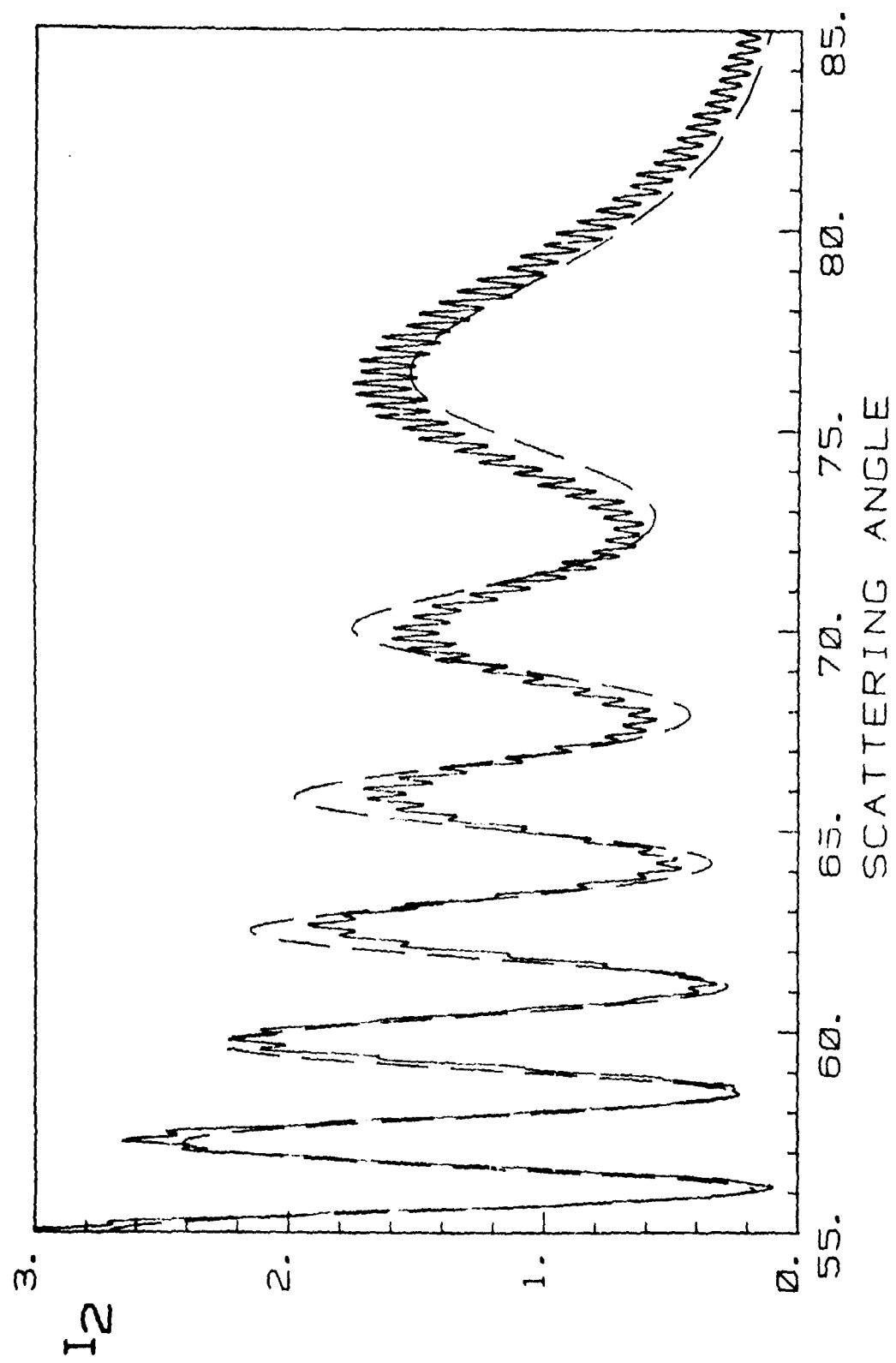


Fig. S4

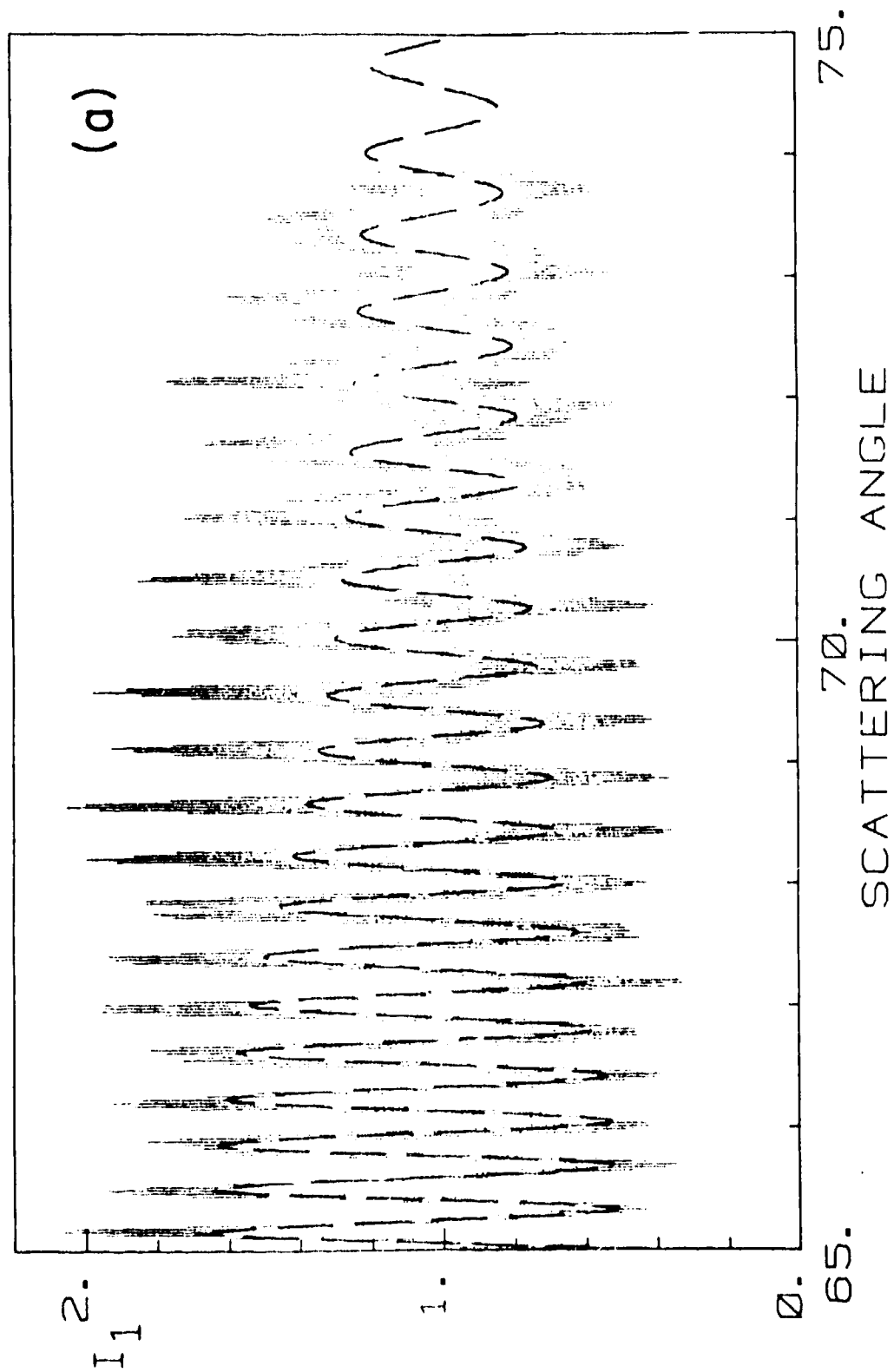


Fig. S5

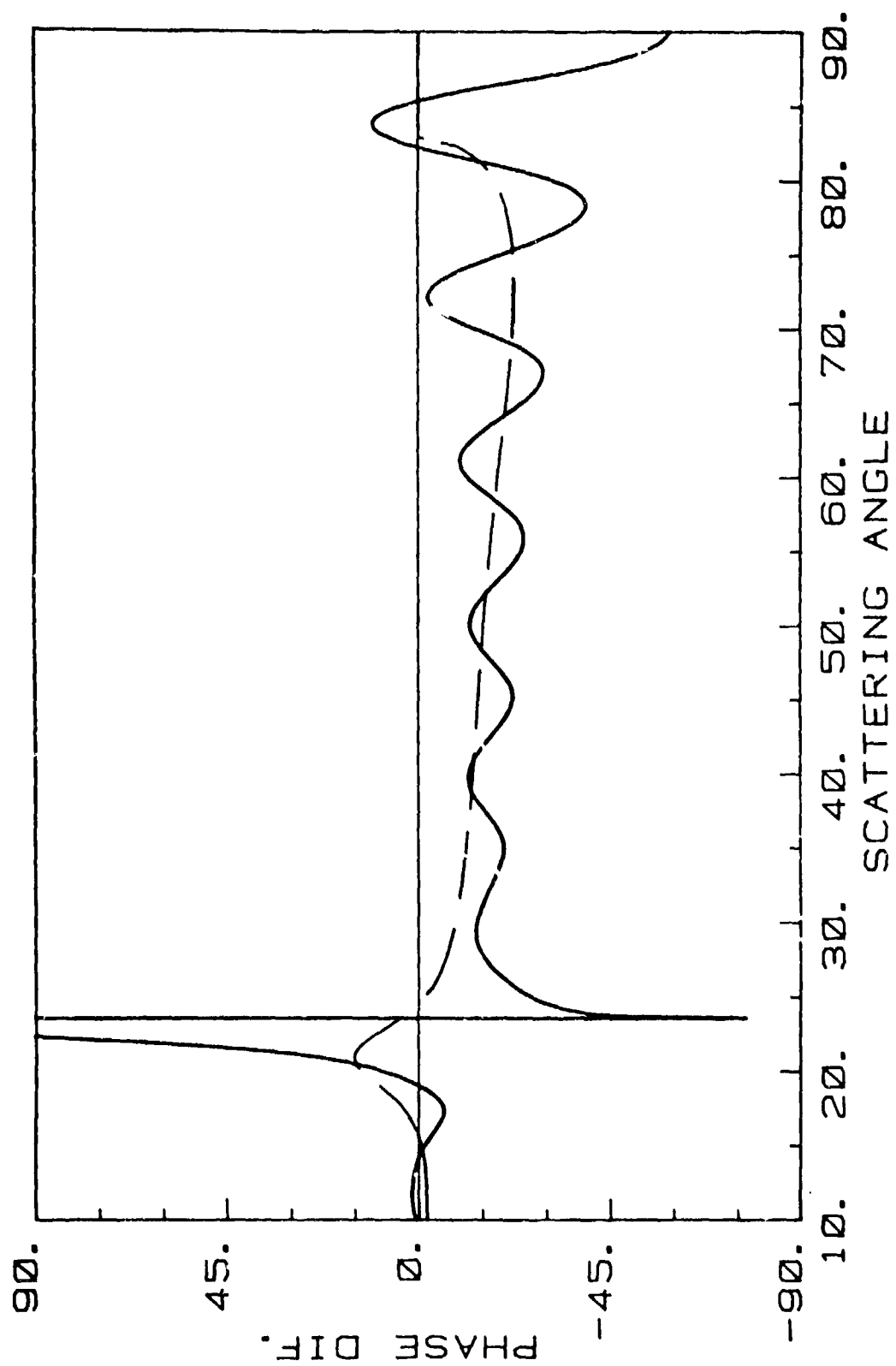


Fig. S6

Paper No. 5

Scattering by bubbles in glass: Mie theory and physical optics approximation (D. L. Kingsbury and P. L. Marston) Applied Optics, 2348-2350 (1981).

Scattering by bubbles in glass: Mie theory and physical optics approximation

Dwight L. Kingsbury and Philip L. Marston

When this work was done both authors were with Washington State University, Physics Department, Pullman, Washington 99164; Dwight Kingsbury is now with Boeing Commercial Airplane Company, P.O. Box 3707, Seattle, Washington 98124.

Received 14 January 1981.

0003-6935/81/142348-03\$00.50/0.

© 1981 Optical Society of America.

One of the causes of light scattering in glass is the presence of small gas bubbles. In critical applications such as optical fibers this scattering is not negligible; a microbubble trapped at the core-cladding interface may scatter a significant fraction of the light in the fiber.¹ Here we use Mie theory and physical optics to describe the main features of bubble scattering in glass. We anticipate that these results will be useful for the detection of bubbles in quality control applications.

We are unaware of prior publication of the Mie intensity for $0-180^\circ$ scattering from bubbles in any dielectric. Structure in the Mie scattering from bubbles can be related to diffraction and interference near the critical scattering angle and to the Brewster null in the reflectivity of parallel polarized light. For scattering from a sphere with a refractive index which exceeds that of the surroundings, the critical scattering angle is not present; also, the effect of the Brewster angle is less pronounced.

We approximate the bubble shape as a perfect sphere and

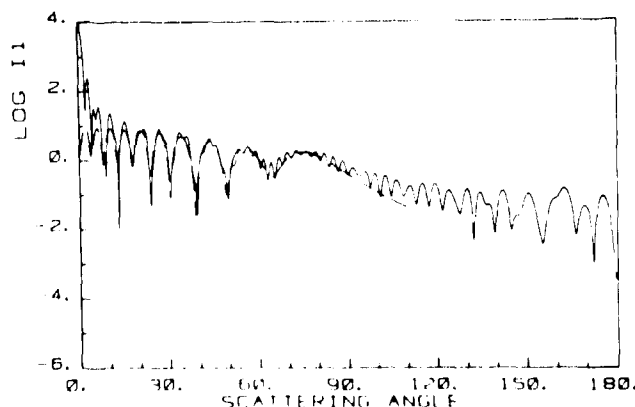


Fig. 1. Logarithm (base 10) of the normalized scattered intensity predicted by Mie theory (solid curve) for $ka = 100$ and the electric field perpendicular to the scattering plane. The dashed curve is the physical optics approximation given by Eq. (24) of Ref. 3 which is useful when scattering angle ϕ is close to the critical scattering angle $\phi_c \sim 94^\circ$. The approximation fails to describe forward region ($\phi < 20^\circ$) and the backward region ($\phi \sim 180^\circ$).

assume the glass has a refractive index of 1.46, as does the glass used in the cladding and outermost core layer of a typical optical fiber preform. (In the resultant fiber a bubble trapped at the core-cladding interface is broken up into a sequence of much smaller bubbles elongated in the direction the fiber is drawn.¹) We take the bubble gas to be air, so that the relative refractive index $n_i/n_o \approx 0.685$. A bubble is described by its size parameter ka , where $k = 2\pi/\lambda$, λ is the wavelength of the light in the glass, and a is the bubble radius. Here we consider bubbles with size parameters 5, 25, and 100. For $\lambda = 0.43 \mu\text{m}$ (which corresponds to 632.8 nm in air for visual inspection) $ka = 100$ gives $a = 6.9 \mu\text{m}$; $ka = 5$ gives $a = 0.35 \mu\text{m}$. For $\lambda = 0.56 \mu\text{m}$ ($0.82 \mu\text{m}$ in air, a typical operating condition of fibers) $ka = 100$ gives $a = 8.9 \mu\text{m}$.

If the bubble is illuminated by a collimated light beam, the

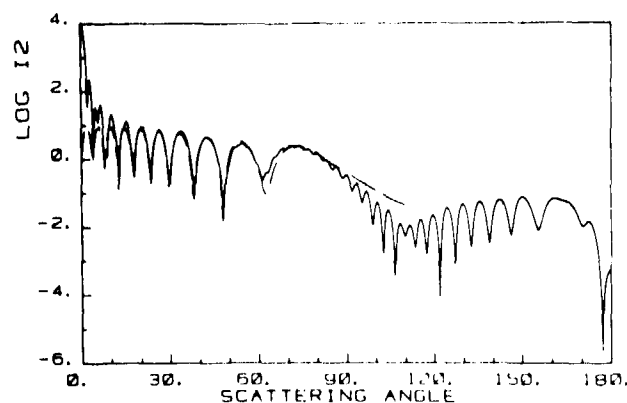


Fig. 2. Like Fig. 1 but with electric field parallel to the scattering plane ($j = 2$ scattering).

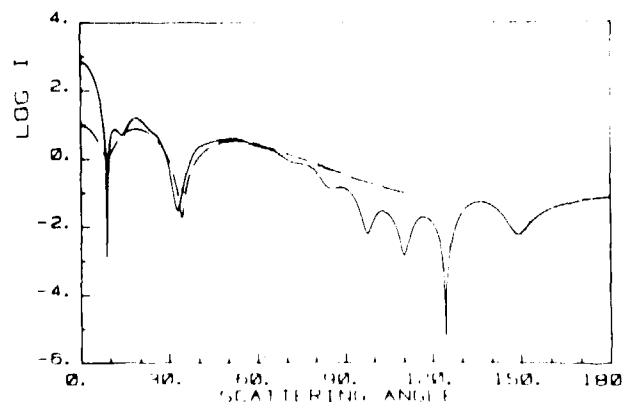


Fig. 3. Scattering for $ka = 25$. Mie theory for $j = 1$ (dotted curve) and $j = 2$ (solid curve). Dashed curve is I_1 from physical optic approximation.

angular distribution of the scattered intensity is described by Mie theory.² At a distance $R \gg k\alpha^2$ from the bubble center and a scattering angle ϕ , the j -polarized scattered intensity is given by the incident j -polarized intensity multiplied by $I_j(\phi)(\alpha/R)^2/4$, where $j = 1$ denotes polarization of the electric vector perpendicular to the scattering plane, $j = 2$ the parallel case. The normalization of the functions $I_j(\phi)$ is chosen so that $I_j(\phi) = 1$ represents perfect reflection according to geometric optics.^{3,4} Using a program described in Ref. 5 incorporating a modified version of the MIEVO subroutine developed by Wiscombe,⁶ we obtain the $I_j(\phi)$ functions shown in Figs. 1-4.

The coarse structure in the vicinity of the critical scattering angle ϕ_c may be understood with reference to a physical optics approximation developed by Marston.^{3,7} Most of the scattered intensity in this region is due to three types of rays which we denote by the parameters $p = 0, 1, 2$, where p is the number of chords within the bubble and the $p = 0$ ray has only an external reflection.⁴ When the local angle of incidence θ satisfies $\sin\theta \geq \sin\theta_c = n_i/n_o$, the $p = 0$ ray is nearly³ totally reflected; the abrupt boundary of total reflection at θ_c results in a far-field diffraction pattern of this ray. Rays with $\theta < \theta_c$ are mostly transmitted inside the bubble. Rays with $p = 1$ are refracted twice and interfere with $p = 0$ rays in the region $\phi < \phi_c$, where $\phi_c = \pi - 2\theta_c$ is the scattering angle of rays incident at θ_c . Marston's physical optics approximation considers the diffraction and interference of $p = 0$ and 1 rays. Small quasi-periodic fine-structure variations ride on the large quasi-periodic coarse-structure variations and are due mainly to the interference of certain neglected $p = 2$ rays ($p = 2'$ rays in the notation of Refs. 3 and 5). If the average intensity over an angular range containing several fine-structure variations is desired, the approximation may be used to predict I_j in the range $20^\circ \leq \phi \leq \phi_c = 93.54^\circ$. This model breaks down for small bubbles, as can be seen in Fig. 4, due to its use of the Fresnel reflection and transmission coefficients of planar interfaces and the stationary phase approximation of diffraction integrals.

The physical optics approximation predicts a quasi-period $\leq (\lambda/\alpha)^{1/2}$ rad for the coarse structure, and a fine-structure quasi-period of $0.95(\lambda/\alpha)$ at ϕ_c , decreasing³ with ϕ . These features are clearly evident for $k\alpha = 25$ and 100, as is the predicted broad decline in intensity for $\phi > \phi_c - \arcsin[1.2(\lambda/\alpha \cos\theta_c)^{1/2}]$ (identified in Ref. 5 as the approximate location of the last coarse-structure maximum).

The broad minimum in I_2 near 110° corresponds to light scattered from the Brewster angle: parallel polarized light incident on a plane glass-air interface is totally transmitted when $\theta = 34.41^\circ$. Thus, when $k\alpha$ is large enough to use the Fresnel coefficients, we expect a negligible contribution to I_2 at $\phi = 180^\circ - 2(34.4^\circ) = 111.2^\circ$ from the externally reflected ($p = 0$) ray. This ϕ can also be written as $2 \arctan(n_o/n_i)$.

For $k\alpha = 5$ (Fig. 4), the fine-structure quasi-period is approximately equal to the coarse-structure quasi-period. The minimum in I_2 at 102° and the slight dip around 45° are the last remnants of this structure. As $k\alpha$ is reduced below 5, we find that the scattering pattern approached that of a dipole radiator, as predicted by Rayleigh scattering theory: $I_1(\phi)$ becomes a flat line, and $I_2(\phi)$ is symmetrical about a minimum at 90° .

We have compared these plots with others made for $n_i/n_o = 0.75$ (air bubbles in water) for the same values of $k\alpha$ and found them, as expected, quite similar. The most noticeable difference is the slightly larger quasi-periods for bubbles in glass. In both cases, the best angles to look for scattering will be those angles where $\phi \leq \phi_c - (\lambda/\alpha)^{1/2}$. Corrections are sometimes needed⁷ when computing the effective scattering

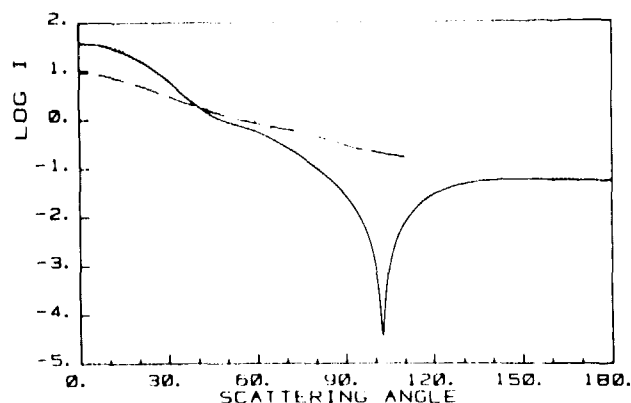


Fig. 4. Like Fig. 3 but with $k\alpha = 5$.

angle observed by a detector due to refraction of the scattered light as it leaves the glass and enters the detector.⁹ The coarse and fine structures present when $k\alpha \geq 25$ may be used to obtain independent estimates of α . That diffraction is important at ϕ_c can be seen by comparing the Mie results to the geometric prediction,⁴ including only the $p = 0$ ray, that $I_j(\phi_c) = 1$ and with the physical optics prediction that $I_j(\phi_c) = 0.25$; the Mie results lie much closer to the latter than the former.

The result that scattering is best observed when $\phi \leq \phi_c - (\lambda/\alpha)^{1/2}$ rad can also be used in certain cases for scattering by nonspherical bubbles if their approximate size is known. For example, if the bubble is spheroidal and either the major or the minor axis lies in the scattering plane, the critical scattering angle predicted by ray optics is the same as that predicted for a sphere. The diffraction related shift in the first maximum is roughly $(\lambda/\alpha)^{1/2}$ rad, where α becomes an average (which depends on the orientation of the spheroid) of the semimajor and semiminor axes. The details of the coarse and fine structures will depend on the bubble's shape.

The approach to the scattering described here is to allow the light to enter and leave the glass via plane surfaces and to neglect surface reflections.⁹ Scattering near 90° has been used to detect bubbles in glass.¹⁰ For glasses with $n_o/n_i = 1.5$, $\phi_c = 96.4^\circ$ and the Brewster scattering angle is 112.6° . Previous applications of Mie theory to bubbles are reviewed in Refs. 5 and 11. Approximations for scattering by inhomogeneities within fiber waveguides have recently been published,^{12,13} but these do not describe the angular structure for scatterers with $k\alpha \geq 1$.

This work was supported by the Office of Naval Research. P. L. Marston is an Alfred P. Sloan Research Fellow.

References

1. A. R. Tynes, A. D. Pearson, and D. L. Bisbee, *J. Opt. Soc. Am.* **61**, 143 (1971).
2. G. Mie, *Ann. Phys. (Leipzig)* **25**, 377 (1908).
3. P. L. Marston and D. L. Kingsbury, *J. Opt. Soc. Am.* **71**, 192, E917 (1981).
4. G. E. Davis, *J. Opt. Soc. Am.* **45**, 572 (1955).
5. D. L. Kingsbury and P. L. Marston, *J. Opt. Soc. Am.* **71**, 358 (1981).
6. W. J. Wiscombe, *Appl. Opt.* **19**, 1505 (1980).
7. P. L. Marston, *J. Opt. Soc. Am.* **69**, 1205 (1979); **70**, 353 (E) (1980).

8. There may be an exception to this guideline for large spherical bubbles because backscattering can be enhanced by the axial focusing of $p \approx 3$ glory rays. Observations of this enhancement for bubbles in liquids are described in P. L. Marston and D. S. Langley, *J. Opt. Soc. Am.* **70**, 1607 (1980).
9. Refraction corrections, such as those described in Ref. 7, are simplified when the light enters and leaves the scattering volume via plane interfaces, and a lens is used to place the detector in the far field. This may be achieved by immersing the glass in an index-matching liquid and illuminating and observing it via windows.
10. U.S. Ordnance Department (Document 2037), *The Manufacture of Optical Glass and of Optical Systems. A War-Time Problem* (U.S. GPO, Washington, D.C., 1921), pp. 205, 206.
11. D. L. Kingsbury, M.S. Thesis, Washington State U. (1981).
12. N. Morita and N. Kumagai, *IEEE Trans. Microwave Theory Tech.* **MTT-28**, 137 (1980).
13. N. K. Uzunoglu, *J. Opt. Soc. Am.* **71**, 259 (1981).

Paper No. 6

Description of computer codes for Mie and model computations
(D. L. Kingsbury and P. L. Marston) [This is a slightly
modified version of an Appendix in D. L. Kingsbury,
"Light Scattering Near the Critical Angle in Air Bubbles
in Water and Glass," M. S. Thesis, Washington State Uni-
versity (1981).]

Appendix

COMPUTER CODES

Three programs were used to generate our plots. MIESC, incorporating a modified version of Wiscombe's MIEVO, produced the Mie and CRIT the approximation results. The versions given here store results in disk data files where they can be accessed by the plotting routine MIEPL for display on the HP 2847A monitor or for paper plots on the HP 9872A plotter. All programs are written in Hewlett-Packard RT-IVB Fortran. CRIT evaluates the approximation developed by Marston and Kingsbury (1981).

MIESC

MIESC asks for the following inputs:

1. REF INDX is the complex relative refractive index n_i/n_o . The imaginary part must be non-positive.
2. BETA is the size parameter $ka = 2\pi a/\lambda$, where λ is the wavelength in the outer medium.
3. AST is the smallest scattering angle for which scattering angle for which scattering functions are computed, DPHI the angle step size, and NUMANG = N_{ang} is the total number of angles.

If NUMANG is even, results are calculated for the angles

$\phi_i = AST + i(DPHI)$, $i = 0$ to NUMANG/2, and their complementary

angles $(180^\circ - \phi_i)$. (If NUMANG = 1, 90° must be the only angle. If NUMANG = 0, only the extinction efficiency factor Q_{scat} is computed.)

For example, if $n_i = 1.33 - i(.05)$, $n = 1.0$, and scattering functions are desired for $\phi = 40^\circ$ to 90° with increments of $.5^\circ$, one should type in

/.7508,-.0282,40.,.5,101

MIESC then asks for the name and cartridge number of an existing datafile in which to store the output. What data is stored depends on what the output buffer RBUF has been equivalenced to. In the version included here, each record will consist of three real numbers giving ϕ , $I_1(\phi)$, and $I_2(\phi)$, and the records are entered in order of increasing ϕ , except that the record for $(180^\circ - \phi)$ immediately follows that for ϕ .

If the phase difference DIFA is not desired, the code that computes PH1, PH2, and DIFA is skipped.

To bring subroutine MIEVO down to more manageable size, the original comments were largely omitted. The commented version is given in Wiscombe (1979). Most complex variables have been converted to 2-dimensional arrays or to separate variables prefixed with "R" or "I." For example, NUM became NUM(1) and NUM(2), denoting the real and imaginary parts, respectively, and

ZET became RZET and IZET. (This was done because of the absence of double precision Fortran in RT-IVB Fortran.) Most complex arrays were similarly converted to separate arrays for the real and imaginary components.

Subroutine names prefixed with "DV" refer to functions in the HP Vector Instruction Set, which considerably speeded up the execution of two former DO-loops.

To keep the loaded program within a 32K size limit, the original MIEVO's complex BIGA array was discarded. (BIGA, which stored the A_n , contained as many elements as the number of terms used in the Mie series. Thus for $ka = 10\ 000$, a total of $2(10\ 088) = 20\ 176$ double precision must be stored, requiring 161 408 bytes.) Required A_n values are instead stored on and retrieved from a system disk using EXEC calls.

The use of the Hewlett-Packard minicomputer instead of a regular "pay" computer system was absolutely necessary. Extrapolation from Table 8 of Wiscombe (1980) indicates a MIEVO execution time of over 100 seconds on a CRAY-1 for $ka = 10\ 000$ and $NUMANG = 8000$. The several size parameters, repeated testing, and dozens of plots required made our choice of computer systems inevitable.

CRIT

Required CRIT inputs are the relative refractive index RI (now assumed real); the size parameter BETA; PTS and STRT, which determine the angles for scattering computations; and LAST ANGLE, the largest PH (ϕ). $N = n_o/n_i = 1/RI$ is used to calculate the critical incident angle θ_c :

$$THC = \arcsin(1/N).$$

(Arctangents are used in the program due to the unavailability of the arcsin function.) The critical scattering angle ϕ_c is then

$$PHC = \pi - 2(THC).$$

For a given incident angle TH-THC, the angle PH at which the refracted ray is scattered is given by an equation derived using Snell's Law and elementary geometry

$$PH = 2(\arcsin[\sin(TH)/N] - TH).$$

For a desired smallest PH, one chooses STRT such that TH = STRT(THC) substituted in the above equation gives this PH.

As CRIT executes, TH is stepped up in increments of $E = (THC - TH_{init})/PTS$. As TH approaches THC the corresponding step sizes for PH grow steadily. Consequently, at selected angles TH2, TH3, and TH4, the step size in TH is reduced.

The function G1 is the geometrical divergence factor

$$G1 = \frac{\sin(TH) \cos(TH)}{2[1 - [N \cos(TH) / \cos(R)] \sin(PH)]}$$

in the expression for the intensity of refracted radiation (Davis, 1955; van de Hulst, 1957), where $R = \arcsin(N \sin(TH))$.

IP and IS are the intensities of the parallel and perpendicular refracted radiation, respectively, computed using Fresnel's intensity transmission coefficients $(1 - FP)$ and $(1 - FS)$ for plane surfaces. The coefficients are squared because this radiation is refracted twice -- at entrance and at exit.

The variable W is the upper limit of integration on the Fresnel integral used in the reflected radiation calculation (Marston, 1979). Subroutine FRES evaluates this integral using a numerical approximation (Abramowitz and Stegun, 1965).

The phase differences B1 and B2 between the reflected and refracted rays for perpendicular (B1) and parallel (B2) polarization have three components: the phase shift the reflected ray undergoes at the bubble surface (DEL1 and DEL2), the phase path difference ETAC, and a $\pi/4$ phase difference arising from the curvature of the scattered wavefront. (For the reflected ray this phase shift is already included in the Fresnel integral.)

CRIT is now ready to compute the scattering functions at angle PH:

$$S_1 = \sqrt{IS} + (1/\sqrt{2})(FC + iFS)\exp(-iB1)$$

$$S_2 = \sqrt{IP} + (1/\sqrt{2})(FC + iFS)\exp(-iB2)$$

where FC and FS are the output of subroutine FRES.

MIEPL

Output was plotted by program MIEPL using the HP 1000 Graphics package. MIEPL is not included in the program listing which follows.

REFERENCES:

- Davis, G. E., "Scattering of light by an air bubble in water," J. Opt. Soc. Am. 45, 572-581 (1955).
- Marston, P. L., "Critical angle scattering by a bubble: physical-optics approximation and observations," J. Opt. Soc. Am. 69, 1205-1211 (1979); 70, 353(E) (1980).
- Marston, P. L. and D. L. Kingsbury, "Scattering by a bubble in water near the critical angle: interference effects," J. Opt. Soc. Am. 71, 192-196 (1981).
- van de Hulst, H. C., Light Scattering by Small Particles, (Wiley, New York, 1957).
- Wiscombe, W. J., "Mie Scattering Calculations: Advances in Technique and Fast, Vector-Speed Computer Codes," NCAR Technical Note NCAR TN-140-STR (National Center for Atmospheric Research, Boulder, Colo., 1979).
- _____, "Improved Mie scattering algorithms," Appl. Opt. 19, 1505-1509 (1980).

T=00003 Is ON CR00027 USING 00059 BLKS P=0000

```

FTN4,L
C*****Dwight Kingsbury, 1 JUL 80*****
      BLOCK DATA
      COMPLEX SBACK,S1,S2
      DOUBLE PRECISION BETA,XMU,PI
      REAL N2OUT
      COMMON/INOUT/PI(2),SBACK,S1(512),S2(512),BETA,XMU(512),N2OUT,
      *   NUMANG,NMPI,NN,DBET,LUOUT,ICNMD,ILEN,ISECT,NB0,IOP10,IOP20
      END
      PROGRAM MITSO
      ANGULAR DIMENSIONS
      COMPLEX SBACK,S1,S2
      DOUBLE PRECISION BETA,XMU,PI,DBET,RI,CON,AST
      C
      REAL N2OUT,I1,I2,INTEN
      DIMENSION ICOR(14),PBUFF(3),NAME(3)
      COMMON/INOUT/PI(2),SBACK,S1(512),S2(512),BETA,XMU(512),N2OUT,
      *   NUMANG,NMPI,NN,DBET,LUOUT,ICNMD,ILEN,ISECT,NB0,IOP10,IOP20
      EQUIVALENCE (PBUFF(1),ANGLE),(PBUFF(2),I1),(PBUFF(3),I2)
      DATA ISECT,IOP1,IOP2,ICOR(14),IOP10,IOP20,ILEN
      C
      IL=DIM(PBUFF)*2
      LUIN=LUCLU(10)
      WRITE(LUIN,2000)
      2000 FORMAT("PRINTOUT, STOPCOUNT, COMPUTE PHASES? (Y OR N S)")
      READ (LUIN,2001) IR,IST,IPH
      2001 FORMAT("3H")
      IF (IR.EQ.1HY) LUOUT = 6
      IF (IR.NE.1HY) LUOUT = LUIN
      N2OUT = 0.
      PI = 3.14159265358979
      CON = PI/180.
      SCON = SIN(SCON)
      WRITE(LUIN,2002)
      2002 FORMAT("ENTER CHAN REF INCM, BETA,DBET,AST,DBHI,NUMANG")
      READ(LUIN,*) PI(1),PI(2),BETA,DBET,AST,DBHI,NUMANG
      C
      FUNCTIONS FOR NUMERICAL INTEGRATION OVER SOLID ANGLE
      SAST = SIN(SCON*AST*SCON)
      DBTER = (DBHI*SCON)**2
      IF(IST.NE.1HY) GOTO 2
      WRITE(LUIN,2003)
      2003 FORMAT("ENTER FILE# CHS1, OR NO,(2 CHS)")
      READ(LUIN,2004) NAME(1),NAME(2),NAME(3),ICR
      2004 FORMAT("3H")
      CALL OPEN(ICOR,ISF,NAME,IOP10,ISC,ICR)
      IF (ICR.EQ.0) GO TO 229
      PBUFF(1) = BETA
      PBUFF(2) = PI(1)
      PBUFF(3) = PI(2)
      CALL WRITE(IPH,ISF,PBUFF,IL)
      2
      NUMUM = (NUMANG/512)+1
      C
      IF NUMERICALION DESIRED, MULT S FILE BY 0.1'S BY 0**2
      042,043
      042=0**2
      NUMA = NUMUM*NUMANG/512
      DO 14 I=1,NUMUM
      IF (NAME(3).EQ.0) GOTO 6
      IF (ICOR.NE.0) NAME(3)=NUMA+1
      IF (ICOR.NE.0) NUMANG = 512

```

```

      NMP1 = NUMANG*1
      NN = NMP1/2
      DO 4 I = 1,NN
4 XNUK(I) = DDBSC*(AST+(I-1)*DPHI)+CONJ
C
6 CALL MIEV0(I)
  IF (NUMANG.EQ.0) GOTO 12
  TINT = 0.
  DO 10 I = 1,NN
  RK = 0.
  ANGLE = AST+(I-1)*DPHI
C   PH1, PH2 ARE THE PHASE ANGLES IN DEGREES; PHDIF IS DIFFERENCE
  IF (IPH.NE.100) GOTO 7
  PH1=-57.2958*ATANH(AMAG(S1(I)*VREAL(S1(I)))
  PH2=-57.2958*ATANH(AMAG(S2(I)*VREAL(S2(I)))
  IF (REAL(S1(I)).LT.0.) PH1=PH1+180.
  IF (PH1.GT.180.) PH1=PH1-360.
  IF (REAL(S2(I)).LT.0.) PH2=PH2+180.
  IF (PH2.GT.180.) PH2=PH2-360.
  PHDIF=PH2-PH1
  IF (PHDIF.GT.180.) PHDIF=PHDIF-360.
  IF (PHDIF.LT.-180.) PHDIF=PHDIF+360.
7 I1 = (REAL(S1(I))*2+AIMAG(S1(I))*2
  I1 = (I1*Q2)
  I2 = (REAL(S2(I))*2+AIMAG(S2(I))*2
  I2 = (I2*Q2)
  INTEN = ALOG10(.5*(I1+I2))
  DECPOL = (I2-I1)/(I2+I1)
  IF (AMOD(ANGLE,2.)EQ.0) WRITE(LUOUT,1001) ANGLE,I1,I2
  IF (IST.EQ.100) CALL WRITE(IOC6,IERR,REOF,IL)
C   DO COMPLEMENTARY ANGLE
C   IF COMPL. ANGLE FUNCTIONS DESIRED, THE FINAL DO-LOOP IN
C   SUBROUTINE MIEV0 CANNOT EXCLUDE 8-NMP1-J) ENDS
  ANGLE = 180-ANGLE
  IF (NUMANG.EQ.1) GOTO 12
  I1C = (REAL(S1(NMP1-I)))*2+AIMAG(S1(NMP1-I))*2
  I1 = (I1*Q2)
  I2C = (REAL(S2(NMP1-I)))*2+AIMAG(S2(NMP1-I))*2
  I2 = (I2*Q2)
  INTEN = ALOG10(.5*(I1+I2))
C   THESE LINES PERFORM SOLID ANGLE INTEGRATION AT PHI=PI/4
8 ZINT = (COS(PH)*CONJ)*2*(I1+I1C) + (SIN(PH)*CONJ)*2*(I2+I2C)
  TINT = TINT+Z*ZINT*STEP
  RK = RK+DPHI
  IF (SIN(ANGLE)*CONJ+CONJ*PH*CONJ+GE/SAST) GOTO 8
  IF (AMOD(ANGLE,2.)EQ.0) WRITE(LUOUT,1001) ANGLE,I1,I2
C
10 CONTINUE
  RLINT = ALOG10(TINT)
  ANGLE = BETA
  I1 = PLINT
  I2 = PLINT
  IF (IST.EQ.100) CALL WRITE(IOC6,IERR,REOF,IL)
  WRITE(LUOUT,1001) ANGLE,BETA,TINT,PLINT
C
12 AST = 180-ANGLE+DPHI
C   STOP AST NOT USED FOR SOLID ANGLE INTEGRATION
12 BETA = BETA+DBET
  CALL EXCOS(PI)
  IF (BETA.LE.135) GOTO 6
14 CONTINUE
  CALL EXCOS(PI)

```

```

C
999 IF(IST.EQ.144) CALL CLOSE(1008)
WRITE(LUIN,2007) IEPR
2007 FORMAT("IERR=",I5)
C      USE THIS FORMAT FOR MORE DETAILED OUTPUT
1000 FORMAT(1H1,5X,"MIE SIZE PARAMETER = (F8.2,15X,"REFRACTIVE ",
* "INDEX = (D14.6,E12.3//", "ANGLE",11X,"S-SUB-1",21X,"S-SUB-2",
* "15X", "INTENSITY",12X,"DEGPOL",18X,"I1",12X,"I2")
1001 FORMAT(F7.2,E14.6,F8.4,E14.6,E6.3)
1002 FORMAT(F7.2,F12.3)
      END
C
      SUBROUTINE MIEV0(I0)
      COMPLEX SBACK, S1, S2
      DOUBLE PRECISION BETA,XMU,RI
      REAL N2OUT
      COMMON/INOUT/PI(2),SBACK,S1(512),S2(512),BETA,XMU(512),N2OUT,
*      NUMANG,NMPI,NOI,NOET,LUOUT,ICNWD,ILEN,ISET,MRO,IOP10,IOP20
      LOGICAL NOINAG, NOANGS
      COMPLEX ANMI,BNMI
      DIMENSION RSP(256),ISP(256),RSM(256),ISM(256),RSPS(256),ISPS(256),
*      RSMX(256),ISMX(256),PIN(256),PINMI(256),TMP(256),TAUN(256)
      DOUBLE PRECISION RBIG,IBIG,PIN,PINMI,NP1DN,COEFF,VTEM(256),
*      RSP,ISP,PSN,ISM,RSPS,ISPS,RSM,ISM,AN(2),BN(2),RANP,IANP,
*      RBNP,IBNP,RANPM,IANPM,RBNPM,IBNPM,RZET,IZET,PZETN,IZETN,
*      RZINP1,IZINP1,TMP,TAUN,REZ,REZINW,FN,PH,FNP1,TWONP1,RNP1,
*      ZINX(2),FFX(2),AN(2),DEN(2),NUM(2),EPS1,EPS2,TEM(2),TMA(2),
*      NTH(2),DTDC(2),TTC(2),RIDIRV,PSIN,PSINP1,CHIN,CHINP1,BUFF(32)
      EQUIVALENCE (S1(1),PIN(1)),(S2(1),TAUN(1)),
*      (S1(257),PINMI(1)),(S2(257),TMP(1))
      DATA EPS1/1.0-2I, EPS2/1.0-9I, MAXIT/10000/
C
C
      IF(BETA.LT.0. .OR. RI(1).LE.0. .OR. RI(2).GT.0.) STOP 1000
      NOANGS = NUMANG.EQ.0
      NOINAG = RI(2).GE.N2OUT
C
C
C      CALCULATE NUMBER OF TERMS IN MIE SERIES (A LEAST UPPER BOUND)
C      USING EMPIRICAL FORMULAE FITTED FOR SIZE PARAMETERS UP TO
C      20,000
C
7 IF(BETA.LT.4200.) NT = BETA+4.05+BETA*(1.1/3.)+2.
IF(BETA.GE.4200.) NT = BETA+4.+BETA*(1.1/3.)+2.
NTP1 = NT+1
C
C
C      COMPUTE BIGA
C
      IF IC > 1 ARRAY BIGA HAS ALREADY BEEN GENERATED
10 IF (IC.GT.1) GO TO 200
      ITRM = 14
      RESERVE SPACE ON SYSTEM DISC FOR ARRAY BIGA
      CALL EREQ(4,ITRM,ISTRM,DISC,ISET)
      ICNWD = DISC
      ILEN = 100
      IOP1 = IOP1+1
      IOP2 = IOP2+2
      CALL GCDV(0,100,0,RI,TEM)

```

```

      ZINV(1) = TEM(1)/BETA
      ZINV(2) = TEM(2)/BETA
C
C      PREPARE FOR DOWN-RECURRENCE---
C      COMPUTE INITIAL HIGH-ORDER BIGA-H USING LENTZ METHOD
C
15  FFC(1) = NTP1*ZINV(1)
    FFC(2) = NTP1*ZINV(2)
    NM = -1
    KK = 2*NT+3
    AKC(1) = (NM*KK)*ZINV(1)
    AKC(2) = (NM*KK)*ZINV(2)
    DENK(1) = AKC(1)
    DENK(2) = AKC(2)
    CALL DCDVK(0,100,0,FF,TEM)
    NUMK(1) = DENK(1) + TEM(1)
    NUMK(2) = DENK(2) + TEM(2)
    KOUNT = 1
C
20  KOUNT = KOUNT+1
    IF(KOUNT.GT.NMAXIT) GO TO 40
    CALL DCDVK(-1,NUMK(1),NUMK(2),AK,TEM)
    CALL DCDVK(-1,DENK(1),DENK(2),AK,TMA)
    IF (TEM(1).GT.EPS1 .AND. TMA(1).GT.EPS1) GO TO 30
C      ILL-CONDITIONED CASE--STRIDE TWO TERMS INSTEAD OF ONE
    NM = -NM
    KK = KK+2
    AKC(1) = (NM*KK)*ZINV(1)
    AKC(2) = (NM*KK)*ZINV(2)
    NTHK(1) = AKC(1)*NUMK(1) - AKC(2)*NUMK(2) + 100
    NTHK(2) = AKC(1)*NUMK(2) + AKC(2)*NUMK(1)
    DTDK(1) = AKC(1)*DENK(1) - AKC(2)*DENK(2) + 100
    DTDK(2) = AKC(1)*DENK(2) + AKC(2)*DENK(1)
    CALL DCDVK(0,NTHK(1),NTHK(2),DTD,TEM)
    TMAK(1) = TEM(1)*FFC(1) - TEM(2)*FFC(2)
    FFC(2) = TEM(1)*FFC(2) + TEM(2)*FFC(1)
    FFC(1) = TMAK(1)
    NM = -NM
    KK = KK+2
    AKC(1) = (NM*KK)*ZINV(1)
    AKC(2) = (NM*KK)*ZINV(2)
    CALL DCDVK(0,NUMK(1),NUMK(2),NTH,TEM)
    NUMK(1) = AKC(1) + TEM(1)
    NUMK(2) = AKC(2) + TEM(2)
    CALL DCDVK(0,DENK(1),DENK(2),DTD,TEM)
    DENK(1) = AKC(1) + TEM(1)
    DENK(2) = AKC(2) + TEM(2)
    KOUNT = KOUNT+1
    GO TO 20
C
30  CALL DCDVK(0,NUMK(1),NUMK(2),DEN,TT)
    TENK(1) = TT(1)*FFC(1) - TT(2)*FFC(2)
    FFC(2) = TT(1)*FFC(2) + TT(2)*FFC(1)
    FFC(1) = TENK(1)
C      CHECK FOR CONVERGENCE
    IF(DABS(TENK(1)-100).LT.EPS2 .AND. DABS(TENK(2)-100).LT.EPS2) GO TO 50
    NM = -NM
    KK = KK+2
    AKC(1) = (NM*KK)*ZINV(1)
    AKC(2) = (NM*KK)*ZINV(2)

```

```

      CALL DCDVX(0.1D0,0.,NUM,TEM)
      NUM(1) = AK(1) + TEM(1)
      NUM(2) = AK(2) + TEM(2)
      CALL DCDVX(0.1D0,0.,DEN,TEM)
      DEN(1) = AK(1) + TEM(1)
      DEN(2) = AK(2) + TEM(2)
      GO TO 20
C
      40 WRITE(OUTPUT,8001) NT, BETA,PI,AK,NUM,DEN,TT,FF
      8001 FORMAT(2,' CONTINUED FRACTION FOR A-SUB-NT FAILED TO CONVERGE'
      * ' NT= ',1E20,' B= ',1E20,' REFR INDEX= ',1.2E20,' AK= ',1.2E20,'
      * ' NUM= ',1.2E20,' DEN= ',1.2E20,' TT= ',1.2E20,' FF= ',1.2E20,'
      STOP 1002
C
      50 RBIG = FF(1)
      IBIG = FF(2)
      BUFF(31) = RBIG
      BUFF(32) = IBIG
      NB = 31
C
      C      DOWNWARD RECURRENCE FOR BIG-N
C
      DO 70 N = NT,2,-1
      TEM(1) = N+ZINV(1) + RBIG
      TEM(2) = N+ZINV(2) + IBIG
      CALL DCDVX(0.1D0,0.,TEM,TMA)
      RBIG = N+ZINV(1) - TMA(1)
      IBIG = N+ZINV(2) - TMA(2)
      NB = NB-2
      BUFF(NB) = RBIG
      BUFF(NB+1) = IBIG
      IF (NB.NE.1) GO TO 70
      CALL EXEC(2,ICMD,BUFF,ILEN,IOP1,IOP2)
      IF (ILEQ(2)) GO TO 80
      NB = 33
      IOP2 = IOP2-2
      IF (IOP2.LE.0) GO TO 20
      IOP1 = IOP1-1
      IOP2 = ISECT-2
      70 CONTINUE
      CALL EXEC(2,ICMD,BUFF,ILEN,IOP1,IOP2)
      80 NB0 = NB
      IOP10 = IOP1
      IOP20 = IOP2
C
      C      INITIALIZE QUANTITIES USED FOR EFFICIENT CALCULATION OF
      C      NUMERICAL COEFFICIENTS IN MIE SERIES
C
      FN = 100
      PN = 100
      NM = 1
C
      C      INITIALIZE RICHTI-BESSEL FUNCTION BETA FOR UPWARD RECURRENCE
      PSIN = 0.5IN(BETA)
      CHIN = 0.5CN(BETA)

```

```

PSINP1 = PSIN/BETA + CHIN
CHINP1 = CHIN/BETA + PSIN
RZETH = PSIN
IZETH = CHIN
PZTHP1 = PSINP1
IZTHP1 = CHINP1
C      INITIALIZE PREVIOUS COEFFICIENTS (A-SUB-N-1, B-SUB-N-1)
C      FOR USE IN ASYMMETRY FACTOR SERIES
ANM1 = (0.0,0.0)
BNM1 = (0.0,0.0)
QEXT = 0.
C      INITIALIZE ANGULAR FOR RIN AND SUMS FOR H+L AT ALL ANGLES
CALL DYNOMV(0.00,0.0,PSR,1,NN)
CALL DYNOMV(0.00,0.0,ISR,1,NN)
CALL DYNOMV(0.00,0.0,PSM,1,NN)
CALL DYNOMV(0.00,0.0,ISM,1,NN)
CALL DYNOMV(0.00,0.0,PSDS,1,NN)
CALL DYNOMV(0.00,0.0,ISDS,1,NN)
CALL DYNOMV(0.00,0.0,PSMS,1,NN)
CALL DYNOMV(0.00,0.0,ISMS,1,NN)
CALL DYNOMV(0.00,0.0,PSNM,1,NN)
CALL DYNOMV(0.00,0.0,ISNM,1,NN)
C
C
WRITE(LUOUT,2063+HELMONT,IL,NUMANG
2063 FORMAT(2N,4I6,E12.3)
C
C
DO 500 N = 1,NT
  PSIG = SURFMS
  ISIG = SURFMEL
  C      COMPUTE THE VARIOUS NUMERICAL COEFFICIENTS NEEDED
  FRI = PI*100
  IMON1 = EN*CHP1
  INP1 = ISM*FRI
  COPT = PI*100
  NO10H = 100*PI
  C
  C      CALCULATE THE MIE SERIES COEFFICIENTS LITTLE-H AND LITTLE-B
  C
  IF(NDIMAG) GO TO 300
  C      GENERAL CASE
  CALL DCDV(0.0,PSIG,ISIG,PI,TEM)
  TEM10 = TEM10 + PI*BETA
  TMX10 = TEM10*PZTHP1 + TEM20*IZTHP1 + RZETH
  TMX20 = TEM10*IZTHP1 + TEM20*PZTHP1 + IZETH
  HX10 = ((TEM10*(PSINP1+PSIN)*TMX10) + (TEM20*(PSINP1-PSIN)*TMX20))
  * (TMX10**2 + TMX20**2)
  HX20 = ((TEM20*(PSINP1+PSIN)*TMX10) + (TEM10*(PSINP1-PSIN)*TMX20))
  * (TMX10**2 + TMX20**2)
  TEM10 = PI1*PSIG + PI2*IRIGH + PI*BETA
  TEM20 = PI1*ISIG + PI2*IRIGH
  TMX10 = TEM10*IZTHP1 + TEM20*IZTHP1 + RZETH
  TMX20 = TEM10*PZTHP1 + TEM20*PZTHP1 + IZETH
  BX10 = ((TEM10*(PSINP1+PSIN)*TMX10) + (TEM20*(PSINP1-PSIN)*TMX20))
  * (TMX10**2 + TMX20**2)
  BX20 = ((TEM20*(PSINP1+PSIN)*TMX10) + (TEM10*(PSINP1-PSIN)*TMX20))
  * (TMX10**2 + TMX20**2)
  GO TO 300

```



```

300 CONTINUE
C      NO-ABSORPTION CASE
TEN(1) = (R1OP1/RB1GA+FN/BETA)*R2THP1-P2ETH
TEN(2) = (R1OP1/RB1GA+FN/BETA)*I2THP1-I2ETH
TNAC(1) = (R1OP1/RB1GA+FN/BETA)*PSINP1-PSIN
CALL DCDX(0,TMP(1),0,TEM,BN)
TEN(1) = (R1OP1/RB1GA+FN/BETA)*R2THP1-P2ETH
TEN(2) = (R1OP1/RB1GA+FN/BETA)*I2THP1-I2ETH
TNAC(1) = (R1OP1/RB1GA+FN/BETA)*PSINP1-PSIN
CALL DCDX(0,TMP(1),0,TEM,BN)
C
350 DEXT = DEXT+TMONP1+SNGL(ANK(1))+SNGL(BN(1))
IF(NOANGS) GOTO 450
C
C      PUT NIE SERIES COEFFICIENTS IN FORM NEEDED FOR COMPUTING S+, S-
C
RANP = COEFF*AN(1)+BN(1)
IANP = COEFF*AN(2)+BN(2)
RENK = COEFF*AN(1)-BN(1)
ISNP = COEFF*AN(2)-BN(2)
RANPM = NM*RANP
IANPM = NM*IANP
RENPM = NM*RENK
ISNPM = NM*ISNP
C
C      ADD UP SUMS WHILE UPWARD RECURSING ANGULAR FUNCTIONS LITTLE PI
C      AND LITTLE TAU
CALL DVMPI(XMU,1,FIN,1,VTEN,1,NM)
CALL DVSUB(VTEN,1,FIN(1),1,TMP,1,NM)
CALL DVMYCN(TMP,1,TAUN,1,NM)
CALL DVSUB(TAUN,1,FIN(1),1,TAUN,1,NM)
CALL DVMON(FIN,1,FIN(1),1,NM)
CALL DVMON(TMP,1,TMP,1,VTEN,1,FIN,1,NM)
C
CALL DVMON(FIN(1),1,TAUN,1,VTEN,1,NM)
CALL DVMON(AN(1),VTEN,1,REN(1),REN,1,NM)
CALL DVMON(IANP,VTEN,1,ISN(1),ISN,1,NM)
CALL DVMON(REN(1),VTEN,1,PSMS(1),PSMS,1,NM)
CALL DVMON(REN(1),VTEN,1,ISMS(1),ISMS,1,NM)
C
CALL DVSUB(FIN(1),1,TAUN,1,VTEN,1,NM)
CALL DVMON(REN(1),VTEN,1,REN(1),REN,1,NM)
CALL DVMON(REN(1),VTEN,1,ISN(1),ISN,1,NM)
CALL DVMON(REN(1),VTEN,1,PSPS(1),PSPS,1,NM)
CALL DVMON(REN(1),VTEN,1,ISPS(1),ISPS,1,NM)
C
C      UPDATE RELEVANT QUANTITIES FOR NEXT PASS THROUGH LOOP
450 NM = -NM
FN = FNPI
RN = REN(1)
AN(1) = (RN(1)+SNGL(AN(1))+SNGL(AN(2)))
BN(1) = (RN(1)+SNGL(BN(1))+SNGL(BN(2)))
C      CALCULATE RELEVANT BESSEL FUNCTIONS BY UPWARD RECURRENT
R2ET = (TMONP1/BETA+I2THP1-R2ETH)
I2ET = (TMONP1/BETA+I2THP1-I2ETH)
R2TH = R2THP1
I2TH = I2THP1
R2THP1 = R2ET
I2THP1 = I2ET
PSIN = PSINP1

```

```

      PSINP1 = RZTHP1
      NB = NB+2
      IF (NBLT.33) GO TO 500
      NB = 1
      IOP2 = IOP2+2
      IF (IOP2.LT.ISECT) GO TO 490
      IOP1 = IOP1+1
      IOP2 = 0
490 CALL EXEC(1,ICNMD,BUFF,ILEN,IOP1,IOP2)
500 CONTINUE
C
C
      QEXT = 2.*QEXT/BETA**2
      IF(NOANGS) RETURN
C
C      RECOVER S1 AND S2 FROM S+, S-
C
      DO 800 J = 1,NN
      S1(J) = 0.5*CMPLX(SNGL(RSP(J)+PSN(J)),SNGL(ISP(J)+ISM(J)))
      S2(J) = 0.5*CMPLX(SNGL(RSP(J)-PSN(J)),SNGL(ISP(J)-ISM(J)))
      S1(NNP1-J)=0.5*CMPLX(SNGL(RSP(J)+PSN(J)),SNGL(ISP(J)+ISM(J)))
800 S2(NNP1-J)=0.5*CMPLX(SNGL(RSP(J)-PSN(J)),SNGL(ISP(J)-ISM(J)))
C
      RETURN
      END
      SUBROUTINE DCDVCH,R1,R2,S,Q
C      PERFORMS COMPLEX MULTIPLICATION & DIVISION IN DOUBLE PREC
      DOUBLE PRECISION R1,R2,S(2),Q(2),DIV
      IF (R2.EQ.0. .AND. S(2).EQ.0.) GO TO 10
      DIV = S(1)**2+S(2)**2
      IF (N) 1,2
1 Q(1) = DSORT((R1**2+R2**2),DIV)
      RETURN
2 Q(1) = (R1*S(1)+R2*S(2))/DIV
  Q(2) = (R2*S(1)-R1*S(2))/DIV
      RETURN
10 Q(1) = R1/S(1)
  Q(2) = 0.
      RETURN
      END

```

T=00004 IS ON CR00028 USING 00013 BLKS P=0000

```

FTN4,L
C*****DOWIGHT, 28 JULY
PROGRAM CRIT
DIMENSION RBUF(3),IDCB(144),NAME(3)
REAL M,NS,IP,IS,NS,INTEN
DOUBLE PRECISION N,ST,THC
C DESIGNATE QUANTITIES TO BE STORED
EQUIVALENCE (RBUF(1),PD),RBUF(2),INTEN),(RBUF(3),TIP)
C * ,RBUF(4),S2P),RBUF(5),S2I)
DATA 15070,10PTH,0,1L,107
LUIN = LOGLOC(10000)
WRITE(LUIN,20000)
2000 FORMAT('ENTER R1,BETH,PTS,STRT, LAST ANGLE')
READ(LUIN,*) R1,BETH,PTS,STRT,STANG
WRITE(LUIN,2001)
2001 FORMAT('ENTER FILE NO CHS, CR, NO.2 CHS')
READ(LUIN,2002) NAME(1),NAME(2),NAME(3),ICR
2002 FORMAT(3H,12)
PI = 3.14159265358979
P4 = PI/4.
S2 = SQRT(2.)
N = 1.D0/PI
THC = DATA(1,00,DSORT(N**2-1,00))
TH2 = THC-0.9E-2
TH3 = THC-0.9E-2
TH4 = THC-1.9E-3
PHC = PI-2.*THC
NS = N/N
A = BETH*(2.00/PI)
HK = SORT(A*POS(SHGL(THC)))
TH = STRT+THC
E = -THC-TH/PTS
E2 = E**2.
E3 = E**3.
E4 = E**4.
BSQ = BETH**2/4.
C OPEN DATA FILE DESIGNATED BY NAME
CALL OPEN(IDCB,IEPR,NAME,10PTH,150,1CR)
IF(IEPR.LT.0) GO TO 999
RBUF(1) = BETH
RBUF(2) = 1./N
RBUF(3) = 0.
C STORE FUNCTIONS DESIGNATED IN RBUF EQUIVALENCE STATEMENT
CALL WRITE(IDCB,IEPR,RBUF,1L)
10 ST = DSIN(DEL(TH))
R = DATA(HST,DSORT(1.00-(N*ST)**2))
D = R-TH
PH = 2.*D
CT = COS(TH)
PD = PH IN DEGREE
PD = PD*57.2958
D = NS*1.000000E7
C COMPUTE VAN DE HULST DIVERGENCE FACTOR
G1 = CT*ST*(1.00-1./NSIN(PH))
S = PATH
EP = CT*PD*(DATA(C)**2)
PS = -NSIN(PSIN(S)**2)
C COMPUTE INTENSITIES OF THE TRANSMITTED + REFLECTED RAY

```

```

IP = G1*4.+(1.-FP)**2
IC = G1*4.+(1.-FS)**2
ETA = PHC-PH
W = SIN(ETA)*AK
THB = THC+ETA/2
DEL1 = ATAN(SORT(SIN(THB)**2-1./NS)/COS(THB))
DEL2 = 2.*ATAN(NS+TAN(DEL1))
DEL1 = 2.*DEL1
ETAC = 2.*ETA*(COS(THB)-CT+COS(R)/N)
B1=ETAC+P4+DEL1
B2=ETAC+P4+DEL2
S11=SORT(IC)
S12=SORT(1D)
CB1=COS(B1)
CB2=COS(B2)
SB1=SIN(B1)
SB2=SIN(B2)
GOTO 40
C      THIS CODE USED WHEN PH>PHC
30 ETAD = ETAD-DETH
ETA = ETAD/57.2958
PH = PHC-ETA
PD = PH*57.2958
W = SIN(ETA)*AK
S11=0.
S12=0.
CB1=1.
CB2=1.
SB1=0.
SB2=0.
40 CALL FRES(W,FS,FC)
FS=FS/S02
FC=FC/S02
S1R=FC*CB1+FS*SB1+S11
S2R=FC*CB2+FS*SB2+S12
S1I=FS*CB1-FC*SB1
S2I=FS*CB2-FC*SB2
C      COMPUTE PHASE DIFFERENCE
PH1=57.2958*ATAN(S1I/S1R)
PH2=57.2958*ATAN(S2I/S2R)
IF(S1R.LT.0.) PH1=180.+PH1
IF(PH1.GT.180.) PH1=PH1-360.
IF(S2R.LT.0.) PH2=180.+PH2
IF(PH2.GT.180.) PH2=PH2-360.
DIFR=PH2-PH1
IF(DIFR.GT.180.) DIFR=DIFR-360.
IF(DIFR.LT.-180.) DIFR=DIFR+360.
C      COMPUTE TOTAL INTENSITIES
TIS=(S1R**2+S1I**2)
TIP=(S2R**2+S2I**2)
INTEN=ALOG10(5*(TIS+TIP))
IF(ANODE.PD,1E-4).EQ.0.) WRITE(LUIN,1000) PD,TIS,TIP,DIFR
1000 FORMAT(F8.4,2E14.6,F10.4)
CALL WRITE(IDCB,IERR,PBUF,IL)
IF(TH.LT.TH0) GOTO 30
IF(PD.LT.STARG) GOTO 30
GOTO 999
50 IF(TH.GE.TH3) E=E2
IF(TH.GE.TH3) E=E3
IF(TH.GE.TH4) E=E4

```

```

      TH=TH+E
      IF(TH.LT.TH0) GOTO 10
      ETAD=0.
      DETA=.05
      GOTO 30
    999 CALL CLOSE(IOC8)
      WRITE(LUIN,2003) IERR
    2003 FORMAT("IERR=",14)
      STOP
      END
      SUBROUTINE FRES(W,F,FC)
C      THIS SUBR CALCULATES THE FRESNEL INTEGRAL FROM 0 TO W
      W = ABS(W)
      F = (1.+1.926*W)/(2.+1.792*W+3.104*W**2)
      G = 1./(2.+4.142*W+3.492*W**2+6.670*W**3)
      A = 1.570796*W**2
      C = COS(A)
      S = SIN(A)
      FC = .5+F*S-G*C
      FS = .5-F*C-G*S
      IF(W.LT.0.) GOTO 3
      FC = FC+.5
      FS = FS+.5
      RETURN
3    FC = .5-FC
      FS = .5-FS
      RETURN
      END

```

Paper No. 7

Glory in the optical backscattering from air bubbles (D. S. Langley
and P. L. Marston) Accepted for Publication in Physical Review
Letters

Abstract

Observations of light backscattered from air bubbles in a viscous liquid demonstrate an enhancement due to axial focusing. A physical-optics approximation for the cross-polarized scattering correctly describes the spacing of regular features observed. The non-cross-polarized scattering is not adequately described by a single class of rays.

The Mie solution¹ for electromagnetic scattering by a sphere frequently does not lead to direct interpretation of the angular scattering pattern. Consequently, models have been developed to facilitate an understanding of the structure in the scattered intensity present where intensity is plotted as a function of the scattering angle ϕ or the size parameter $x = ka$ (k = wave-number; a = sphere radius). These models have emphasized the angular regions where diffraction is important for a drop of water in air: the rainbow,^{2,3} $\phi \approx 180^\circ$,³⁻⁵ and $\phi \approx 0^\circ$.^{3,6} In the scattering of light by a spherical air bubble in a liquid or in glass, the real part of the refractive index of the sphere is less than that of the surroundings and the models must be significantly modified. New phenomena appear, such as diffraction^{7,8} in the region of the critical scattering angle ϕ_c . Here we report the first detailed observations of backscattering by air bubbles in liquids and give a model which describes some of the observed features. We refer to this as glory because, as in the case of drops,³⁻⁵ the $\phi \approx 180^\circ$ scattering is enhanced when x is large.

Van de Hulst^{3,4} gave a partial explanation of the enhancement for drops by noting the axial focussing of those backscattered rays which have a non-zero impact parameter. When modeling this focussing in the far field, diffraction provides an essential correction to ray optics because the factor in the scattered intensity which accounts for geometrical divergence of the rays goes to ∞ as $\phi \rightarrow 180^\circ$. Examination of this factor in ray-optics models of scattering by bubbles⁹ shows that this ∞ is not restricted to drops. We have modeled the backscattering with a physical-optics approximation. The procedure is to (a) compute amplitudes in an exit plane in contact with the bubble via ray optics, and (b) allow this wave to diffract to the far field where the distance from the bubble's center $R \gg ka^2$.

Fig. 1 illustrates several rays which lead to backscattering. The paths are determined by the number of chords p and $m = m_i/m_o$ where the refractive indices of the inner and outer media, m_i and m_o , are taken to be real. Fig. 1 is drawn with $m^{-1} = 1.403$ which corresponds to an air bubble in the dimethylsiloxane-polymer liquid used in the experiment. All rays satisfy $\sin\theta = m\sin\phi$. For $\phi = 180^\circ$, the off-axis (or glory) rays have $\alpha = 0$ and $\rho = \tilde{\rho}$ where: $^{10} \tilde{\rho} = p\tilde{\rho} + (2g+2-p)90^\circ$, g is a non-negative integer ($g = 0$ for rays in Fig. 1) and $m < 1$ requires that $p \geq 3$. The exit plane (dashed line in Fig. 1) touches C' with its normal parallel to the propagation direction of the incident wave.

Our description of the field in the exit plane is facilitated by considering the propagation of a wavelet de which lies close to the backscattered path. Fig. 1 shows de for $p = 3$; it emerges as curve $d'e'$. This curve appears to come from a ring-like source at F known as the focal circle in the analogous $p = 2$ scattering from drops⁴ with $\sqrt{2} < m < 2$. The source is ring-like because the figure may be rotated around the CC' axis. The radius of the ring is $b = a\sin\tilde{\theta}$. After the incident ray crosses the dashed vertical plane (the entrance plane), the propagation phase delay for reaching the exit plane is $\eta = ka[1 - \cos\theta + (1 - \cos\beta)\sec(\theta-\beta) + 2m\pi\cos p]$. The ray crosses the exit plane at a radius s from C' with $s/a = \sin\beta - (1 - \cos\beta)\tan(\theta-\beta)$. The radius α of arc $d'e'$ follows from the curvature at $s = b$: $\alpha = k(d^2\eta/ds^2)^{-1} = a[1 + \frac{1}{2}(p-1)^{-1}\cos\theta]$ where $\tau = \tan\tilde{\rho}/\tan\theta$. The spreading of the wavelet is characterized by $q = \lim_{\tilde{\theta} \rightarrow 0} \overline{d'e'}/\overline{de}$ as $\tilde{\theta} \rightarrow 0$ where the bar denotes the arc length. An equivalent expression for q is $[\lim_{\tilde{\theta} \rightarrow 0} [b - s(\theta)]/(b - a\sin\tilde{\theta})]$ as $\tilde{\theta} \rightarrow \tilde{\theta}$; its value from L'Hospital's rule is $\alpha/(\alpha - a)$. Vectors \hat{e}_ℓ ($\ell = 1, 2$) denote orthogonal basis vectors in both the entrance and exit planes; \hat{e}_1 is chosen parallel to the polarization of the incident wave's electric field $E_i \exp(-i\omega t)$.

In the exit plane, the field $E_p^{\hat{e}_\ell}$ of the outgoing p th glory wave is computed by applying Van de Hulst's method of first decomposing the fields

perpendicular and parallel to the scattering plane.^{3,4} Exit-plane polar coordinates centered on C' are (s, ψ) where ψ is the angle relative to \hat{e}_1 and \hat{s} and $\hat{\psi}$ denote local basis vectors. We assume $x \gg 1$ and use Fresnel's coefficients r_j for the internal reflections where $j = 1, 2$ for fields parallel to $\hat{\psi}$ and \hat{s} , respectively. If $|s-b| \ll a$, the multiple internal reflections give:

$$E_p^\ell = E_I q^{-1/2} F^\ell \exp[i\tilde{\eta} + ik(s-b)^2/2\alpha] \quad (1)$$

where $\tilde{\eta} = \mu + \eta(\rho = \tilde{\rho})$, $F^1(\psi) = c_1 \sin^2 \psi + c_2 \cos^2 \psi$, $F^2(\psi) = \frac{1}{2}(c_2 - c_1) \sin 2\psi$, and $c_j = (-1)^{p(j-1)} r_j^{p-1} (1 - r_j^2)$. The new phase term μ accounts for the crossing of caustics or "focal lines"; its value is^{3,11} $-\pi(p+g)/2$. The r_j are evaluated at $\tilde{\theta}$: $r_1 = \sin(\tilde{\theta} - \tilde{\rho})/\sin(\tilde{\theta} + \tilde{\rho})$, $r_2 = \tan(\tilde{\theta} - \tilde{\rho})/\tan(\tilde{\theta} + \tilde{\rho})$. The sign factor in c_j accounts for a geometrical inversion (present when $j = 2$ and p is odd) which is not evident in descriptions of $p = 2$ glory in drops.^{3,4}

The field E_p^ℓ at a distant point Q is computed as follows. The left extension of the CC' axis makes an angle γ with $C'Q$. When γ is small and $\overline{C'Q} = R' \gg ka^2$, scalar diffraction theory and the Fraunhofer approximation¹² give:

$$E_p^\ell \approx \frac{kE_I e^{i(kR' + \tilde{\eta})}}{2\pi i R' q^{1/2}} \int_0^\infty s W^\ell e^{ik(s-b)^2/2\alpha} ds \quad (2)$$

$$W^\ell = \int_0^{2\pi} F^\ell e^{-iks \sin \gamma \cos(\psi - \xi)} d\psi \quad (3)$$

where ξ is the angle between \hat{e}_1 and the projection of $\overline{C'Q}$ on the exit plane. In Eq. (2), the approximation given by Eq. (1) has been extended beyond its useful domain in anticipation of the stationary phase approximation (SPA) of the integral. Direct evaluation of Eq. (3) gives $\tilde{W}^1(\gamma, \xi) = W^1(\gamma, \xi, s = b)$

$= \pi[(c_1 + c_2)J_0(u) + (c_1 - c_2)J_2(u) \cos 2\xi]$ and $\tilde{W}^2 = \pi(c_1 - c_2)J_2(u) \sin 2\xi$ where $u = kbs\sin\gamma$. The SPA of Eq. (2) gives the pth glory contribution to the scattered field when kb^2/α , and thus x , are large. In the experiments to be described $x \geq 4000$ and the SPA is applicable.

The total field may be approximated by summing the E_p^ℓ from Eq. (2) with the fields due to axial reflections and surface waves. Surface wave contributions should be small for the observed bubbles due to the largeness of x . To determine which glory and axial terms are important to the total field, and for other heuristic reasons, consider the ℓ -polarized intensity I_p^ℓ of the pth field taken alone. The SPA of Eq. (2) gives:

$$I_p^\ell = (2/\pi) x I_R f_{p,g} |W^\ell(r, \theta)|^2 \quad (4)$$

where $I_R = I_I \alpha^2 / 4R^2$ is the total intensity at a distance $R = \overline{CQ}$ from a perfectly reflecting sphere of radius α predicted by ray optics,⁹ I_I is the incident intensity, and $f_{p,g} = b^2 \alpha / \alpha^3 q = b^2 (\alpha - \alpha) / \alpha^3$. In Eq. (4), R has replaced R' from (2) and γ becomes $180^\circ - \phi$ because $R \gg \alpha$. Geometrical optics^{3,9} gives the intensities \tilde{I}_p^ℓ of separate axial reflections (e.g. $p = 0$ and 2 in Fig. 1) which are proportional to α^2 . The strongest reflection has $p = 0$ and $\ell = 1$; for $\gamma = 0$, $\tilde{I}_0^1 = I_R (m-1)^2 / (m+1)^2$ while $\tilde{I}_0^2 = 0$. Since $f_{p,g}$ does not depend on α , $I_p^\ell \propto kd^3$ and glory terms dominate the backscattering when α is large.

Consider a bubble with $x = 4000$ and $m = 1.403^{-1}$. The strongest glory terms have $g = 0$ and $p = 3, 4$, and 5; the I_p^1 / I_R for $\gamma = 0$ are respectively 1.03, 0.43, and 0.16. The I_p^1 decrease with increasing p due to the partial reflections in the bubble. The strongest axial ray gives $\tilde{I}_0^1 / I_R = 0.028$. The interference of the fields depends on α and our Mie computations verify that the backscattered intensity is not simply proportional to α^3 even for this

large value of x . The $\ell = 2$ (cross-polarized) scattering is, however, nearly dominated by the $p = 3$ glory term. Due to symmetry, $\ell = 2$ scattering vanishes as $\gamma \rightarrow 0$. The $I_p^2(\gamma \neq 0, \xi)$ have maxima at $\xi = \pm 45^\circ$ and $\pm 135^\circ$ and they vanish at $\xi = 0^\circ, \pm 90^\circ$, and 180° . Let $\gamma = \gamma_p$ locate the first maxima of $I_p^2(\gamma, \xi = 45^\circ)$. The largest $\ell = 2$ terms have $I_p^2(\gamma_p, \xi = 45^\circ)/I_R = 0.53$ and 0.10 for $p = 3$ and 4 . To the extent that $p \neq 3$ scattering may be neglected, the $\ell = 2$ intensity will be quasi-periodic in γ .

We have numerically verified the validity of Eq. (4) by using Debye's localization principle^{3,4} to modify Mie theory so that only partial waves associated with $p = 3$ rays were included in the Mie series. Furthermore, when Eq. (4) is applied to spheres with certain $m > 1$, the resulting $I_p^1(\gamma = 0)$ agree with the glory "analog" tabulated in Ref. 11. This analog was derived by applying the Watson transformation to the $\gamma = 0$ Mie series.

Fig. 2 diagrams the experiment. A syringe injected bubbles into the liquid. The liquid had a high kinematic viscosity ($\approx 600\,000$ cS) and a single bubble could be observed for hours. The laser's power output was 5 mW and the beam diam was 5 mm. The wavelength in the liquid $2\pi/k$ was $632.8\text{ nm}/1.403$; \hat{e}_1 lay in the splitter's plane of incidence. The camera was focused on ∞ so the photographs recorded the far-field intensity pattern.^{7,12} Photographs were made with $a \approx 0.3\text{--}0.8$ mm corresponding to $x \approx 4000\text{--}11000$. Exposure times were typically 5s for TriX film and a 200 mm focal length camera lens.

Fig. 3 demonstrates that the scattering has roughly the dependence on ξ predicted by Eq. (4); $\xi = 0^\circ$ corresponds to scattering toward the top of the photographs and $\gamma = 0^\circ$ corresponds to the center of the symmetry. Fig. 3(b) shows that the $\ell = 1$ scattering for $\gamma > 0.2^\circ$ is significantly stronger for $\xi = \pm 90^\circ$ than it is for $\xi = 0^\circ$. This agrees with the following model results: (1) $(c_1/c_2)^2 \gg 1$ (for $p = 3$ we predict $c_1/c_2 \approx -5.2$); and (ii) for this x ,

the I_p^1 depend only weakly on ξ and are dominated by the I_p^1 . One prediction of Eq. (4) could be quantitatively checked: when both $\sin \gamma \approx \gamma$ and $u \gg 1$, the minima in I_p^2 should be spaced by $\Delta \gamma$ rad such that $kb\Delta \gamma \approx \pi$ where for $p = 3$, $b/a = 0.447$. Fig. 4 compares this with the mean spacing of ≈ 40 dark rings lying outside the 9th ring from the center. The error bars combine uncertainties in measured a and $\Delta \gamma$ with those of corrections due to refraction at the cell-air interface⁷ and the tilt of the cell. Fig. 4 shows that $p = 3$ rays dominate the $\ell = 2$ scattering. The modulations of the intensity along $\xi = \pm 45^\circ$ in Fig. 3(b) show that other rays contribute to $\ell = 1$ scattering since the predicted $I_3^1 \propto [J_0(u)]^2$.

In conclusion, backscattering from bubbles can be enhanced by axial focusing. The number of significant glory terms depends on m . The main contributions differ from those for water drops where surface waves³ and other diffraction related terms⁵ play an essential role. If focusing were not present, scattering by large bubbles would be $\ll 1_R$ in the region⁷⁻⁹ $(\phi_c + 10^\circ) \lesssim \phi \lesssim 180^\circ$ where $\phi_c = 2 \cos^{-1} m \approx 89^\circ$ for $m^{-1} = 1.403$. We also find evidence of $p = 3$ glory in Mie computations for bubbles in water.

This work was supported by the Office of Naval Research. P. L. Marston is an Alfred P. Sloan Research Fellow.

References

1. G. Mie, Ann. Phys. (Leipzig) 25, 377 (1908).
2. V. Khare and H. M. Nussenzveig, Phys. Rev. Lett. 33, 976 (1974).
3. H. C. Van de Hulst, Light Scattering by Small Particles (Wiley, New York, 1957).
4. H. C. Van de Hulst, J. Opt. Soc. Am. 37, 16 (1947).
5. V. Khare and H. M. Nussenzveig, Phys. Rev. Lett. 38, 1279 (1977).
6. H. M. Nussenzveig and W. J. Wiscombe, Opt. Lett. 5, 455 (1980).
7. P. L. Marston, J. Opt. Soc. Am. 69, 1205 (1979).
8. D. L. Kingsbury and P. L. Marston, J. Opt. Soc. Am. 71, 358 (1981).
9. G. E. Davis, J. Opt. Soc. Am. 45, 572 (1955).
10. M. Kerker, The Scattering of Light and Other Electromagnetic Radiation (Academic, New York, 1969).
11. J. J. Stephens, P. S. Ray, and T. W. Kitterman, Appl. Opt. 14, 2169 (1975).
12. J. W. Goodman, Introduction to Fourier Optics (McGraw Hill, New York, 1968).

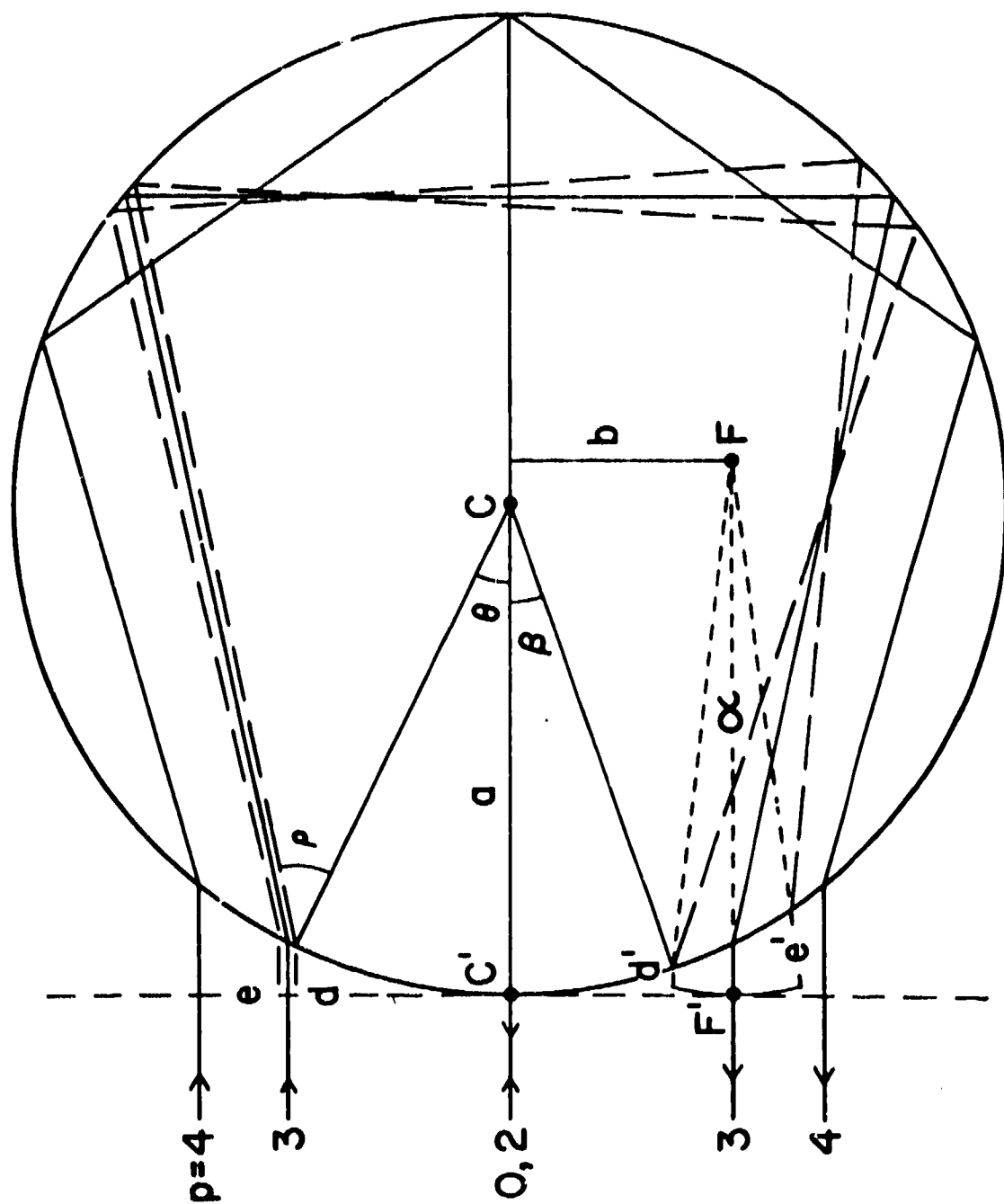
Fig. Captions

Fig. 1. Rays which contribute to backscattering. The local angle of incidence is θ and C is the bubble's center.

Fig. 2. Apparatus for observing backscattering from bubbles.

Fig. 3. Photographs for: (a) crossed polarizer ($\ell = 2$ scattering); (b) uncrossed polarizer ($\ell = 1$); and (c) no polarizer. The incident polarization was vertical. $a = 0.49$ mm and $x = 6830$.

Fig. 4. Measurement and model for the angular separation of the dark rings in the $\ell = 2$ scattering.



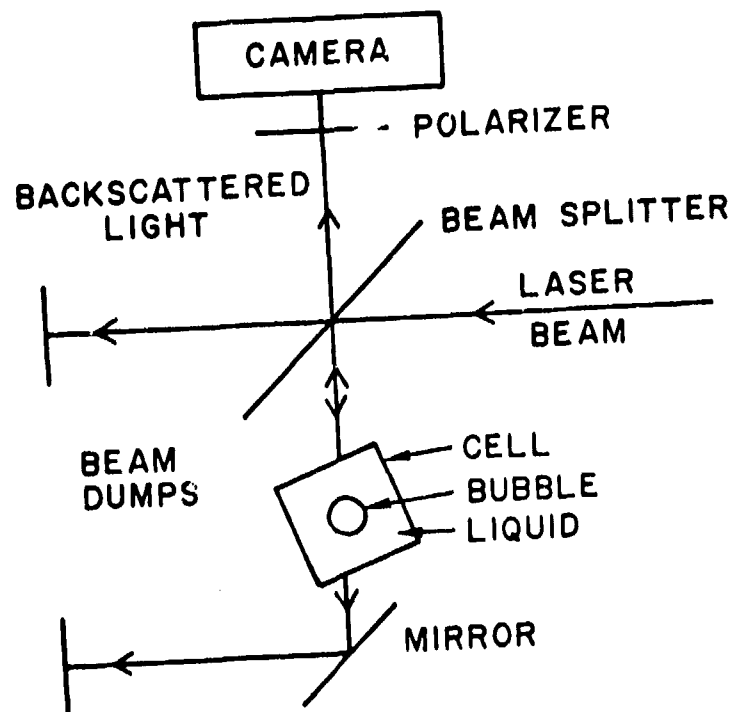
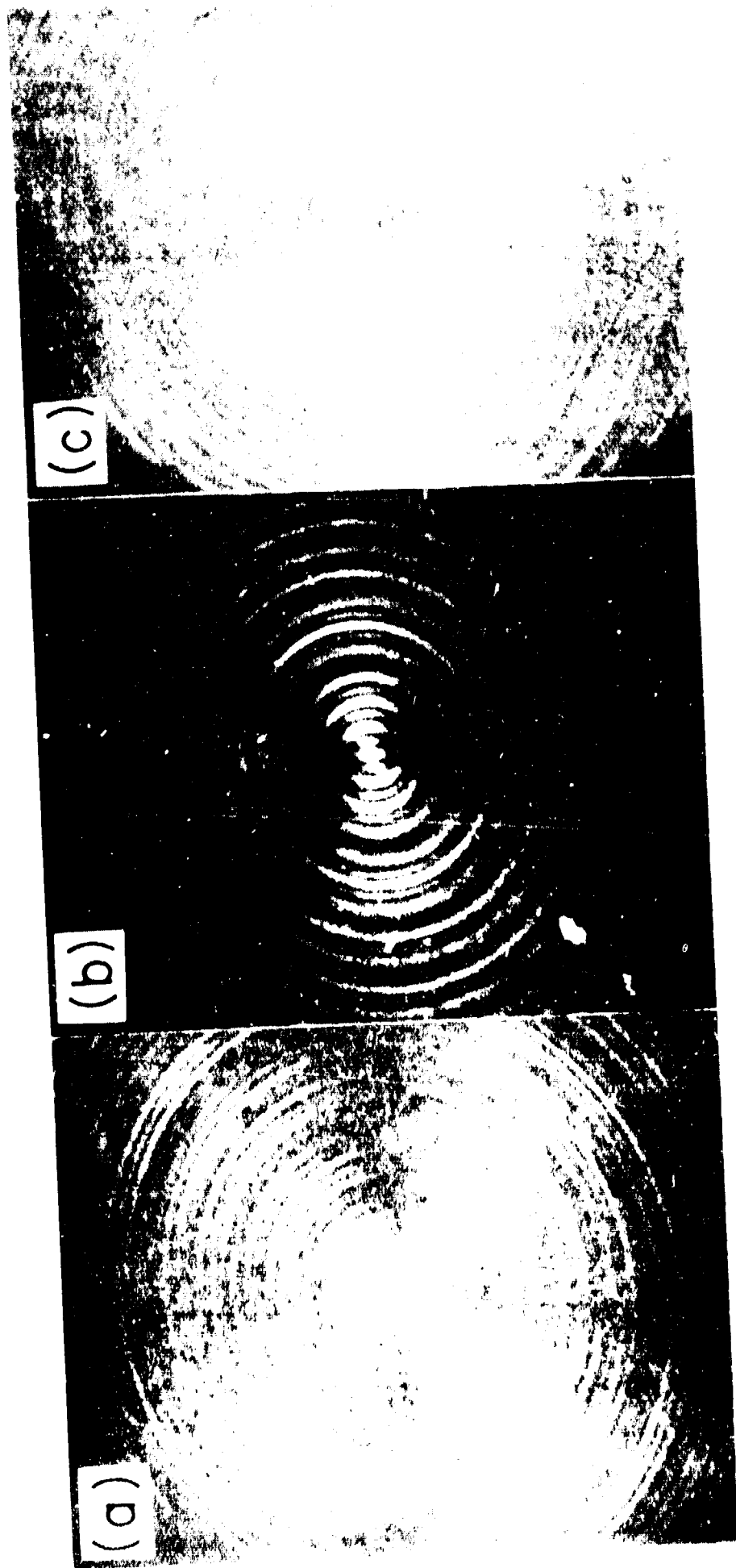


Fig. 2



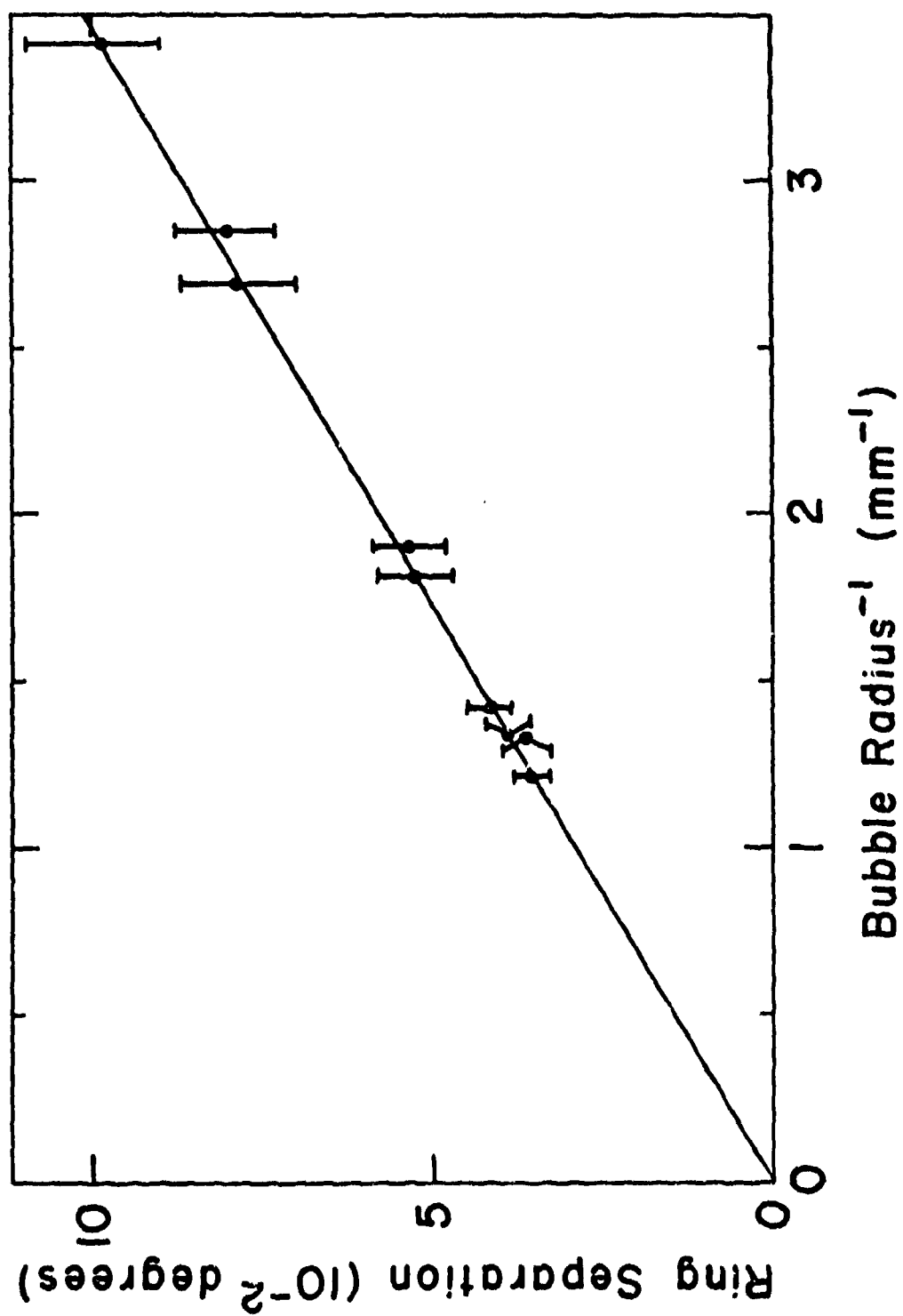


Fig. 4

February 1981

REPORTS DISTRIBUTION LIST FOR ONR PHYSICS PROGRAM OFFICE
UNCLASSIFIED CONTRACTS

Director Defense Advanced Research Projects Agency Attn: Technical Library 1400 Wilson Blvd. Arlington, Virginia 22204	3 copies	Director U. S. Army Engineering Research and Development Laboratories Attn: Technical Documents Center Fort Belvoir, Virginia 22060	1 copy
Office of Naval Research Physics Program Office (Code 421) 800 North Quincy Street Arlington, Virginia 22217	3 copies	ODDRE Advisory Group on Electron Devices 201 Varick Street New York, New York 10014	3 copies
Office of Naval Research Director, Technology (Code 200) 800 North Quincy Street Arlington, Virginia 22217	1 copy	Air Force Office of Scientific Research Department of the Air Force Bolling AFB, D. C. 22204	1 copy
Naval Research Laboratory Department of the Navy Attn: Technical Library Washington, DC 20375	3 copies	Air Force Weapons Laboratory Technical Library Kirtland Air Force Base Albuquerque, New Mexico 87117	1 copy
Office of the Director of Defense Research and Engineering Information Office Library Branch The Pentagon Washington, DC 20301	3 copies	Air Force Avionics Laboratory Air Force Systems Command Technical Library Wright-Patterson Air Force Base Dayton, Ohio 45433	1 copy
U. S. Army Research Office Box 12211 Research Triangle Park North Carolina 27709	2 copies	Lawrence Livermore Laboratory Attn: Dr. W. F. Krupke University of California P.O. Box 808 Livermore, California 94550	1 copy
Defense Technical Information Center Cameron Station Alexandria, Virginia 22314	12 copies	Harry Diamond Laboratories Technical Library 2800 Powder Mill Road Adelphi, Maryland 20793	1 copy
Director, National Bureau of Standards Attn: Technical Library Washington, DC 20234	1 copy	Naval Air Development Center Attn: Technical Library Johnsville Warminster, Pennsylvania 18974	1 copy
Commanding Officer Office of Naval Research Western Regional Office 1031 East Green Street Pasadena, California 91101	3 copies	Naval Weapons Center Technical Library (Code 753) China Lake, California 93555	1 copy
Commanding Officer Office of Naval Research Eastern/Central Regional Office 666 Summer Street Boston, Massachusetts 02210	3 copies	Naval Training Equipment Center Technical Library Orlando, Florida 32813	1 copy
		Naval Underwater Systems Center Technical Center New London, Connecticut 06320	1 copy

Commandant of the Marine Corps Scientific Advisor (Code 40-1) Washington, DC 20380	1 copy	Dr. L. Flax, Code 791 Naval Coastal Systems Center Panama City, FL 31407	Dr. Taylor Wang Jet Propulsion Lab. 4800 Oak Grove Pasadena, CA 91103
Naval Ordnance Station Technical Library Indian Head, Maryland 20640	1 copy	Don Rottler Code 701 Naval Undersea Warfare Eng. Station Keyport, WA 98345	Q. Duntley or C. S. Cox Visibility Laboratory Scripps Inst. Oceanography University of California San Diego La Jolla, CA 92152
Naval Postgraduate School Technical Library (Code 0212) Monterey, California 93040	1 copy	Dr. H. Medwin Physics Department US Naval Postgraduate School Monterey, CA 93940	B. D. Johnson or R. C. Cook Department of Oceanography Dalhousie University Halifax, Nova Scotia CANADA B3H 4J1
Naval Missile Center Technical Library (Code 5632.2) Point Mugu, California 93010	1 copy	Dr. Robert E. Apfel Mason Laboratory Yale University P.O. Box 2159 New Haven, CT 06520	Dr. Akira Ishimaru Dept. of Electrical Engineering University of Washington Seattle, WA 98195
Naval Ordnance Station Technical Library Louisville, Kentucky 40214	1 copy	Dr. D. T. Blackstock Applied Research Laboratory University of Texas Austin, TX 78712	G. C. Mooradian or R. J. Giannaris Naval Ocean System Center San Diego, CA 92152
Commanding Officer Naval Ocean Research & Development Activity Technical Library NSR Station, Mississippi 39204	1 copy	Dr. Bill D. Cook Dept. of Mechanical Engineering University of Houston Houston, TX 77004	Dr. H. Uberall Physics Department Catholic University Washington, D.C. 20064
Naval Explosive Ordnance Disposal Facility Technical Library Indian Head, Maryland 20640	1 copy	Dr. Lawrence A. Crum Department of Physics University of Mississippi University, MS 38677	Dr. John E. Tyler Scripps Inst. Oceanography 2212 Sverdrup Hall, A-024 La Jolla, CA 92093
Naval Ocean Systems Center Technical Library San Diego, California 92152	1 copy	Dr. W. M. Fairbank Physics Dept. Stanford University Stanford, CA 94305	Dr. N. Lagakos, Code 5134 Naval Research Laboratory Washington, D.C. 20375
Naval Surface Weapons Center Technical Library Silver Spring, Maryland 20910	1 copy	Dr. R. A. Graham Shock Wave Division Sandia Laboratories Albuquerque, NM 87185	Dr. G. C. Gaunard Naval Surface Weapons Center R-31, White Oak Silver Spring, MD 20910
Naval Ship Research and Development Center Central Library (Code 142 and 143) Bethesda, Maryland 20884	1 copy	Dr. Joseph B. Keller Department of Mathematics Stanford University Stanford, CA 94305	Dwight L. Kingsbury, MS 02-15 Boeing Commercial Airplane Co. P.O. Box 3707 Seattle, WA 98124
Naval Avionics Facility Technical Library Indianapolis, Indiana 46218	1 copy	Dr. I. Rudnick Physics Department University of California Los Angeles, CA 90024	Dr. Warren J. Wiscombe Dept. of Applied Science New York University New York, NY 10003
Dr. Milton Kerker Chemistry Dept. Clarkson College Potsdam, N.Y. 13676			
Dr. Milton S. Plesset Dept. of Engineering Science California Institute of Tech. Pasadena, CA 91125			